ATOMISTIC SCALE INVESTIGATION OF THERMAL STABILITY, CLUSTER
DYNAMICS AND MICROSTRUCTURAL EVOLUTION OF IMMISCIBLE CU-TA ALLOYS

by

Raj Kiran Koju
A Dissertation
Submitted to the
Graduate Faculty
of
George Mason University
in Partial fulfillment of
The Requirements for the Degree
of
Doctor of Philosophy
Physics

Committee:

_____   Dr. Yuri Mishin, Dissertation Director

_____   Dr. Howard Sheng, Committee Member

_____   Dr. Patrick Vora, Committee Member

_____   Dr. Maria Emelianenko, Committee Member

_____   Dr. Paul So, Department Chairperson

_____   Dr. Donna Fox, Associate Dean, Office of
                                     Student Affairs & Special Programs,
                                     College of Science

_____   Dr. Ali Andalibi, Dean,
                                     College of Science

Date: _____   Fall Semester 2019
                                     George Mason University
                                     Fairfax, VA

Atomistic Scale Investigation of Thermal Stability, Cluster Dynamics and Microstructural Evolution of Immiscible Cu-Ta Alloys

A dissertation submitted in partial fulfillment of the requirements for the degree of Doctor of Philosophy at George Mason University

By

Raj Kiran Koju
Master of Science
Tribhuvan University, 2011
Bachelor of Science
Tribhuvan University, 2008

Director: Dr. Yuri Mishin, Professor
Department of Physics and Astronomy

Fall Semester 2019
George Mason University
Fairfax, VA

Dedication

I would like to dedicate this dissertation to my grandparents, Govinda Das Koju and Ganesh Maya Koju, and my parents, Ganesh Lal Koju and Chandra Maya Koju, for their tremendous effort and support for my higher education. Last but not least, to my loving wife, Pramila Awal, and son, Salween Koju, for all sacrifices they had to go through.

Acknowledgments

I would like to extend my deepest gratitude to my advisor Dr. Yuri Mishin for providing me an opportunity to carry out this dissertation under his supervision. His invaluable support, motivation, and guidance have always initiated me to surpass all limits and move forward with an inner strength. I will be ever indebted to him for teaching me how to deal with the research problems and accomplish any goal.

I am equally grateful to Dr. Ganga Prasad Purja Pun for his stimulating and constructive suggestions during this work. I learned a lot from him for developing the computational algorithm to solve complex research problems.

I gratefully acknowledge my dissertation committee members Dr. Howard Sheng, Dr. Patrick Vora, and Dr. Maria Emelianenko for reviewing my dissertation and providing their feedback. Also, I would like to express my sincere thanks to Dr. Robert Weigel, Dr. Joseph C. Weingartner, and all professors and staff of the department of physics and astronomy for making my PhD journey joyful.

I want to thank my sisters, Gauri and Gayatri, for their support and encouragement throughout my life. Their passion and affection are the greatest sources of inspiration in every step of my life.

Finally, I want to acknowledge my wife, Pramila Awal, for being a constant source of inspiration. I could not have done it without her help. All this work reflects her encouragement and helping me so much in caring for our son, Salween.

Table of Contents

List of Tables

List of Figures

xiii

Abstract

ATOMISTIC SCALE INVESTIGATION OF THERMAL STABILITY, CLUSTER DYNAMICS AND MICROSTRUCTURAL EVOLUTION OF IMMISCIBLE CU-TA ALLOYS

Raj Kiran Koju, PhD

George Mason University, 2019

Dissertation Director: Dr. Yuri Mishin

Nanocrystalline immiscible Cu-Ta alloys produced by mechanical alloying emerged as a new class of material for high temperature and high strength applications. The extraordinary structural stability of this alloy is believed to be due to the effect of precipitated Ta nanoclusters on thermodynamics and mobility of internal interfaces, primarily grain boundaries (GBs). In order to better understand this effect, we studied the interaction of Ta clusters with individual GBs driven by applied shear stress and capillary force. The atomistic simulations provided strong evidence that the experimentally found extraordinary grain size stabilization in Cu-Ta alloys is dominated by the kinetic factor associated with the Zener pinning of GBs by Ta clusters. Also, the effect of solute drag at GBs in a random solution is not as strong as cluster pinning. A moving GB in the random solution displays a stop-and-go character of motion precipitating a set of Ta clusters due to short circuit Ta diffusion in the GB core.

Moreover, atomistic simulations confirmed that small Ta clusters have FCC structure and remain at least partially coherent with the Cu matrix. As the cluster size increases, it becomes incoherent and emits misfit dislocations into the matrix. At higher temperatures, the lattice misfit between the Ta clusters and the matrix decreases, promoting better

coherency. The core-shell Ta clusters observed in experiments can be explained with the redistribution and the crystallization of Cu and Ta atoms in a Ta rich amorphous solution.

Simulated deformation and creep tests conducted under tension and compression have shown that the Ta clusters effectively suppress the grain boundary mechanisms of plastic deformation, such as sliding and grain rotation. The Ta clusters also inhibit deformation-induced grain growth and suppress the operation of dislocation sources inside the grains leading to high strength and structural stability. The strain rate sensitivity parameter of Cu-Ta alloy exhibits a limited rate of strain hardening even when subjected to temperatures as high as 80% of melting point (1327 K) where pure nanocrystalline Cu becomes unstable and undergoes rapid grain growth. We observed that creep in Cu-Ta alloy is governed by atomic diffusion with the stress exponent 3.78±0.44, while this value predicts dislocation based creep mechanism in pure nanomaterials.

Chapter 1: Introduction

Nanocrystalline pure metals are famous for their superior physical properties compared to coarse-grained materials. Experiments and computer simulations have extensively demonstrated and well established improved mechanical strength, electrical and magnetic properties, corrosion, and wear resistance in nanocrystalline materials [1–11]. However, their applications at higher temperatures are fundamentally limited because of their lack of structural stability and coarsening process even at lower temperatures. This has been attributed to the generation of a large density of grain boundaries (GBs) with a continual reduction in grain size, which enhances excess free energy responsible for driving GB migration. In practice, grain stabilization is achieved through the addition of impurities on pure metals. The added impurities bring grain stabilization either by reducing the GB free energy through solute segregation across the GBs [12–16] or by reducing the GB mobility through solute drag [17–21] or Zener pinning mechanism [22–24] due to precipitated solute second phase. While the approach involving the reduction of GB energy is called thermodynamic stabilization, the process involving the reduction of GB mobility is called kinetic stabilization. Several alloys with exceptional structural stability or metastability at high temperatures have been discovered experimentally [14, 25–28] using these approaches, although in many cases, it is not always possible to fully separate the contributions of these two competing stabilization mechanisms.

Recently synthesized immiscible Cu-Ta alloys demonstrated extraordinary stability with enhanced mechanical strength and extreme creep resistance at high temperatures [29–35]. Although Cu and Ta exhibit negligible mutual solubility in the solid-state phase diagram, high-energy mechanical alloying drives a significant amount of Ta into a metastable FCC solid solution with Cu forming Cu-Ta alloys [29, 30]. However, due to the lack of mutual solubility, Ta atoms precipitate predominantly along the GBs and triple junctions in the form

1

of nanometer-scale coherent clusters separated by large areas of pure Cu boundaries instead of distributing uniformly as explained by the classical segregation model. These clusters impose a strong resistance to the GB migration and eventually prevent grain growth by the Zener pinning mechanism [32]. As the Ta clusters occupy only a small fraction of the GB area, substantial reduction of the GB energy as expected by the thermodynamic stabilization model is limited. Thus, Cu-Ta alloys serve as a perfect system for understanding kinetic grain stabilization phenomena, and a firm understanding of physical mechanism governing within it may provide essential knowledge to design other metallic alloys for structural applications at high temperatures. Hence, the dissertation was carried out on Cu-Ta alloys using atomistic computer simulations to understand the physical phenomena leading to unique properties such as thermal stability, high mechanical strength, small strain-rate sensitivity index, and excellent creep resistance.

With a high fidelity interatomic potential, atomistic simulations can accurately explain the physical theory and predict experimental results generating data that are hard to measure experimentally. New potential having high accuracy and reliability has been developed recently by Purja-Pun et al. [32] for describing the interatomic interactions of Cu-Ta system using angular dependent potential (ADP) formalism [36]. This potential was fitted to a large number of experimental properties and the results of first-principle calculations. The availability of this new realistic potential has motivated us to perform large scale atomistic simulations to investigate the kinetic and mechanical properties of Cu-Ta alloys.

Previous atomistic simulations [29, 32] have confirmed the formation of nanometer-scale Ta clusters inside the nanograins and especially at GBs, with their size distribution being consistent with experimental data obtained by atom probe tomography [33, 34]. Importantly, both simulations and experiments have shown that adding more Ta into the alloy only increases the number density of clusters with little effect on their size distribution, and these clusters drastically reduce grain growth rate. These simulations were performed on polycrystalline samples and probed a typical behavior of a polycrystalline aggregate. Since a polycrystal is made up of grains having random orientations, the GBs are of mixed

type and are affected by multi junctions. As different sections of the boundaries experience varying amounts of driving forces, the interaction of GB with solutes becomes much more complicated to characterize comprehensively. Thus, part of the dissertation is focused on atomistic simulations of an individual GB with particular crystallography to understand the GB-cluster interactions in detail. Of the several driving forces that could be implemented in molecular dynamics (MD) simulations for GB motion, shear coupled [37] and capillary driven [38] GB migration are implemented for studying GB-cluster interactions. With these simulations, we will reveal quantitatively that the outstanding thermal stability of the Cu-Ta alloys is primarily due to the kinetic factor, namely, the Zener pinning by Ta clusters.

Experimental observations have also revealed the presence of Ta clusters with varying sizes ranging from atomic clusters to much larger nanometer-scale Ta precipitates and phases coherent (FCC) or incoherent (BCC) to Cu crystal lattice [35, 39]. These clusters were observed to emit enormous dislocation activities in the Cu matrix. As the high strength and stability at elevated temperatures are influenced not only by the retention of the grain size but also by the accumulation of dislocations within the grain interior, it is essential to investigate the stability of Ta phases, interface behavior and microstructural evolution under intense heating. Hence, the dissertation conducted a systematic molecular dynamics (MD) study of Ta phases embedding different sizes of Ta nanoclusters in the Cu matrix and explained the microstructural manifestation observed in experiments.

Nanoclusters are composed primarily of Ta, defects, or random alloy. Some of these clusters are observed to have a core-shell type structure with Cu atoms embedded as core and Ta as shell [39]. Core-shell type nanoclusters have recently been attributed to the excellent strength and ductility of molybdenum alloys [40] and steels [41]. The dissertation explored the formation mechanism of core/shell Ta structure in Cu-Ta alloys using Monte Carlo (MC), molecular dynamics (MD), accelerated molecular dynamics (AMD), and hybrid MD simulations. The formation mechanism of core/shell structure can be explained by a redistribution of Ta atoms aided by Cu diffusion and crystallization achieved through the

coarsening of redistributed neighboring atoms in the amorphous Cu-Ta solution as.

Nanocrystalline materials usually display extreme superplastic behavior with a higher strain rate sensitivity (SRS) index (>0.3) when subjected to elevated temperatures or high strain rates. With the presence of Ta clusters in Cu-Ta alloys, investigation of their deformation mechanism at higher temperatures is of vital concern to see whether there is any strain hardening and elevated SRS behavior. Thus, the compression simulations were performed over a broader range of deformation rates (10^6 -10^{10} s^{-1}) at two different temperatures, 300 K and 1000 K respectively, to understand the flow stress of the material. With systematic simulations, we will show that the extreme SRS behavior in Cu-Ta alloys is unattainable, and the mechanism driving this unexpected trend is related to the reduction of grain boundary sliding and rotation through GB-Ta clusters interaction.

In general, the mechanical behavior of material changes with time and exhibits creep phenomena when exposed longer time to the stress lower than the yield stress at higher homologous temperatures. However, Cu-Ta alloy is a creep resistant material with creep rates [39] comparable to Ni-based single crystal superalloys (10^{-8} s^{-1}) [42] lying at the forefront in superior tensile creep behavior. The dissertation sheds light on the mechanism of creep resistance and explains the role of Ta clusters in the microstructural evolution of grain and interfaces.

The outline of the dissertation is as follows. Chapter 2 describes fundamental physics, background information, and methodology used in this work. In chapters 3 to 8, the simulation results are discussed and compared with experimental observations. Finally, a summary of different projects is presented in chapter 9.

Chapter 2: Theoretical background

2.1   Cu-Ta alloys

Cu-Ta alloys are an immiscible system of Cu and Ta elements lacking mutual solubility in the equilibrium solid-state phase diagram [43]. These constituent elements have different crystalline structures as Cu-FCC and Ta-BCC with significantly different melting temperatures viz; 1356 and 3290 K, respectively [44]. Although the Cu-Ta system does not form any compounds for all possible composition range, several processing techniques such as mechanical alloying, sputtering, vapor deposition, and powder technologies could produce Cu-Ta alloys forcing Ta atoms into FCC Cu lattice forming metastable FCC solid solution [29, 30].

A metastable Cu-rich solid solution can accommodate up to 10-20at.%Ta with higher concentrations causing amorphization [45–49]. During the subsequent thermal processing, Ta atoms precipitate from the solution in the form of nanometer-scale coherent FCC clusters. Even though some of these clusters eventually lose coherency with Cu and grow into larger particles of BCC Ta, an array of coherent Ta nanoclusters helps in attaining excellent thermal stability of the mechanically alloyed Cu-Ta alloys than Cu based alloys [33, 34, 50]. These clusters impose a strong resistance to GB migration and eventually pin GBs in place by the Zener mechanism [32]. No structural changes were experimentally observed in Cu-Ta alloys with 2-20 nm Ta particles and 200 nm Cu grains when annealed for 10 hours at 1173 K [51].

In addition to the Hall-Petch mechanism of GB hardening [52–54], the clusters located at the GBs increase their resistance to dislocation transmission and GB sliding. The clusters located inside the grain also contribute mechanical strength by restraining dislocation glide and twinning. For example, a Cu-Ta alloy with a grain size of around 100-200 nm is stronger

than pure Cu with a grain size of about 5 nm, leading to a more favorable combination of strength and ductility [34]. Thus, Cu-Ta alloys present significant technological and scientific interest for high-temperature, high-strength structural applications.

Some of the superior experimentally measured properties of Cu-Ta alloys are 0.6-1.1 Gpa yield strength, 10-25% elongation, 1.8-5.0 Gpa hardness, 40-70 (%ICAS), and 150-280 (W/mK) thermal conductivity [55]. The other excellent properties of Cu-Ta alloys are high corrosion and wear resistance, higher spall strength, lack of superplastic behavior, low strain-rate sensitivity, and superior creep resistance [56–59]. Multilayer Cu/Ta system is also used in semiconductor devices to improve the service performance of interconnects in large scale integrated circuits [60, 61].

Few semi-empirical potentials describing the interatomic interactions of the Cu-Ta system are available for running atomistic simulations [32, 62–64]. These potentials were developed using a different fitting procedure such as Finnis-Sinclair (FS), embedded-atom (EAM), and angular-dependent potential (ADP) method [36, 65, 66]. As the ADP potential format is believed to more appropriate for BCC transition metals, we used recently developed ADP potential [32] fitted to a large number of experimental properties and the results of first-principle calculations. The ADP potential is a generalization of EAM potential with additional bonding vectors.

2.2   Grain boundary (GB)

GB is an interface between differently oriented crystallites of the same material (Fig. 2.1a). It plays a vital role in the physical behavior of polycrystalline materials due to the excess free energy associated with the distortion of crystal structure across the boundary [67, 68]. Many aspects of materials properties and performance, such as yield strength, creep, fracture, and corrosion, are directly affected by GB properties, and their mobility controls microstructural evolution such as recrystallization [69, 70], grain growth [71] and plastic deformation [72, 73]. Precipitations of second phases at GB are also influenced by their energy, structure, and

6

distribution [74].

GB is defined by five macroscopic parameters, of which 3 are rotation parameters that describe the lattice orientation of two adjacent grains, and 2 are unit vectors that define the spatial orientation of the boundary plane [75]. It is also specified in terms of the rotation axis common for both adjoining grains and a rotation angle known as a misorientation angle, which brings both grains in perfect matching. GBs are called tilt (Fig. 2.1b) or twist boundaries (Fig. 2.1c) depending on whether the rotation axis (uvw) is perpendicular or parallel to the GB normal ($\hat{n}$) and mixed boundaries when the interface does not fit any of these relationships. While tilt boundaries consist only edge dislocations, twist boundaries are made up entirely of screw dislocations. For tilt boundaries, if the mirror symmetry is satisfied between two adjacent grains across the boundary plane, it is called symmetrical tilt boundary, while all other configurations are called asymmetrical tilt boundaries. When the misorientation between two grains is relatively small ($<15^0$), a grain boundary is described by a discrete array of dislocation structures and is called a low-angle grain boundary (LAGB). GBs having high misorientation are called a high-angle grain boundary (HAGB) and posses complicated structure. The structure of GB is described by coincidence site lattice (CSL) or displacement shift complete (DSC) lattice construction in both neighboring crystallites.
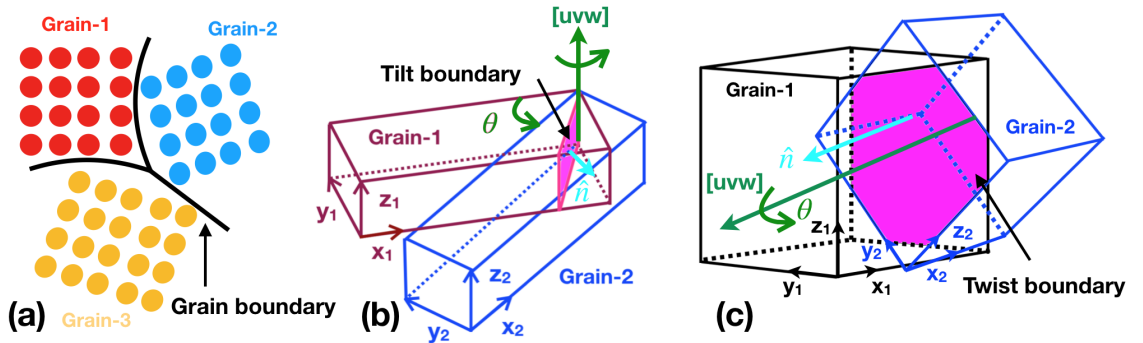
Figure 2.1: Schematic showing (a) grain boundaries and two common classes of grain boundaries (b) a tilt grain boundary (c) a twist grain boundary.

Theoretically, the energy of LAGB is described by Read and Shockley dislocation model [76], which estimates the energy based on the dislocation density and core energy of dislocations, and models employing thermodynamic considerations of an interface such as Herring equation [77] based upon the dihedral angles formed by the grain boundaries junctions. Computationally, GB energy is determined by first-principles density functional theory (DFT) calculations, Monte Carlo (MC) [78], molecular dynamics (MD) [79,80], and phase-field simulations [81]. Atomistic simulations have provided crucial insights into the GB structure [37,82], energies [37,83,84], mobilities [85–90], and mechanisms of GB migration [37]. The ground-state structure of the GB is determined by static minimization of the total potential energy to local atomic displacements and relative translations of one grain on another neighboring grain [82,91].

2.3 GB motion

GB undergoes motion at elevated temperature or by application of external loading or stress. The motion accompanied by deformation of its structural units may be normal motion in which the GB moves in its normal direction, coupled motion where the grain translates parallel to the GB plane moving the GB in normal motion, sliding where one grain translates on another across the GB or rotation [92].

Coupled motion is usually caused by applied shear stress. For plane GB, applied shear stress translates grain parallel to the GB plane and moves the GB in normal direction. The motion is characterized by a coupling factor β defined as the ratio of the tangential grain translation velocity $v_\parallel$ to the normal GB velocity v_n i.e., $\beta = v_\parallel / v_n$. In symmetrical tilt [100] GBs, there are two coupling modes with ideal coupling factors defined by

$$\beta^{<100>} = 2tan\left(\frac{\theta}{2}\right)$$
$$\beta^{<110>} = -2tan\left(\frac{\pi}{4} - \frac{\theta}{2}\right)$$

(2.1)

where θ is the misorientation angle [37]. MD simulations have demonstrated that GBs with θ closer to 0^0 couple in <100> and those having closer to 90^0 couple in <110> mode. The transition from one mode to another occurs around tilt angle 36^0, and GBs with θ close to 36^0 display dual behavior spontaneously switching between two modes. The coupling depends strongly on the tilt angle and the deformation mode, however at high temperatures, the coupling is gradually replaced by sliding for large misorientation angle [37]. Shear stress applied along a curved GB also undergoes coupled motion but accompanied by grain rotation. For the stress-driven motion, the drag pressure is defined by

$$P = \beta\tau \tag{2.2}$$

where τ is the average shear stress required for sustaining a constant GB velocity [92–94].

At higher temperatures, substantial grain growth or loss takes place through boundary migration to reduce excess free energy by reducing the total area of the grain boundary. The driving force for grain growth is capillary nature and depends on the excess free energy of GBs. For a circular GB, the driving force is by

$$P = \frac{\gamma}{r} \tag{2.3}$$

where γ is the excess energy associated with GB and r is the radius of curvature [93]. The boundary undergoes grain shrinkage coupled with inner grain rotation and the misorientation angle increases or decreases towards 36^0.

2.4 Grain stabilization

The velocity of grain growth may be expressed through a linear relationship

$$V = M.P \tag{2.4}$$

9

where M is the GB mobility, and P∝γ is the driving force. This relation makes evident that reduction in the GB mobility or/and driving force helps in attaining grain stabilization by decreasing the grain growth. In practice, grain stabilization is achieved through the addition of impurities on pure metals.

There are two ways in which grain stabilization is achieved. The first is the thermodynamic approach in which the driving force for grain growth is lowered by reducing excess free energy through solute segregation across the GBs. Starting from the Gibbs adsorption equation, Weissmüller [95] noted that the GB energy (γ) on solute segregation could be expressed as

$$\gamma = \frac{dG}{dA} = \gamma_0 - \Gamma(\Delta H^{seg} - KTlog[x]) \tag{2.5}$$

where γ_0 is the initial grain boundary energy of pure matrix, ΔH^{seg} is the enthalpy change for a particular solute concentration X at temperature T, dG is the total free energy change of the system when the GB area changes by dA through solute segregation. Therefore, when solute segregation results in γ=0, grain growth is firmly prevented with dG=0. However, in real practice, there exists a minimum as opposed to a maximum in the GB free energy with solute segregation, and hence, a metastable equilibrium state can be achieved to the grain-size stabilization. Several theories have also been proposed to evaluate segregation enthalpy correlating with elastic strain, chemical interaction, surface or interfacial energy and to reduce excess GB energy to zero at different grain sizes and temperatures; for example Mclean, BET, Fowler-Guggenheim, Guttmann [96], Wynblatt and Ku [97], Darling et al. [26] and Murdoch and Schuh [68]. This approach has been successful in achieving thermal stability in some systems such as Fe-Al [25], Fe-Zr [26], Cu-Zr [27], W-Ti [98], and Cu-W[28].

The second is the kinetic approach in which the GB mobility is reduced by solute drag [17–21] or Zener pinning [22–24] by small precipitates of the second phase. According to the Zener pinning model, pinning pressure resisting the GB motion is exerted by the solute while interacting with the boundary. The dragging force exerted by a spherical particle of

radius R is

$$f = 2\pi R\gamma sin\theta cos\theta = \pi R\gamma sin2\theta \tag{2.6}$$

where θ is the contact angle [24]. This force reaches maximum value f_{max}=πRγ at θ=45^0. For the GB having an area A and interacting with N obstacles, the maximum pinning pressure is then given by

$$P = \frac{\pi R\gamma N}{A} \tag{2.7}$$

Thus, the GB motion is inhibited when the driving pressure causing grain growth is counterbalanced by the pinning pressure exerted by the solute.

2.5   Deformation

Deformation is a change in volume or shape of material under external loading or applied stress. When the applied stress displaces atoms into new equilibrium positions from their original positions, change in shape is unrecoverable and refereed as inelastic deformation. The inelastic deformation is termed time-independent plastic deformation when the applied stress is greater than or equal to the yield stress of the material and time-dependent creep when exposed longer time to the stress lower than the yield stress at high homologous temperature.

Plastic deformation in pure metals and alloys usually occurs through slip and twinning mechanisms [99]. Slip is the sliding of planes of atoms over one another through the generation of a linear defect called dislocation. It occurs along specific crystallographic planes called slip planes, and directions called slip directions. The slip planes and directions are characteristic of the crystal structure of materials and take place on the plane having a densest pack of atoms in the close-packed directions. In FCC metals, slip occurs on the {111} planes in the <110> directions whereas in BCC metals, the slip planes are {110}, {112} or {123} with slip directions <111> [100]. Similarly, slip occurs in the HCP metals

on the basal (0001) plane in the $<11\bar{2}0>$ directions. The amount of slip during the deformation is defined by the Burgers vector, which can be determined by making a closed circuit around the dislocation.

Dislocations generated during slip can be edge, screw, and mixed types. When the Burgers vector is perpendicular, parallel, or randomly oriented to the dislocation line, the corresponding dislocation is edge, screw, or mixed dislocation. While the edge dislocation causes axial distortion in the crystal lattice, the screw dislocation causes lattice rotation through the helical path. Dislocations may also dissociate into two Shockley partials, leading and trailing separated by the stacking fault. The stacking fault gets expanded as the leading partial propagates forward and gets removed at the instant trailing partial moves ahead following the leading partial. Frank's rule describes the splitting of dislocation into partial dislocation.

The sources of dislocations are Frank-Read sources, GBs, or interfaces [101]. Dislocations nucleated or emitted from these sources propagate freely across the grain and are absorbed by other GBs leaving traces of dislocation slip within the grain. GBs also inhibit dislocation transmission into another grain, causing dislocation pile up within the grain. This GB hindrance leads to the fact that the strength of the material increases with more grain boundaries. The resulting phenomenon is called the Hall-Petch effect [53] that defines an increase in yield strength with a decrease in grain size through the relation

$$\sigma_y = \sigma_0 + kd^{-1/2} \tag{2.8}$$

where σ_y is the yield stress, σ_0 is a material constant, k is a strengthening coefficient and d is the grain size. The Hall-Petch effect holds up to an experimental observation limit of 10 nm [2] grain size beyond which there arises inverse Hall-Petch behavior due to change in deformation mechanisms from dislocation glide and pile up processes to grain boundary rotation, sliding and viscous flow.

Deformation mechanisms in nanocrystalline materials (grain diameter <100 nm) are

mainly related to GBs activities with Frank-Read sources being prevented. The GBs activities involve dislocation emission and absorption, GB sliding, rotation, and migration. These activities depend on the grain boundary misorientation angle, strain energy density, and localization of stress state within the grain. Emission of dislocation promotes GB migration with rotation and facilitates grain growth or loss during deformation. GB sliding becomes prominent when dislocation emission is reduced, or dislocation pile up within the grain is limited by the grain size.

Twinning is another mechanism of deformation. In twinning, a group of atoms or a region of crystal lattice moves simultaneously parallel to the plane called twin plane and arranges in a mirror image of one another across it. In FCC, the twin plane is twist boundary when the misorientation angle between two grains is 60^0 with rotation axis <111> and tilt boundary when the misorientation angle between two grains is 70.53^0 with rotation axis <110>. Twinning occurs more quickly than slip and is more common in high-stress situations and few slip systems such as low symmetry crystals.

Creep deformation is broadly divided into two types of mechanisms called diffusion creep and dislocation creep [102]. Diffusion creep involves the movement of atoms by diffusion. Based on the diffusion path, diffusion creep is called Coble creep when it occurs occur predominantly through the GBs and Nabarro-Herring creep when it occurs predominantly through the grains themselves. Dislocation creep is a mechanism involving the motion of dislocations. Dislocations can move by gliding in a slip plane or by climb process via atomic movement or self-diffusion within the lattice. The amount of creep deformation with the movement of dislocations and diffusion of atoms can be expressed through the general creep equation

$$\dot{\epsilon} = C\sigma^n exp(-Q/kT) \tag{2.9}$$

where C is a constant, n is also a constant termed as stress exponent, Q is the activation energy (equal to the self-diffusion) of creep, σ is the applied stress, and kT has its usual meaning. In pure nanocrystalline material, the value of n infers the creep mechanism operating on it. The value of n is approximately 1 for diffusion creep and in the range 3-8

13

for dislocation creep.

2.6 Atomistic simulation methods

Atomistic simulation serves as a powerful tool for getting insights into the atomic events. It can accurately explain the physical theory and make an exact prediction of experimental measurements generating data that are difficult to measure experimentally. The approach in simulation methods may be quantum mechanical (QM) methods such as density functional theory (DFT) and quantum chemical calculations or classical methods such as molecular dynamics (MD) and Monte Carlo (MC) simulations. The advantage of QM methods over classical methods is that it gives highly accurate results with a precise assumption of atomic events, but it is computationally slow and handles only small system size. The classical methods are most efficient for the investigation of physical phenomena, which are inaccessible through QM simulation methods such as phase transformations, diffusion, microstructure evolution, plastic deformation, and fracture. This dissertation deals exclusively with classical MC and MD methods to understand grain stability, dislocation nucleation, mechanical strength and microstructure evolution of Cu-Ta alloys under heating and deformation.

The choice between two classical methods depends on the physical event under investigation. While MD simulation models static and dynamical behavior of the system with time-dependent response, MC simulation models system using random sampling and probability statistics. MC simulations cannot be used in situations that require a definition of time. Such examples include the determination of transport properties such as diffusion and viscosity coefficients. Although MC lacks an objective definition of time, it attains system equilibrium much faster than MD by sampling all configurational space where the atoms may be trapped in MD simulation, such as large energy barrier leading poor conformational sampling. Moreover, MC can only be used for simulations involving the addition and removal of atoms (Grand Canonical) and switching chemical species in a multi-component system.

14

In MD simulation, atomic movements are governed by classical equations of motion. It consists of step by step numerical solution of Newton's equation of motion

$$m_i \ddot{r}_i = -\frac{\partial U}{\partial r_i} + f^{ext} \tag{2.10}$$

where U is an interatomic potential, f^{ext} is an external force, m_i and r_i are mass and position of the ith atom. Trajectories of atoms are predicted from the current positions and velocities using different time integration algorithm such as velocity Verlet, Leapfrog, Beeman algorithms. Several software packages are available for carrying out MD simulations. However, this dissertation employs the molecular dynamics package LAMMPS (Large-scale Atomic/Molecular Massively Parallel Simulator) developed at Sandia National Lab. In LAMMS, atoms are treated as particles confined to a box of volume V and modeled through statistical ensembles such as NVE, NPT, NVT. While temperature is calculated from atoms velocities, pressure is determined from the volume of the simulation cell using statistical mechanics.

In MC simulation, an atom is randomly selected, and a trial move is executed by displacing it in a random direction by a small random displacement. The energy change ΔE associated with this move is then calculated, and the trial move is accepted or rejected with the following metropolis scheme:

1. If $\Delta E < 0$, accept the move unconditionally.

2. If $\Delta E > 0$

    (a) compute p= exp(-$\Delta E/kt$)

    (b) generate a random number r$\in$ [0,1)

    (c) if r $\leq$p, accept the move; otherwise reject it

The process is repeated until the system approach equilibrium in which all parameters randomly fluctuate around their average values. To generate nanocrystalline alloys having

15

the desired concentration of binary elements, semi-grand canonical Monte Carlo simulation is performed at the fixed chemical potential difference. In this method, the trail moves also include chemical switching from one atom type to another, keeping the total number of atoms fixed in the system. Also, it includes random changes in the dimensions of the simulation block with respective rescaling of atomic coordinates. The trial move is accepted with the probability

$$
P = \begin{cases} 1, & \Delta\Phi \leq 0. \\ exp(-\Delta\Phi/kt), & \Delta\Phi > 0. \end{cases} \tag{2.11}
$$

where

$$
\Delta\Phi = \Delta E + \Delta\mu_{\alpha\beta} + \frac{3}{2}kTln\frac{m_\alpha}{m_\beta} \tag{2.12}
$$

Here, ΔE is the total energy change in the trail move, k is the Boltzmann constant, α and β are the new and old chemical species of the tested atom, and m_α and m_β are the respective masses. In this approach, the chemical composition of the system is determined as a result of equilibration with the fixed potential difference $\mu_{\alpha\beta}=\mu_\alpha$-$\mu_\beta$. A better approach to achieve nanocrystalline alloy having desired chemical composition is composition controlled Metropolis scheme, where the chemical potential difference is adjusted through a feedback loop to achieve that composition.

$$
\mu_\alpha^{(i)} = \mu_\alpha^{(i-1)} - a\left(\frac{c_\alpha^{(i-1)} - c_\alpha^{(i-2)}}{2} - c_\alpha^{(0)}\right) \tag{2.13}
$$

where index i labels Monte Carlo steps, μ_α and c_α represents the current chemical potential and composition values of element α, and a is an adjustable parameter that affects computational efficiency but not the result of the simulation. This approach is much faster and efficient than semi-grand canonical MC simulations and doesn't require the knowledge of chemical potential difference. When the system reaches equilibrium, both the chemical

16

composition and the chemical potential fluctuate around equilibrium values. This dissertation utilizes composition controlled Metropolis scheme for generating various compositions of Cu-Ta alloys.

2.7   Grain orientation

Atomistic simulations are performed to understand and observe structural evolution in the system. There are many physical events involving structural evolution, such as precipitate formation, film deposition, mechanically driven grain growth, phase transformation, strain-induced deformation, severe plastic deformation. As the system undergoes microstructural evolution, it is essential to track and observe individual grains. Grains can be identified through the determination of the orientation matrix of each atom from the orientation vectors of neighboring atoms. Orientation matrix (g) describes the orientation of the sample coordinate system (C_s) with respect to the orientation of the crystal coordinate system (C_c) having unit vectors <100> as axes through the relation C_c=gC_s (Fig fig:orientation).

This dissertation has developed a parallel MPI code for the analysis of crystallographic orientations in nanocrystalline materials. This code is very efficient in handling large system size and can be used for identifying the crystallographic orientation of new grains nucleated in the simulation and their relationship with old grains. This code requires pre-processing of data first with OVITO to identify bond angle analysis and centrosymmetry parameter (CSP) of each atom. Interface atoms are then identified and avoided from orientation calculation using the bond angle parameter and a cutoff in the centrosymmetry parameter.

The orientation of remaining inner FCC crystalline atoms is calculated with the alignment of a direction vector of its 12 nearest neighbors [103]. For any directional vector, there exist four other directional vectors making approximately an angle of 60 degrees and residing in two separate {100} planes. Of these four-vectors, the resultant vector of a pair of vectors which are perpendicular to each other gives two <100> directions, and their cross product gives third <100> direction. This calculated orientation represents the <100> orientation in the sample coordinate system. Inversion of the matrix formed by arranging components

17

of <100> directions in the column elements gives the orientation matrix through the relation $g=C_cC_s{}^{-1}=C_s{}^{-1}$ as $C_c=I$ is an identity matrix in the crystal coordinate system. In other words, the orientation matrix is the matrix with row elements denoting the resolved components of a sample orthogonal basis.

As there are 24 rotational symmetries in FCC crystal, there exist 24 mathematically distinct but physically indistinguishable orientation matrix. Thus, the orientation matrix is uniquely defined by obtaining solutions through premultiplication of orientation matrix with 24 symmetry operators and finding the one with minimum angle of rotation. The trace of the premultiplied orientation matrix gives the angle of rotation through the relation $\theta=\cos^{-1}\left(\frac{trace-1}{2}\right)$. Miller indices of any arbitrary crystal are determined by multiplying the column elements of the minimum angle premultiplied orientation matrix with a suitable factor to convert it into whole number and dividing by their lowest common factor. The first, second, and third columns then represent the miller indices along x, y, and z directions of the simulation block. Changes in the lattice orientation of the grain from one crystal frame (g_A) to another crystal frame (g_B) can be determined from the misorientation matrix (g_{AB}) that defines transformation between two crystal frame through the relation $g_B=g_{AB}\times g_A$. The rotation angle and rotation axis of the minimum angle misorientation matrix (g_{AB}) defines the transformation two crystal frame.
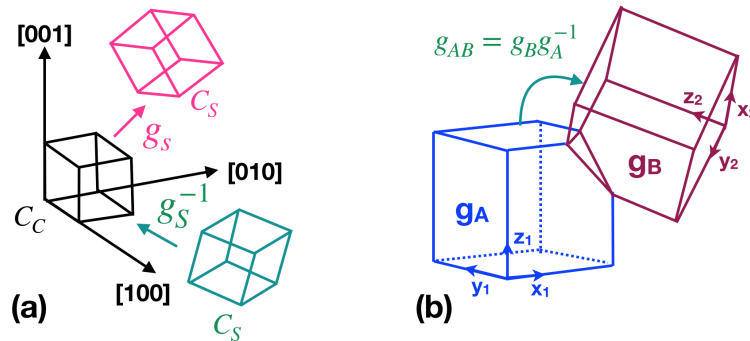
Figure 2.2: Schematic showing (a) transformation of grain relative to crystal coordinate system (b) transformation from one grain to another grain.

Chapter 3: Zener pinning of grain boundaries and structural stability of immiscible alloys

3.1 Introduction

Nanocrystalline alloys have attracted much attention over the past decades due to their high mechanical strength, corrosion and wear resistance, and other useful properties. These properties are primarily due to the presence of a large density of grain boundaries (GBs) in the material. In particular, the strengthening effect is caused by the difficulty of dislocation nucleation and glide inside the nano-grains and slip transmission across GBs. One of the obstacles to wider applications of nanocrystalline alloys is the tendency of nano-grains to grow at elevated temperatures (in some cases, even at room temperature). Due to the large specific area of GBs, their excess free energy creates a strong driving force for grain growth, causing deterioration of superior properties. Several approaches have been proposed for the stabilization of nano-grain structures. They can be broadly divided into two types: thermodynamic stabilization by reducing the GB free energy by solute segregation [12–16], and kinetic stabilization wherein the GB mobility is reduced by the solute drag effect [17–20] or Zener pinning by small precipitates of a second phase [22–24].

Cu-Ta nanocrystalline alloys have recently emerged as a promising class of materials for high-temperature, high-strength applications [16,29–31,33,34]. They belong to the category of immiscible alloys that combine high mechanical strength with extraordinary structural stability at high temperatures [5,12,16,29–31,33,34,50,104–106]. Although Cu and Ta have negligible mutual solubility in the solid-state, high-energy mechanical alloying can force a significant amount of Ta into unstable FCC solid solution with Cu. During the subsequent thermal processing, Ta atoms precipitate from the solution in the form of nanometer-scale coherent clusters [30]. Although some of these clusters eventually lose coherency with Cu

and grow into larger particles of BCC Ta, it is the array of coherent Ta nanoclusters that are believed to be responsible for the excellent thermal stability and strength of the mechanically alloyed Cu-Ta alloys [32–34]. The clusters impose a strong resistance to GB migration and eventually pin GBs in place by the Zener mechanism [22–24]. In addition to the Hall-Petch mechanism of GB hardening [52,54], the clusters located at the GBs increase their resistance to dislocation transmission and GB sliding. The clusters located inside the grains can also contribute to the strengthening by restraining dislocations glide and twinning. As a result, a Cu-Ta alloy with a grain size of around 100-200 nm is stronger than pure Cu with a grain size of about 5 nm, leading to a more favorable combination of strength and ductility [34].

Previous atomistic simulations [29,32] have confirmed the formation of nanometer-scale Ta precipitates (clusters) inside the nano-grains and especially at GBs, with their size distribution being consistent with experimental data obtained by atom probe tomography [33, 34]. Importantly, both simulations and experiments have shown that adding more Ta into the alloy only increases the number density of the clusters with little effect on their size. The simulations have also confirmed that the Ta clusters drastically reduce the grain growth rate in agreement with experiments and significantly increase the tensile strength of the material.

The previous simulation work [29, 32] was performed on polycrystalline samples and probed an average behavior of a polycrystalline aggregate. In this paper, we report on atomistic simulations of an individual GB with a particular bicrystallography. The goal is to understand the GB-cluster interactions in greater detail and demonstrate quantitatively that such interactions are well-consistent with the Zener model of GB pinning. This agreement provides strong evidence that the outstanding thermal stability of the Cu-Ta alloys is primarily due to the kinetic factor, namely, the Zener pinning by Ta clusters.

3.2   Methodology

Atomic interactions were described by the recently developed angular-dependent inter-atomic potential for the Cu-Ta system [32]. The simulations combined molecular dynamics (MD) employing the LAMMPS code [107] and Monte Carlo simulations implemented in the parallel MC code developed by V.Yamakov (NASA). A prescribed amount of Ta was introduced into Cu by the composition-controlled MC algorithm utilized in our previous work [91, 108]. This algorithm brings the system to thermodynamic equilibrium at a given temperature, given average chemical composition, and imposed zero-stress conditions. A trial move of the MC process included a small random displacement of a randomly selected atom in a random direction and a random re-assignment of its chemical species to either Cu or Ta. The trial moves also included random changes in the dimensions of the simulation block with respective rescaling of atomic coordinates. The trial move was accepted or rejected by the Metropolis algorithm. In single-crystalline samples, the Ta atoms inserted by the MC simulation always appeared in the form of randomly distributed nanoclusters with FCC structure coherent with the Cu-matrix. In the presence of a GB, the clusters had approximately the same size but formed predominantly at the GB. Thermodynamically, the nanocluster form of Ta is metastable in both MC simulations and experiments. The nearly constant cluster size is apparently dictated by a local energy minimum optimizing the solubility energy, elastic strain energy (Cu and Ta have a large atomic size mismatch), and the surface tension, somewhat similar to Guinier−Preston zones in Al(Cu) alloys. The extraordinary thermal stability of this metastable state suggests the existence of a large energy barrier separating it from the more stable structure composed of large particles of BCC Ta. For comparison, we modeled the unstable solid solution obtained by mechanical alloying. The latter was obtained by randomly substituting Cu atoms by Ta to create a uniform mixture with a set chemical composition.

The boundary studied here was the $\Sigma 17(530)[001]$ symmetrical tilt GB with the misorientation angle of θ=61.93 (Σ being the reciprocal density of coincident sites, [001] the tilt
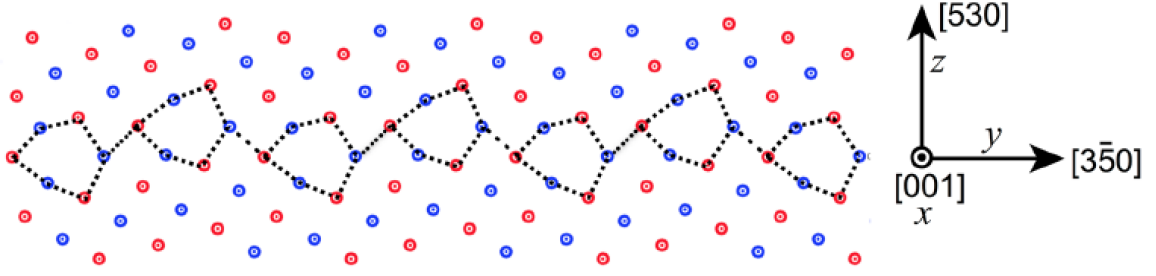
Figure 3.1: Symmetrical tilt GB Σ17(530)[001]. GB structure is composed of kite-shaped structural units. Z-axis is normal to the GB plane (x-y plane) with the x-direction oriented along the [001] tilt axis.

axis and (530) the GB plane). The GB structure consists of identical kite-shape structural units arranged in a zigzag array, as shown in Fig. 3.1. The grains had an approximately square cross-section parallel to the GB plane and were longer in the z-direction normal to the GB plane. The boundary conditions were initially periodic in all three directions. Two simulation blocks were utilized: a smaller one with the approximate dimensions 6.3×6.3×84.4 nm (2.63×10^5 atoms) and a bigger one with the approximate dimensions 21.3×21.3×58.7 nm (2.06×10^6 atoms). By default, the results reported below were obtained with the smaller block unless otherwise indicated. Ta was introduced into the bicrystal by either MC simulations or random substitution, as mentioned above.

To induce GB motion, a shear strain was applied parallel to the GB plane. To this end, free surfaces were created in the z-direction. Atoms within a 1.5 nm layer near one surface were fixed, while a similar layer near the second surface was translated as a rigid body parallel to the GB plane and normal to the tilt axis with a constant velocity $v_\parallel$. All other atoms were dynamic. The translation velocity was chosen between 0.02 and 10 m/s. This simulation scheme explores the shear-coupling effect [37, 109], in which normal GB motion produces shear deformation of the region it traverses; conversely, relative translation of grains parallel to the GB plane with some velocity $v_\parallel$ causes normal GB motion with a velocity v_n. The shear-coupling effect is characterized by the coupling factor $\beta = v_\parallel / v_n$, which

for perfect coupling is a geometric parameter that depends only on the bicrystallography of the boundary. For the $\Sigma 17$ GB studied here, the geometric coupling factor is $\beta=2\tan(\theta/2-\pi/4)=-0.496$. The normal driving force exerted on the GB is $p=\beta\tau$ [92,94], where $\tau=\sigma_{yz}$ is the shear stress parallel to the GB plane created by the grain translation. During the MD simulations, the position of the moving GB was tracked by finding the peak of potential energy (pure Cu and Cu-Ta with clusters) or bond-angle parameter (solid solution) in the snapshots using the OVITO visualization software [110]. The shear stress was computed using the standard virial expression averaged over the entire system.
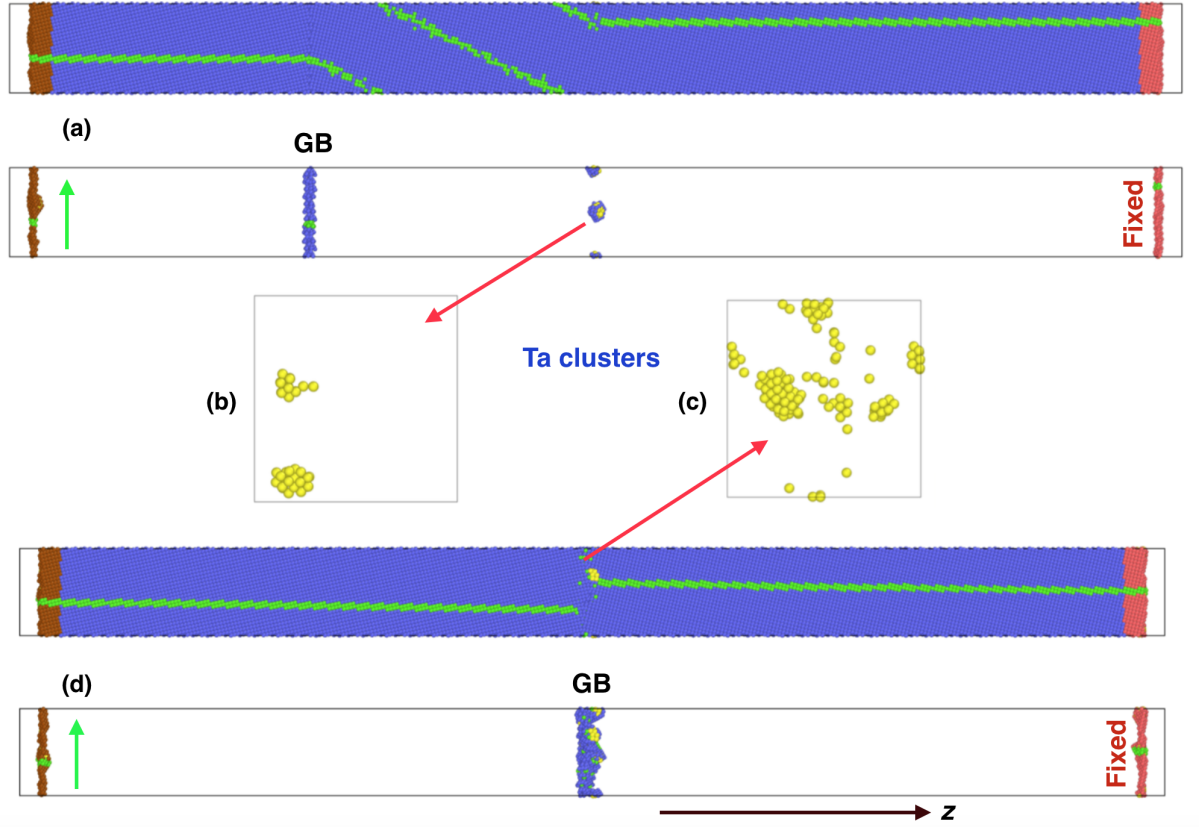
Figure 3.2: MD simulation of the stress-induced motion of Cu $\Sigma 17$ GB in the presence of Ta nanoclusters at 900 K. Right end of the simulation block is fixed while left end moves with the speed of 1m/s in the direction indicated by green arrow. (a) GB position after unpinning from the clusters in 0.015 at.%Ta alloy. (b) Ta clusters left behind the moving GB boundary. (c) Ta clusters in the sliding mode. (d) GB sliding in 0.055 at.%Ta alloy.

23

3.3 Results

3.3.1 Effect of Ta clusters on boundary migration

The Ta clusters had approximately the same size distribution regardless of the average alloy composition, which is in agreement with previous work [32–34]. The temperature dependence of the distribution was also small. For example, at the temperature of 900 K, the clusters had a typical size of 0.75 nm and contained around 20-25 atoms, although some of the clusters contained up to 50 atoms. When Ta concentration was small, the GB could easily unpin from the clusters and move through pure Cu driven by the applied stress (Fig. 3.2a). At 900 K, the stress required for the GB motion was less than 9 MPa (Fig. 3.3a). The coupling factor determined from $v_\parallel$ and v_n was close to the ideal geometric value (Fig. 3.3b).
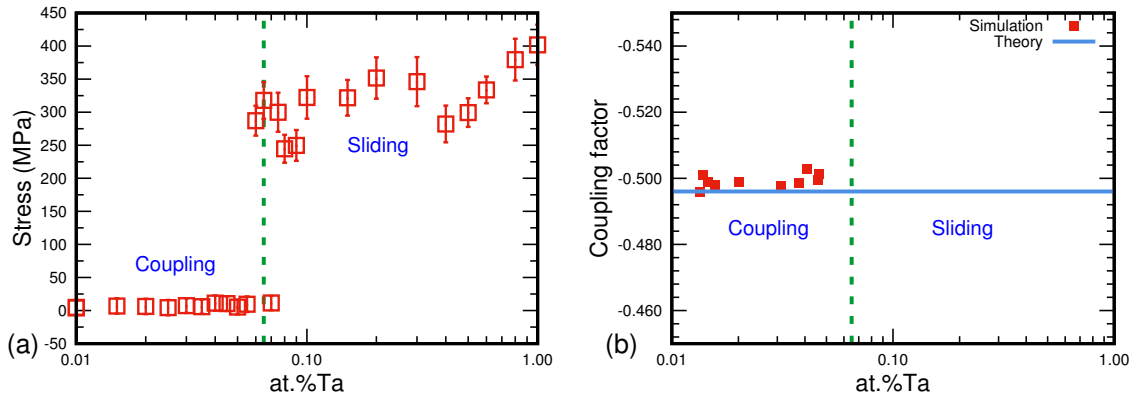
Figure 3.3: Mechanical responses of the Cu $\Sigma17$ GB in the presence of Ta nanoclusters at 900 K. (a) Shear stress τ as a function of the average alloy composition. The error bars indicate the standard deviation of the stress from the average value during the simulations. (b) Coupling factor β as a function of the average alloy composition; the blue line marks the ideal value of β. The vertical yellow line indicates the transition from coupling to sliding mode.

After the composition reached about 0.06 at.%Ta, the GB could no longer unpin, and the GB response to the applied shear switched from coupled motion to sliding. At 900 K, the sliding stress is approximately 300-400 MPa. This is an unusual type of sliding in which the

24

GB contains a significant density of nanoclusters that resist the sliding process. Examination of simulation snapshots showed that the sliding process continuously separated individual Ta atoms from the clusters or merged the clusters together (Fig. 3.2c). Nevertheless, the clusters not only survived but also preserved approximately the same average size, demonstrating remarkable stability. The transition from coupling to sliding occurred when the GB area per cluster was about 8-10 nm^2. In alloys with larger Ta concentrations when the GB slid, this area reduced to 4 nm^2 or less.

To examine the GB-cluster interactions in more detail, the boundary which had unpinned from the clusters and traveled some distance into a Cu grain was stopped and set to move back toward the clusters by reversing the direction of the grain translation with the same magnitude $v_{\parallel}$. Typically, the boundary impinging on the clusters would stop momentarily but then unpin and continue traveling into the other grain. Next, the direction of GB motion was reversed again, and the boundary was driven back through the same set of clusters a second time, and then again several times. Interestingly, during this process, the coupling factor of the GB remained close to ideal, demonstrating remarkable robustness of the shear-coupling effect. Indeed, each time the GB would break through the set of clusters, the latter "punched holes" in the GB structure. Nevertheless, the boundary would quickly heal the holes, recover the initial atomic structure, and regain the ability to couple to shear stresses with the same coupling factor.

Fig. 3.4 shows typical examples of the shear stress as a function of time as the boundary passes through the clusters twice. To demonstrate that this stress behavior is independent of the system size, simulations were repeated in the simulation block with a larger GB area, as illustrated in (Fig. 3.4b). Note the existence of two stress peaks with opposite sign each time the boundary passes through the clusters. This behavior is exactly what is expected within the Zener model of GB pinning. Indeed, as shown schematically in Fig. 3.5, the GB-obstacle interaction has two stages: attraction and pinning. As soon as the moving GB touches the spherical obstacle, the surface tension begins to pull the GB towards the sphere (Fig. 3.5a). As a result, the boundary is attracted to the obstacle. Once the boundary has
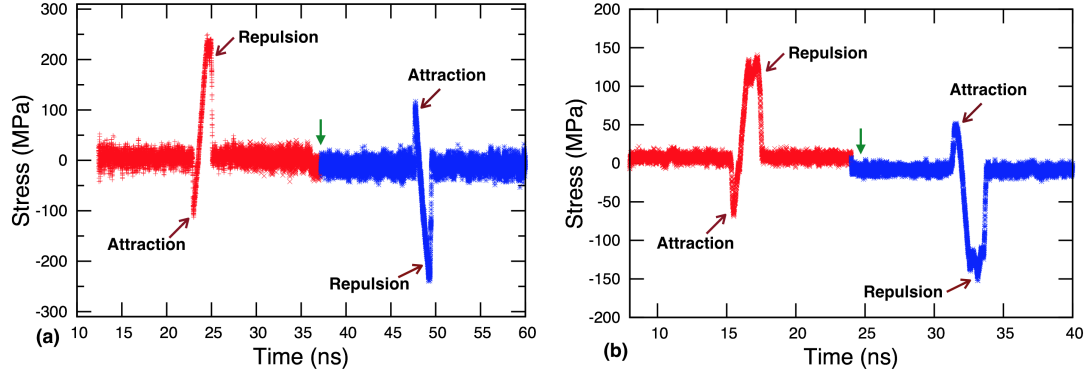
Figure 3.4: Time dependence of shear stress as the GB passes through a set of Ta clusters twice at 900 K. Green arrow shows the point of reversal of the GB motion. (a) Alloy with 0.031 at.%Ta. (b) Alloy with 0.027 at.%Ta in the larger simulation block.
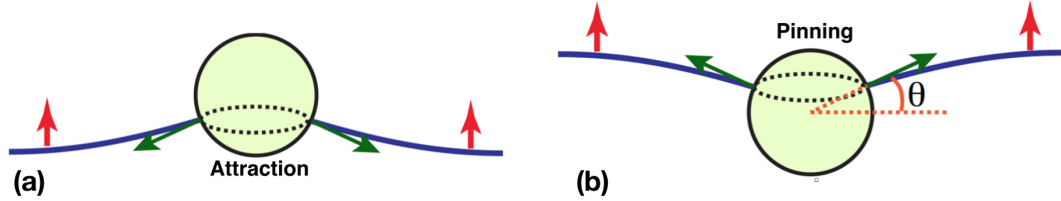
Figure 3.5: Interaction of a moving GB with a spherical obstacle in the Zener pinning model. (a) The boundary moving up comes in contact with the obstacle. The GB tension (shown by arrows) is pulling the GB towards the obstacle, creating an attractive force. (b) The boundary is trying to break away from the obstacle and move on. The capillary force is pulling the boundary back, creating a pinning force. The vertical arrows indicate the direction of GB motion.

passed through the obstacle and is trying to move on, the contact angle changes sign and the surface tension now pulls the boundary back (Fig. 3.5b). This creates a pinning force that must be overcome for the GB to separate from the obstacle.

Fig. 3.6 demonstrates that the local GB curvatures near the clusters are qualitatively consistent with the attraction and pinning stages of the Zener model. Furthermore, a closer examination of Fig. 3.6 and the original movie show that the moving GB first touches
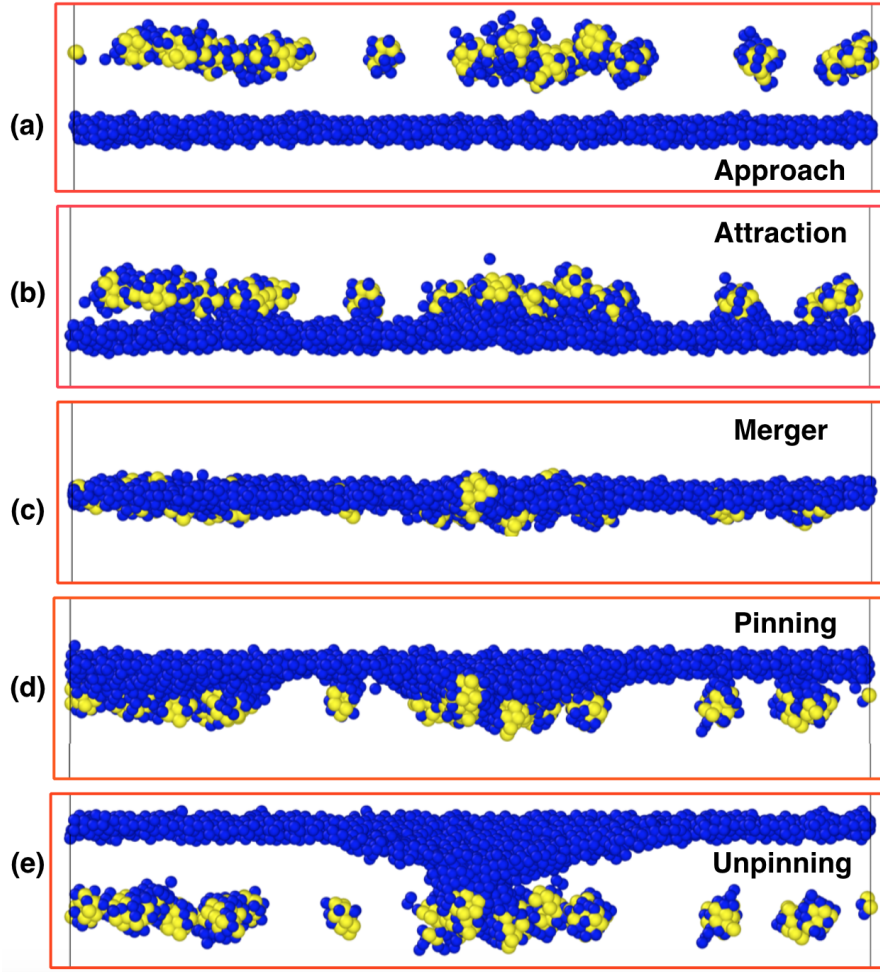
Figure 3.6: Interaction of a GB moving upward with Ta clusters at 900 K. (a) The GB approaches a set of clusters from below. (b) The capillary forces attract the GB as soon as it touches the clusters. (c) The GB has absorbed all clusters. (d) The capillary forces pull the GB back as it tries to move on. (e) Most of the GB has unpinned from the clusters. Note that the GB curvature is similar to the one shown schematically in Fig. 3.5. The alloy composition is 0.027 at.%Ta and the simulation was performed in the large block.

one cluster, which then pulls the GB forward, and it begins to touch neighboring clusters one after another. As a result, the GB-cluster contacts quickly spread over the boundary. Similarly, the unpinning process starts with the unpinning of one cluster, followed by the unpinning of neighbors until the GB finally separates from all clusters. This mechanism is similar to the operation of a ziplock and can be called the zipping/unzipping mechanism.

We can now explain the double peak of the stress in Fig. 3.4. When the GB is away from the cluster, the imposed grain translation creates a shear stress τ pointing in the direction of translation, which we count as positive. When the boundary comes in contact with the clusters, the capillary force starts pulling it in the direction of motion. Due to the coupling effect, this accelerated normal motion produces an additional relative translation of the grains in the direction of the applied translation. The velocity of this additional translation soon exceeds the imposed velocity (in this case, 1 m/s), and the shear stress reverses the sign. This is the origin of the negative peak in Fig. 3.4. After the GB-cluster interaction switches to pinning, the capillary force opposes the GB motion. Accordingly, the imposed grain translation increases the shear stress until a critical value is reached at which the GB unpins. This produces the second stress peak in Fig. 3.4.

More complex interactions of the GB with the clusters were also observed. For example, in alloy compositions near the coupling to sliding transition (Fig. 3.3), the boundary spends a few ns in the sliding mode but eventually unpins and moves into one of the grains. When sent back towards the same set of clusters, the GB is stopped by them and begins to slide. It never breaks through the clusters into the second grain for as long as we can run the simulations (>55 ns). When the direction of grain translation is reversed again, the GB unpins and moves back into the initial grain. In other words, the GB unpins from the clusters in one direction but not in the other, even after several attempts. A detailed mechanism of this asymmetry of pinning remains unclear and calls for future work.

The computed stress profiles (Fig. 3.4) offer an opportunity to test the Zener model against the simulations. The dragging force exerted on the GB by a spherical obstacle of a radius R is [24] f=πRγsin2θ, where θ is the contact angle (Fig. 3.5). This force reaches the maximum value f$_{max}$=πRγ at θ=45^0. For a GB of an area A containing N obstacles, the force per unit area is F$_{max}$=πRγN/A. The GB unpins when its driving force p reaches F$_{max}$, giving the unpinning condition πRγN/A=$|\beta|\tau_{max}$. Here, τ_{max} is the stress of unpinning given by the respective peak in Fig. 3.4. In the simulations, β, N and A are known. The cluster radius can be evaluated as the radius of an equivalent sphere with the same volume

as an average cluster: R=$(3\Omega\ n/4\pi)^{1/3}$, where n is the average number of atoms in a cluster and Ω is the atomic volume. Having this data, we can back-calculate the GB free energy:

$$\gamma = \frac{A|\beta|\tau_{max}}{\pi RN} \tag{3.1}$$

Table 3.1 summarizes the calculations from equation 3.1 for different alloy compositions and two different sizes of the simulation block. Although the number of Ta clusters in the GB varies between 2 to 31, the values of the GB free energy recovered from equation 3.1 have a small scatter around the average value of 0.908 J/m². For comparison, the energy of this boundary at 0 K is 0.856 J/m². The two numbers are remarkably close. Ideally, the GB free energy at 900 K is expected to be lower than at 0 K. On the other hand, the estimates in Table 1 refer to a nonequilibrium boundary damaged by the clusters and curved near the pinning points, the factors which likely raise its excess free energy. Given these circumstances and the fact that Eq. 3.1 relies on the assumption of a perfectly spherical obstacle and other approximations, the consistency of the γ values listed in Table 3.1 is very encouraging and can be taken as a validation of the Zener model by the simulations.

Table 3.1: Calculation of the GB free energy at 900 K from the Zener model of pinning.

Alloy composition (at.%Ta)	n	A (nm²)	R (nm)	τ_{max}(GPa)	γ(J/m²)
0.016	2	40.07	0.50	0.140	0.886
0.027	24	456.03	0.41	0.124	0.908
0.031	4	40.08	0.40	0.230	0.910
0.034	31	455.99	0.41	0.164	0.929

n number of clusters in the GB plane, A GB area, R equivalent radius of clusters, τ_{max} shear stress of unpinning, γ GB free energy

3.3.2 Grain boundary motion in a random alloy

Random distribution of Ta atoms in Cu also imposes a resistance to GB motion, but for the same alloy composition, the effect is not nearly as strong as when Ta forms clusters. For
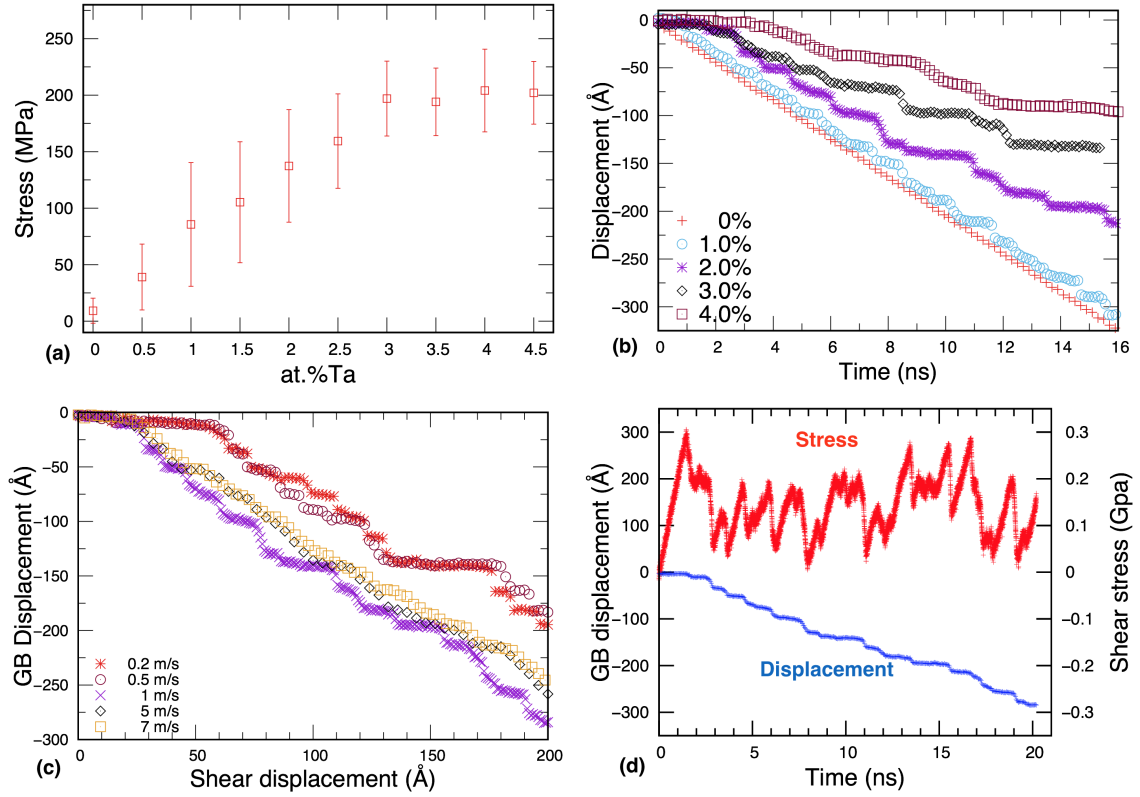
Figure 3.7: Coupled motion of the $\Sigma 17$ GB in the random Cu-Ta solid solution at 900 K. (a) Average stress for GB motion as a function of chemical composition with grain translation velocity of 1 m/s. The error bars indicate the standard deviation of the stress from the average value during the simulations. (b) GB displacement as a function of time for the alloy compositions indicated in the legend with grain translation velocity of 1 m/s. (c) GB displacement as a function of grain translation for the translation velocities indicated in the legend. The alloy composition is 2 at.%Ta. (d) GB displacement and shear stress as functions of time for the 2 at.%Ta alloy.

example, a shear stress of 230 MPa was required to unpin the GB in the sample containing 0.031 at.%Ta (Fig. 3.4a). In a random alloy with this composition, the stress of GB motion is practically indistinguishable from that in pure Cu. Nevertheless, at a fixed grain translation velocity $v_{||}$, this stress increases with Ta concentration, and in alloys, with 3 or more at.%Ta reaches a plateau at 200 MPa (Fig. 3.7). Fig. 3.7b shows that, with increasing Ta concentration, the GB moves on average slower (at a fixed translation velocity of the grains). Thus, the GB response to the applied shear gradually transitions from coupling to

sliding.

An interesting feature of GB migration in the random alloy is its stop-and-go character with alternating periods of rapid motion and arrest (Fig. 3.7). This mode of GB motion is accompanied by a saw-tooth behavior of the shear stress, with an accumulation of stress during the arrest time and a rapid drop during the motion (Fig. 3.7d). As illustrated in this figure, the stop-and-go motion becomes more pronounced with increasing Ta concentration and/or decreasing grain translation velocity (and thus the average GB velocity).

Although a quantitative theory of this interesting effect is yet to be developed, the following qualitative explanation is proposed. As was noted in the previous work [32], short-circuit diffusion of Ta atoms along GBs plays in Cu-Ta alloys. A stationary GB is capable of redistributing the Ta atoms initially located in its core region and narrow vicinity to form nanoclusters. The latter pin the boundary in place, and it remains immobile until the grain translation creates a critical level of stress required for unpinning. Once unpinned, the GB moves fast until the coupling effect reduces the stress, and the boundary stops. While the stress builds up again, the boundary remains stationary, and the GB diffusion creates a new set of clusters that pin the boundary in its new position. The GB remains pinned until the stress reaches the unpinning level again, and the process continues in a stop-and-go manner. The dynamic instability inherent in this process is somewhat similar to the dynamic strain aging phenomenon [111] and the Portevin-Le Chatalier effect [112], except that the role of dislocations and impurity atoms is played by the GB and the clusters, respectively.

The process just described must create an array of Ta clusters behind the moving GB. This was indeed observed in the simulations, as illustrated in Fig. 3.8. The proposed mechanism is consistent with the observed composition and rate dependencies of the stop-and-go motion. The larger the Ta concentration, the more atoms are available in and near the GB to build new clusters; the slower the grain translation velocity, the more time is given to GB diffusion to form larger clusters.
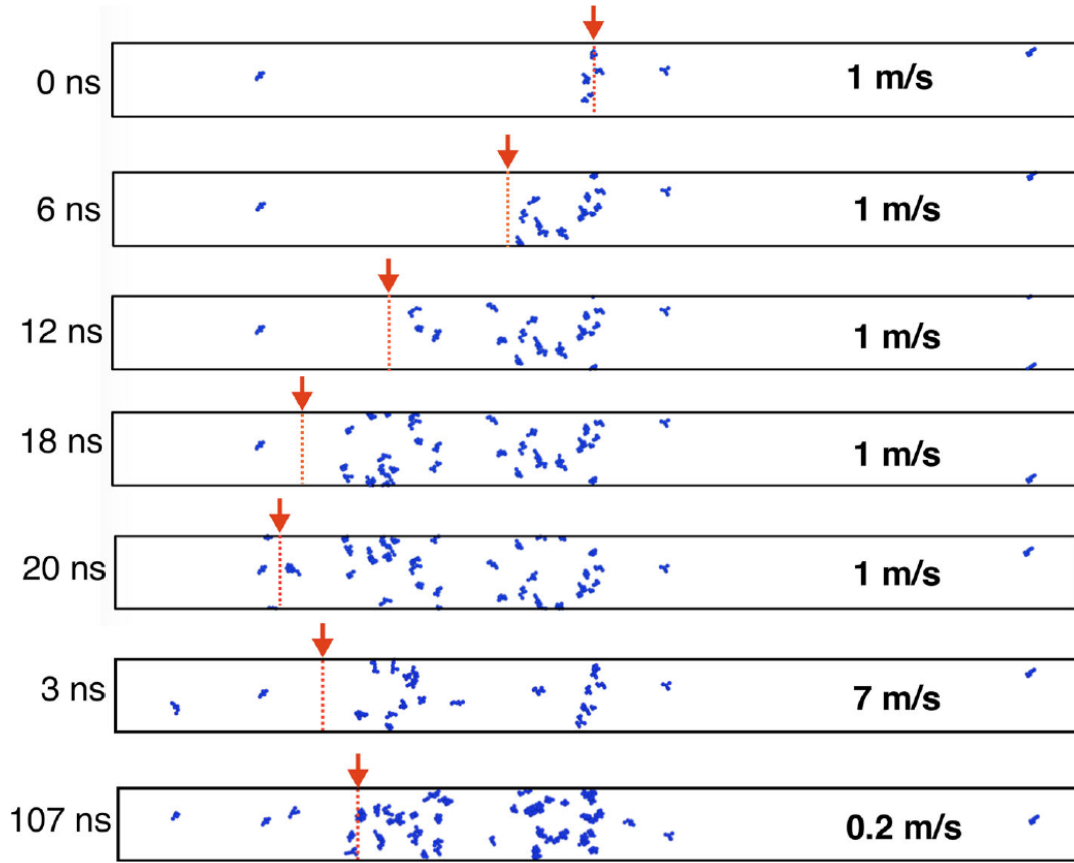
Figure 3.8: Clustering during GB motion in the random Cu-2at.%Ta alloy at 900 K. Only Ta clusters containing 5 or more atoms are shown in the images. The numbers in the left and right columns indicate the elapsed time and the velocity of grain translation, respectively. The arrow shows the GB position. Note the formation of a Ta cluster array behind the moving boundary. The slower the GB motion, the larger are the Ta clusters.

3.4   Conclusion

Stress-driven GB motion has been studied by atomistic simulations in Cu with Ta nanoclusters and in a random Cu-Ta solution. For the alloy with clusters, the simulations confirm the previously observed stability of the cluster size [29, 32–34]. Adding more Ta in the alloys only increases the number density of Ta clusters with little or no effect on their size distribution. In contrast to previous simulations conducted on polycrystalline samples [29, 32], in this project, we have focused on an individual GB. This allowed us to investigate

its interaction with Ta clusters in greater detail. The stress behavior during the GB-cluster interactions has identified two stages of the process, attraction, and pinning, which is consistent with the Zener model of pinning by spherical obstacles. To compare the simulation results with the Zener model quantitatively, we extracted the GB free energy γ from a set of simulations for different alloy compositions and systems sizes. While the number of clusters in the GB plane varied by more than an order of magnitude, the obtained values of γ were well-reproducible and had a very reasonable magnitude (Table 3.1). For the temperature of 900 K, the simulations predict the pinning stress on the level of 100-200 MPa (Table 3.1) and the sliding stress of 300-400 MPa (Fig. 3.3a). For comparison, the stress of moving the same GB with the same velocity in pure Cu is at least an order of magnitude less (<9 MPa). Although the fast (in comparison with experiment) GB motion implemented in the MD simulations is likely to overestimate all stresses, it is reasonable to expect that the relative magnitude of the stresses is represented correctly. The large pinning stress by the Ta clusters and the quantitative agreement with the Zener pinning model provide strong evidence that the high-temperature stability of the grain size demonstrated by the Cu-Ta alloys is primarily due to the pinning of GBs by Ta clusters. Structure evolution in these alloys can, therefore, be modeled by Monte Carlo [113, 114], phase field [115], finite-element [116] and other non-atomistic methods, with input data provided by atomistic simulations.

For comparison, we have studied stress-driven motion of the GB in a random Cu-Ta solid solution, mimicking the state of the material right after mechanical alloying. Although the randomly scattered Ta atoms also imposed a resistance to GB motion, the effect is not as strong as in the alloy with clusters. It was found that, due to short-circuit Ta diffusion in GBs, a moving GB precipitates a set of Ta clusters in its wake (Fig. 3.8). This observation suggests a mechanism by which the clusters can form inside the grains as observed in experiments [29, 33, 34]. At high temperatures, the clusters can precipitate directly from the solid solution by a process similar to spinodal decomposition [32]. However, Ta diffusion in the Cu lattice is very slow [29] and at relatively low temperatures, this process is ineffective. The proposed GB-assisted mechanism can operate a lower temperatures when

lattice diffusion is frozen out.

Although these results were obtained for a particular symmetrical tilt GB, it is believed that the general conclusions remain valid for all high-angle GBs. This assumption can be validated by studying a larger set of different GBs in the future.

Chapter 4: Atomistic modeling of capillary-driven grain boundary motion in Cu-Ta alloys

4.1   Introduction

Many beneficial properties of nanocrystalline materials owe their origin to the large specific area (per unit volume) of grain boundaries (GBs) and other interfaces. One such property is the high mechanical strength. The strengthening effect is partially caused by the formation of dislocation pileups stopped at GBs [54]. However, at small enough grain sizes, the dislocation sources inside the grains cease to operate, and the dislocation pileups cannot form. Instead, the plastic deformation is predominantly controlled by GB processes such as GB sliding and grain rotation [38, 69, 93, 117–123].

Wider applications of nanocrystalline alloys are hampered by the onset of grain growth at elevated temperatures. In some of the nanocrystalline materials, substantial grain growth can even occur at room temperature. The driving force for grain growth has a capillary nature and is caused by the excess free energy of GBs. Since the specific GB area in nanocrystalline materials is large, the capillary driving force is strong and increases as the grains become small. The grain growth results in deterioration of the superior properties of nano-materials.

Several approaches have been proposed for reducing the grain growth, the most effective of them being alloying. There are two possible mechanisms by which alloying can stabilize nano-grains. The thermodynamic stabilization can be achieved by reducing the GB free energy γ by solute segregation [12–15, 20, 68, 98, 124–127]. Since the capillary driving force is proportional to γ, the grain size can be preserved for a longer time and/or up to higher temperatures. It has even been suggested that the total free energy may reach a minimum at a finite grain size, producing a thermodynamically stable nano-grained material [13–

15, 68, 95, 98, 126, 128, 129]. The kinetic stabilization is achieved by the reduction in the GB mobility by the solute drag effect [17, 19, 127, 130] or by the Zener pinning of GBs by small precipitates of a second phase [19, 22–24, 113, 114, 127, 131]. Clean separation of the thermodynamic and kinetic factors is very difficult. In many cases, the grain stabilization is likely to be a combined effect of both mechanisms.

Nanocrystalline Cu-Ta alloys have recently attracted much attention due to their extraordinary structural stability and strength at high temperatures [29–35, 131]. FCC Cu and BCC Ta are practically immiscible in the solid-state. High-energy mechanical alloying produces an unstable solid solution of the two elements, which decomposes during the subsequent thermal processing. Ta atoms precipitate from the solution in the form of nanometer-scale clusters coherent with the Cu matrix. These clusters strongly pin the GBs by the Zener mechanism, preventing the grain growth. As a result, a Cu-Ta alloy can preserve the grain size of about 100 nm at high temperatures up to the melting point of Cu. The existence of this fully stabilized nano-structure opens an avenue for the design of a new class of materials for high-temperature, high-strength applications.

The grain size stabilization leads to unique mechanical properties of Cu-Ta alloys, such as the high strength (above 1 GPa) and small strain-rate sensitivity under tension and compression [31], lack of superplastic behavior, and excellent creep resistance [39]. The Ta clusters located inside the grains contribute to the strengthening by restraining the dislocations glide and twinning. The clusters residing at GBs block the dislocation transmission and enhance the Hall-Petch mechanism of hardening [54]. In addition, the GB clusters create obstacles to the operation of GB deformation mechanisms by suppressing the GB sliding and grain rotation.

Cu-Ta alloys also present an ideal model system for understanding the general principles of grain stabilization. The Ta atoms do not follow the classical segregation model wherein the solute atoms form a relatively uniform distribution over the GB area and reduce the GB free energy. Instead, the Ta atoms form a chain of discrete nanoclusters attached to the GBs and separated by large areas of pure Cu boundaries, as illustrated in Fig. 4.1
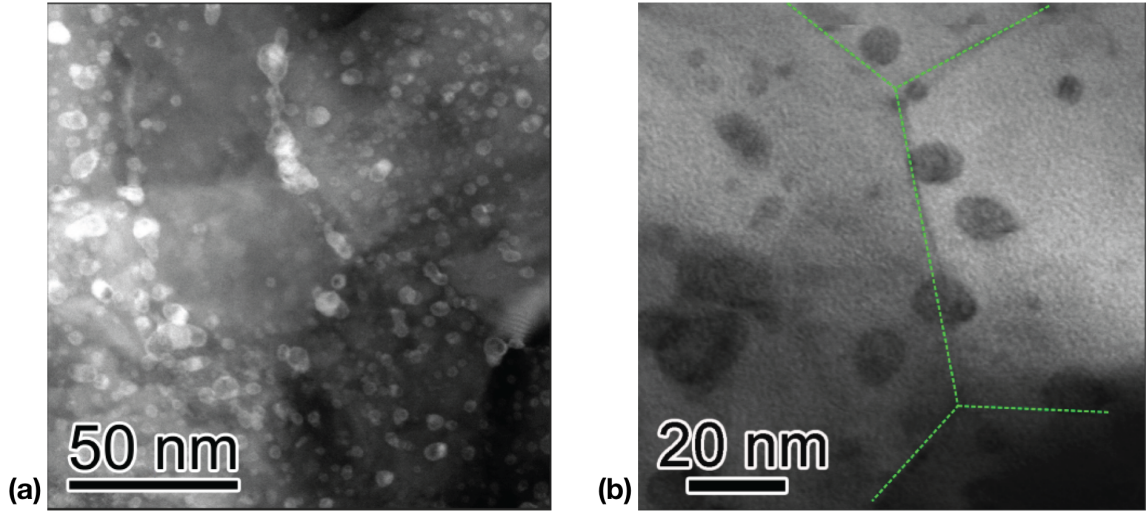
Figure 4.1: High resolution high-angle annular dar-field (HADDF) scanning transmission electron microscopy (STEM) image of a Cu-3at.%Ta alloy consolidated by equal channel angular extrusion (ECAE) at 700^0C. The Ta clusters are revealed by Z-constrast. The average Cu grain size is about 86 nm. a) A typical grain decorated with Ta clusters. b) Zoom-in view showing Ta clusters residing at and near GBs. The approximate GB positions are outlined by dashed lines.

for the Cu-3at.%Ta alloy. The upper left corner of the image in Fig. 4.1a shows a grain decorated with Ta clusters, with a more detailed view of the clusters shown in Fig. 4.1b. Since the clusters only occupy a small fraction of the total GB area, they are unlikely to reduce the GB free energy substantially, as assumed in the thermodynamic stabilization models. On the other hand, they can be very effective in blocking the GB motion by the Zener pinning mechanism [22–24, 113, 114]. This presents us with an opportunity to gain a better mechanistic understanding and evaluate the strength of the kinetic stabilization mechanism separately from the thermodynamic factor.

The previous atomistic simulations [131] have confirmed that Ta clusters in Cu-Ta alloys can exert a strong pinning force and can totally arrest the GB motion. The stress behavior during the GB-cluster interactions was found to be consistent with the Zener model [22–24, 113, 114]. The GB migration was driven by applied shear stress causing the GB motion by the shear-coupling effect [37, 92]. It was noted that the applied stresses driving the GB

37

motion were rather large, and the speeds of GB migration were orders of magnitude higher than the typical speeds under experimental conditions.

The main goal of the present work was to demonstrate that the conclusions reached in the previous study [131] are independent of the particular driving forces or GB migration rates implemented there. To this end, we have performed systematic atomistic simulations of GB motion driven solely by the capillary pressure. The grain sizes studied here are typical of many nanocrystalline materials. Accordingly, the capillary driving force applied to the GBs is representative of typical forces existing in real materials. In addition to the modeling of GB-cluster interactions, we investigate the role of GBs in the precipitation of Ta clusters during the decomposition of the unstable Cu-Ta solution. This precipitation leads to dynamic instability of the GB motion and eventually the GB arrest when the growing clusters reach a critical size.

4.2 Methodology

Atomic interactions were described by the recently constructed angular-dependent interatomic potential for the Cu-Ta system [32]. A rectangular simulation block was initially filled with perfect FCC Cu lattice and had the dimensions $31.8 \times 31.8 \times 7.3$ nm (599,760 atoms) with periodic boundary conditions. A cylindrical grain with a radius of 9.99 nm was created at the center of the block by rotating its lattice around the [001] z-direction by an angle θ_0 (Fig. 4.2). The atomic structure of the tilt GB was equilibrated by minimizing its energy with respect to removal, addition, and displacements of atoms as described elsewhere [93].

In addition to the pure Cu system, Cu-Ta alloys were created with three different distributions of Ta atoms. In the first case, Ta was introduced into the GB region by composition-controlled semi-grand canonical Monte Carlo (MC) simulations using the parallel MC code ParaGrandMC [132]. The temperature of the simulations was chosen to be 900 K. The
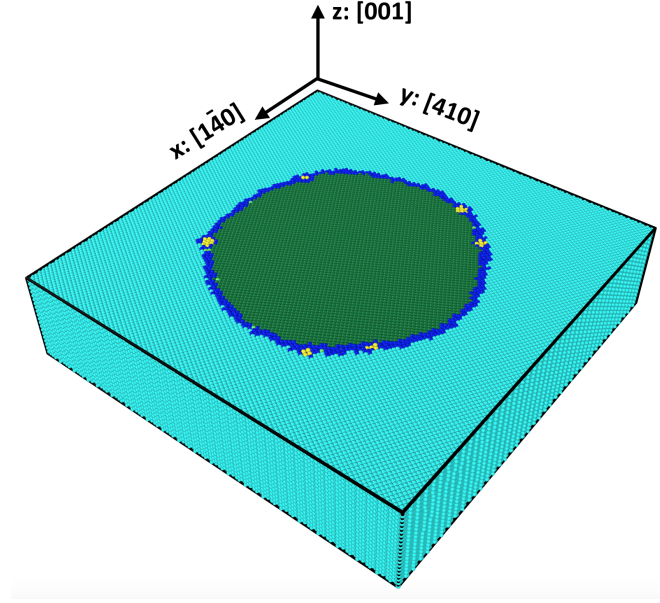
Figure 4.2: Simulation block containing a cylindrical grain. The Cu atoms in the exterior and the interior grains are shown in cyan and green color, respectively. The GB (blue) is decorated with a set of Ta clusters (yellow).

trial moves of the MC algorithm included small random displacements of randomly selected atoms in a random direction with the simultaneous random reassignment of chemical species to either Ta or Cu. In addition, the system dimensions were randomly rescaled. This rescaling ensured zero-stress conditions during the simulation, which helped to minimize the effect of the large atomic size difference between Cu and Ta. The trial moves were accepted or rejected by the Metropolis criterion [133]. Due to the negligible mutual solid solubility in the Cu-Ta system, Ta nanoclusters only formed in the GB region. In the composition-controlled mode of the MC algorithm [91, 108, 132], there is a feedback loop between the composition and the chemical potential difference between the species that ensure equilibration to the given chemical composition of the system. This allowed us to create a set of alloys with several targeted chemical compositions. In the following, these compositions will be measured by the atomic percentage of Ta atoms averaged over the entire simulation block. Given that the Ta atoms are actually located in the GB region, such compositions do not represent the GB chemistry and only serve to label its different

chemical states.

In the second case, the chemical species were only switched during the MC simulations within a 3 nm thick concentric cylindrical shell with a radius smaller than the radius of the grain. The obtained Ta-rich shell mimicked a Ta distribution left behind by an imaginary smaller grain that had detached from this distribution and disappeared. This configuration was created to study the GB interaction with this Ta distribution as the grain shrinks by capillary forces. As in the previous case, several alloy compositions were created.

Finally, in the third case several nonequilibrium solid solutions were created by randomly substituting Cu atoms by Ta atoms uniformly across the entire simulation block until a prescribed chemical composition was reached. Such random solutions represented the state of the material after the mechanical alloying and prior to the thermal treatment.

Starting from the initial configuration, the system evolution was studied by molecular dynamics (MD) simulations. The Large-scale Atomic/Molecular Massively Parallel Simulator (LAMMPS) [107] was utilized. The isothermo-isobaric (NPT) ensemble was implemented at the temperatures of 750 to 1100 K under zero pressure conditions. The latter condition ensured that no internal stresses were developed in the simulation block due to the volume change caused by the GB motion. Snapshots of the simulation were saved at regular time intervals recording the coordinates, velocities, energy, and stress components of an individual atom. The GB position was tracked using the bond angle analysis implemented in the OVITO visualization software [110]. The effective radius of the grain was calculated by averaging the distance to the GB atoms from their centroid. Changes in the lattice orientation in the grain were tracked using four nearest neighbors lying in the (x, y) plane for the lattice atoms inside and outside the grain (0.8 nm away from the GB). The minimum rotation angle between the sets of four vectors pointing to the neighbors was averaged over the inner atoms of the grain and taken as the misorientation angle θ across the GB.

4.3 Results

4.3.1 Grain shrinkage and rotation in pure Cu

To provide a baseline for comparison with Cu-Ta alloys, simulations were first conducted on the pure Cu system. As expected, the grain was found to shrink and eventually disappear. Simultaneously, the lattice of the grain was found to rotate towards larger misorientation angles. Fig. 4.3 shows the results for the initial misorientation angle $\theta_0 = 28.07^0$. In this figure and all similar plots, the data points were collected from individual snapshots. The GB area decreases as a linear function of time following the parabolic kinetics predicted by theoretical models [92, 93]. Slight deviations from the parabolic kinetics are observed when the grain becomes small (Fig. 4.3a). This acceleration of shrinkage could be due to an increase in the curvature-dependent GB free energy. The rate of GB shrinkage increases with temperature.
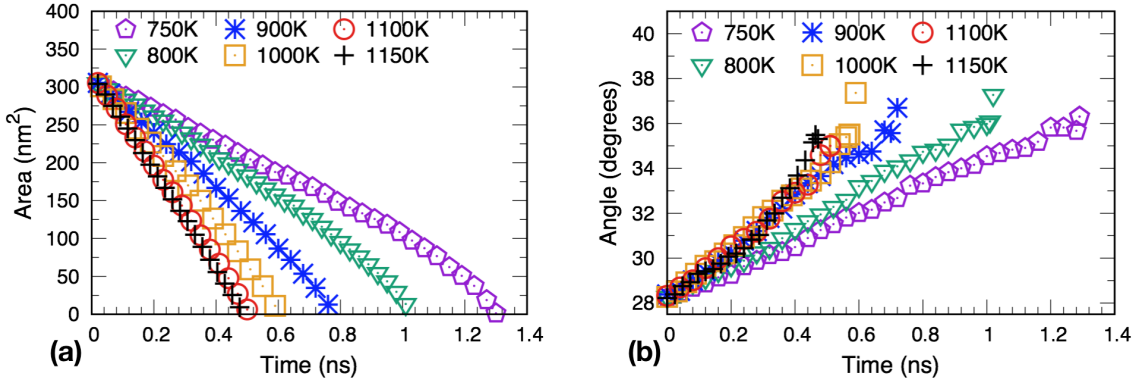
Figure 4.3: The grain area (a) and the misorientation angle θ (b) as a function of time in MD simulations of pure Cu at several temperatures. The initial misorientation angle is θ_0=28.07^0.

The grain rotation in Fig. 4.3b is expected from the shear-coupling theory [37, 92, 109, 134]. The theory predicts that coupled motion of a curved GB creates a driving force for relative rotation of the two grains. For tilt GBs, this rotation should occur towards larger

misorientation angles. This predicted mode of rotation was indeed observed in previous MD simulations [93, 135] and is confirmed in this work. At all temperatures studied here, the GB remains shear coupled and rotates towards the angle of about 36^0. This special angle is associated with the discontinuity in the misorientation dependence of the coupling factor [37,93,94,109,134]. These results are in full agreement with the previous work, which lends additional confidence to the simulation methodology employed in this project.

4.3.2 GB pinning by Ta clusters

When Ta was introduced into the GB region and the latter was equilibrated by MC simulations, Ta was found to form a distribution of discrete clusters with an approximate size of about a nanometer (20-25 atoms) decorating the GB (Fig. 4.2). An increase in the alloy composition only produced more clusters with little effect on their size or size distribution. The tendency of Ta atoms to preserve the cluster size was also observed in the previous simulations [29,30,32–35,131] and experiments [30,31,33–35,131]. In this work, the cluster size was measured by its effective radius $r = (3n\Omega/4\pi)^{1/3}$, where Ω is the atomic volume of the alloy, and n is the number of atoms in the cluster. The average cluster radii are

Figure 4.4: The grain area (a) and the misorientation angle θ (b) as a function of time in MD simulations of the grain pinned by Ta clusters at 900 K. The alloy compositions (at.%Ta) are indicated in the legend.

summarized in Table 4.1 as a function of alloy composition. As Ta concentration increases, r only changes from 0.39 nm to 0.44 nm, whereas the number N of Ta clusters increases in proportion to the concentration and reaches N = 33 at the highest concentration studied here (0.15at.%Ta).

When the number of clusters was small, the capillary force easily unpins the GB from the clusters. The grain then shrinks and rotates toward the 36^0 misorientation, as it does in pure Cu but at a slower rate (Fig. 4.4). The initially small slope of the curves in Fig. 4.4 reflects the unpinning process. Once the GB is unpinned, its further evolution follows the parabolic kinetics as in pure Cu.

The unpinning does not occur uniformly along the GB but rather follows the "unzipping" mechanism illustrated in Fig. 4.5. The GB initially unpins from one random cluster, and the free GB segment tries to migrate toward the grain center, exerting pulling forces on the neighboring clusters. These neighbors eventually also let the GB go, and the free segments become longer. This unzipping process continues to propagate along the GB, unpinning one cluster at a time, until the entire GB detaches from the set of clusters and continues to shrink and rotate in the pure Cu region. While the grain area continues to decrease during the unpinning process, the grain rotation remains blocked until the complete separation from the clusters. This explains the nearly horizontal portions of the curves in Fig. 4.4b.

As the Ta concentration increased, the pinning effect of the clusters became stronger. The GB took a longer time to unpin, and the grain rotation became shorter (Fig. 4.4). In the 1.5at.%Ta alloy containing 33 GB clusters, the GB was unable to unpin on the timescale of the present simulations.

It is interesting to compare the simulation results with predictions of the Zener model of GB pinning [22–24, 113, 114]. According to this model, the GB motion is blocked when the driving pressure due to the GB curvature is balanced by the pinning pressure exerted on the GB by disperse particles. The maximum pinning force created by a single spherical particle is $F_{max} = \pi r \gamma$, where r is the particle radius and γ is the GB free energy. For N particles interacting with a GB of area A, the maximum pinning pressure is $P_p = \pi r \gamma N / A$.
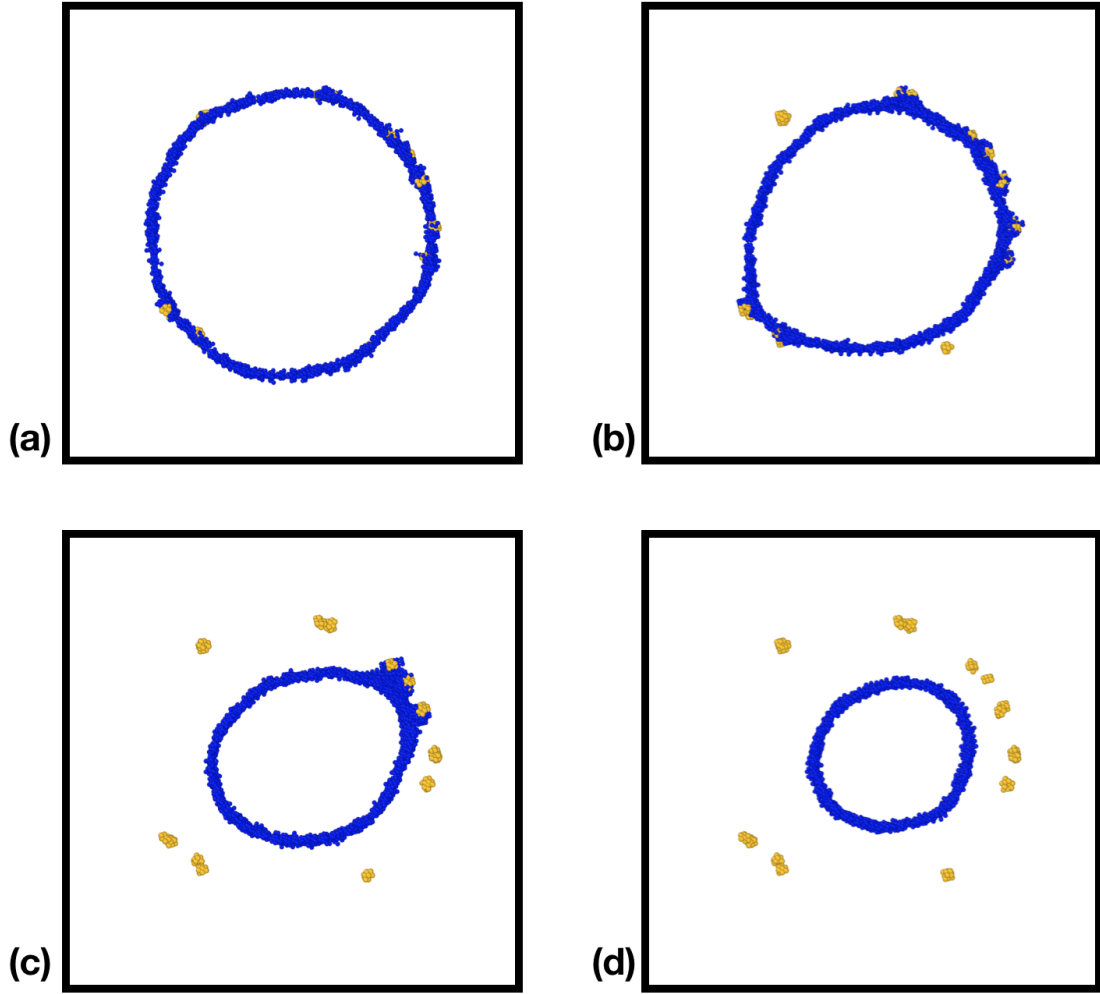
Figure 4.5: The unpinning mechanism in the Cu-0.05at.%Ta alloy at 900 K. (a) Ta clusters (yellow) are initially located at the GB (blue). (b) The GB has unpinned from 2 clusters, and the unpinning process propagates along the GB. (c) The GB has unpinned from most of the clusters. (d) The GB has totally unpinned from the clusters. FCC Cu atoms are not shown for clarity.

In the present case A = 2πRL, where R is the radius of the cylindrical grain and L is its thickness in the z-direction. Using the capillary pressure $P_c = \gamma/R$, the pinning condition $P_p = P_c$ gives

$$N = \frac{2L}{R} \tag{4.1}$$

Inserting L = 7.3 nm and r = 0.44 nm (Table 4.1), the grain should be pinned in its initial state by N ≈ 33 clusters. This number exactly matches the number of clusters blocking the grain in the 0.15at.%Ta alloy.

Table 4.1: Characteristics of cylindrical GB clusters as a function of alloy composition at 900 K.

Alloy composition(at.%Ta)	N	r(nm)	GB area per cluster (nm^2)
0.05	15	0.39	30.76
0.06	16	0.41	28.84
0.07	19	0.41	24.28
0.08	24	0.39	19.22
0.09	25	0.40	18.46
0.10	28	0.40	16.47
0.15	33	0.44	13.98

This perfect agreement may seem surprising since the Zener model is based on many assumptions and approximations [24]. For example, the equation for F_{max} that we utilized above assumes that the particle-matrix interface is incoherent. More generally, $F_{max}=\alpha r\gamma$ and Eq. 4.1 becomes N=$2\pi L/\alpha r$, where α is a numerical factor. For incoherent particles $\alpha=\pi$, while for coherent $\alpha=2\pi$ [136]. On the other hand, keeping the particles incoherent but taking into account the GB curvature, $\alpha\approx3.96$ [137]. Given the approximate character of the model and the fact that the boundary was only pinned on the relatively short timescale of the MD simulations, this perfect agreement is likely to be fortuitous. Nevertheless, it does indicate that the GB pinning observed in the present simulations is generally consistent with the Zener mechanisms.

Fig. 4.6 shows the results of similar simulations at four different temperatures (800 K, 900 K, 1000 K, and 1100 K) at a fix alloy composition (0.08 at.%Ta). As expected, the rates of GB migration and grain rotation increase with temperature.

In addition, the unpinning time manifested by the horizontal portions of the curves becomes shorter at higher temperatures. These changes reflect the thermally activated
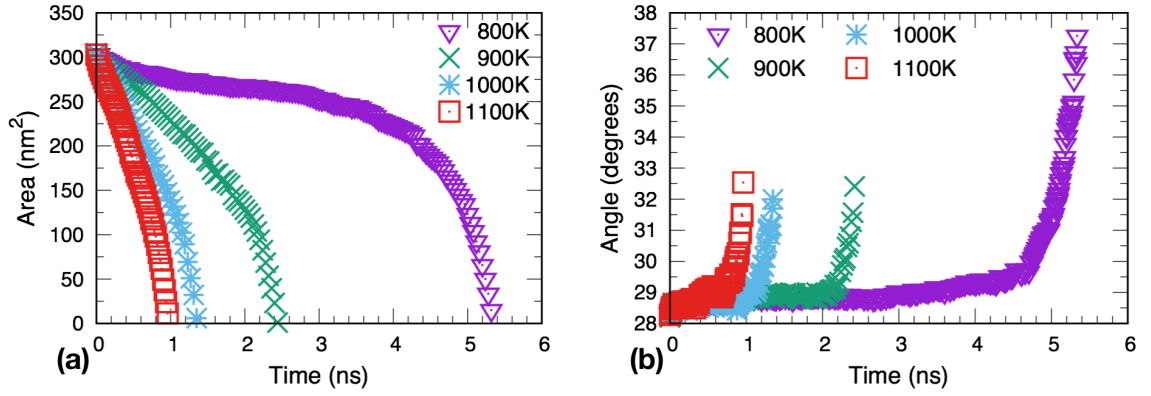
Figure 4.6: The grain area (a) and the misorientation angle θ (b) as a function of time in MD simulations of the grain pinned by Ta clusters in the Cu-0.08at.%Ta alloy at different temperatures.
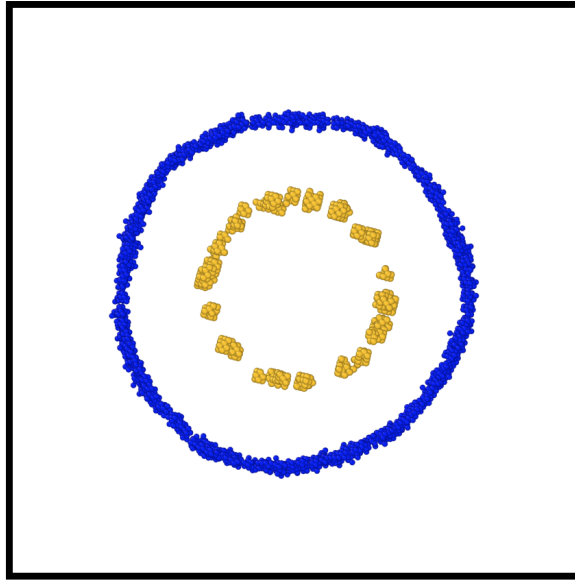
Figure 4.7: Typical initial configuration of Ta clusters forming a cylindrical shell inside the grain. The grain shrinks and rotates until the GB (blue) hits the clusters (yellow).

nature of the unpinning process and of the coupled GB migration/rotation process.

In the preceding simulations, the Ta clusters were created at the GB from the very beginning. To demonstrate that our conclusions do not depend on the initial conditions, a similar distribution of clusters was created in a cylindrical shell inside the grain (Fig. 4.7).

As mentioned above, one can think of such clusters as left behind by another GB that was pinned by them but was able to escape and migrated elsewhere. In this simulation setup, the GB was expected to start moving in the pure Cu region and eventually hit the cluster distribution. This was indeed observed in the simulations. The grain rotated from the initial $\theta_0=28.07^0$ misorientation to about 33^0 before encountering the clusters.

When the alloy concentration, and thus the number of clusters, were small, the boundary was able to unpin from the clusters and continued to shrink until the grain collapsed into a point. The GB-cluster interaction only caused a temporary hold of the shrinkage process, manifested in the horizontal portions of the area-time and angle-time curves (Fig. 4.8). The unpinning occurred by the previously discussed unzip mechanism.
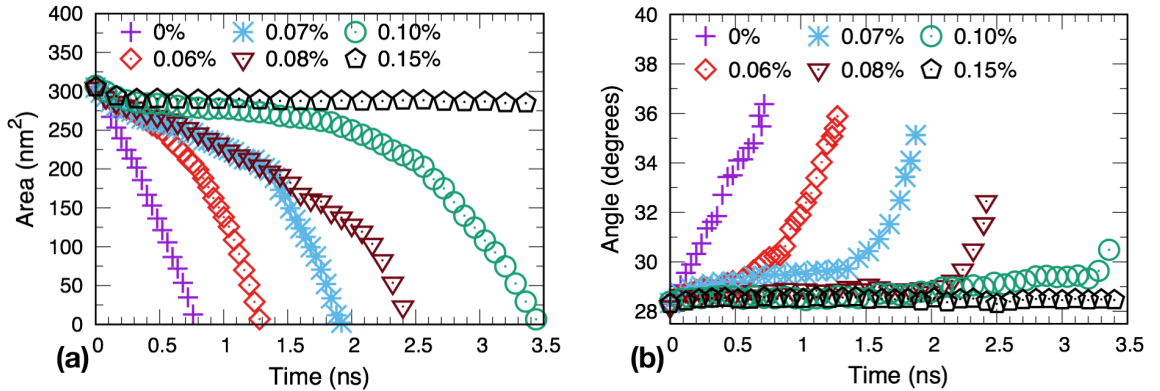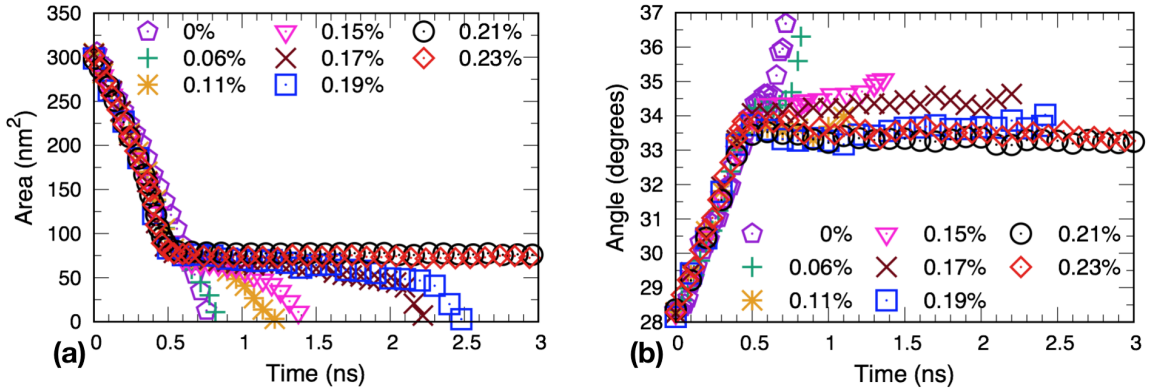

Figure 4.8: The grain area (a) and the misorientation angle θ (b) as a function of time during MD simulations of the grain containing a set of Ta clusters at 900 K. The alloy compositions (at.%Ta) are indicated in the legend. The initial misorientation angle is $\theta_0=28.07^0$.

At higher Ta concentrations, the GB took a longer time to unpin and eventually was stopped by the clusters when the alloy composition reached 0.21 at.%Ta. The previous calculations from equation 4.1 predicted that 33 clusters should be sufficient to block the GB migration. However, as indicated in Table 4.2, the actual number of GB clusters in the 0.21 at.%Ta alloy is 43. In addition to the approximate character of the Zener model mentioned above, the discrepancy could be caused by the significantly larger surface density of the

clusters in the cylindrical shell in comparison with the initial GB (cf. Table 4.1). Under the high- density conditions, the clusters can no longer be treated as isolated as assumed in the Zener model. The contact angles between the clusters and the short GB segments connecting them could no longer reach 45^0 corresponding to the maximum pulling force. This could reduce the increase in the pinning efficiency per each added cluster. Another potential source of discrepancy is the elastic strain field around the clusters [138], which is not in the Zener model. Considering these uncertainties, the simulation results can be considered compatible with the Zener model, at least on a semi-quantitative level.

Table 4.2: Characteristics of Ta clusters in the cylindrical shell inside the grain as a function of alloy composition at 900 K.

Alloy composition(at.%Ta)	N	r(nm)	GB area per cluster (nm^2)
0.06	17	0.39	13.07
0.08	24	0.38	8.71
0.11	30	0.41	7.11
0.15	45	0.39	4.84
0.17	44	0.41	4.97
0.19	46	0.42	4.66
0.21	43	0.44	5.40
0.23	45	0.44	4.88

4.3.3   GB motion and grain rotation in random solid solution

Randomly distributed Ta atoms inserted in the Cu matrix imposed a drag force that reduced the rates of GB migration and grain rotation in comparison with pure Cu. This drag effect was not as strong as the pinning effect of the clusters. Much higher Ta concentrations were required to achieve the same level of retardation. The effects of the alloy composition and temperature are illustrated in Figs. 4.9 and 4.10, respectively. It is evident that the addition of Ta significantly reduces the rate of GB migration and strongly suppresses the grain rotation.
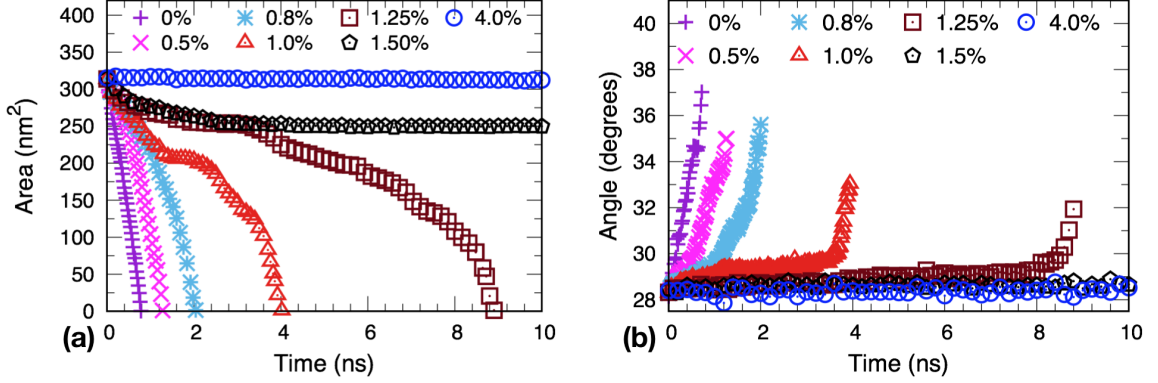
Figure 4.9: The grain area (a) and the misorientation angle θ (b) as a function of time in MD simulations of random Cu-Ta solution at 900 K. The alloy compositions (at.%Ta) are indicated in the legend.
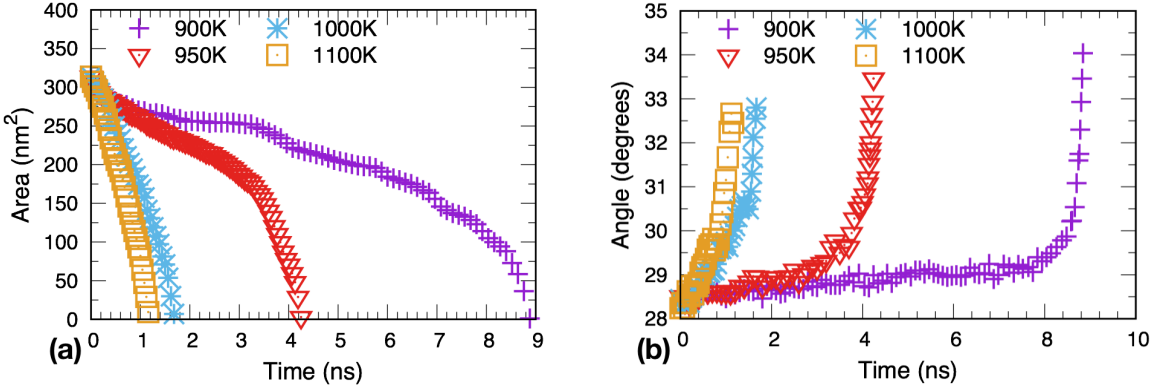
Figure 4.10: The grain area (a) and the misorientation angle θ (b) as a function of time in MD simulations of random Cu-1.25at.%Ta alloy at different temperatures. The temperatures are indicated in the legend.

The capillary driving force γ/R increases as the grain shrinks, which explains the accelerated shrinkage rate at the end of the simulation when the grain becomes small. At this final stage, the grain rotation is accelerated as well.

An interesting feature of this process is its stop-and-go character manifested in the stepwise shape of the area-time curves (Figs. 4.9 and 4.10). This stop-and-go behavior is especially pronounced at higher Ta concentrations and/or lower temperatures. A similar effect was observed in the recent simulations of stress-driven GB motion in the random

Cu-Ta solution [131]. The mechanism of this effect is related to the formation of small GB clusters by short-circuit diffusion of Ta atoms along the GB. Such clusters pin the GB and it stops for a period of time during which the cluster formation continues to occur. The boundary eventually beaks away from the clusters, makes a fast move forward, but soon slows down due to the drag force. This allows the short-circuit diffusion to start the formation of a new set of clusters. These clusters eventually stop the boundary and the whole process repeats. As a result, the GB evolution consists of alternating periods of rapid motion and arrest. The dynamic instability of this process makes it similar to the dynamic strain aging phenomenon [111], the Portevin-Le Chatelier effect [112], and other cases of stick-slip behavior.

The process just described must create an array of Ta clusters behind the moving GB. This was indeed observed in the simulations, as illustrated by two examples in Fig. 4.11. In the 1.25 at.%Ta solution at 900 K, the boundary shrinks in the stop-and-go regime and collapses into a point after 8.8 ns. Fig. 4.11a shows the clusters formed during this time.
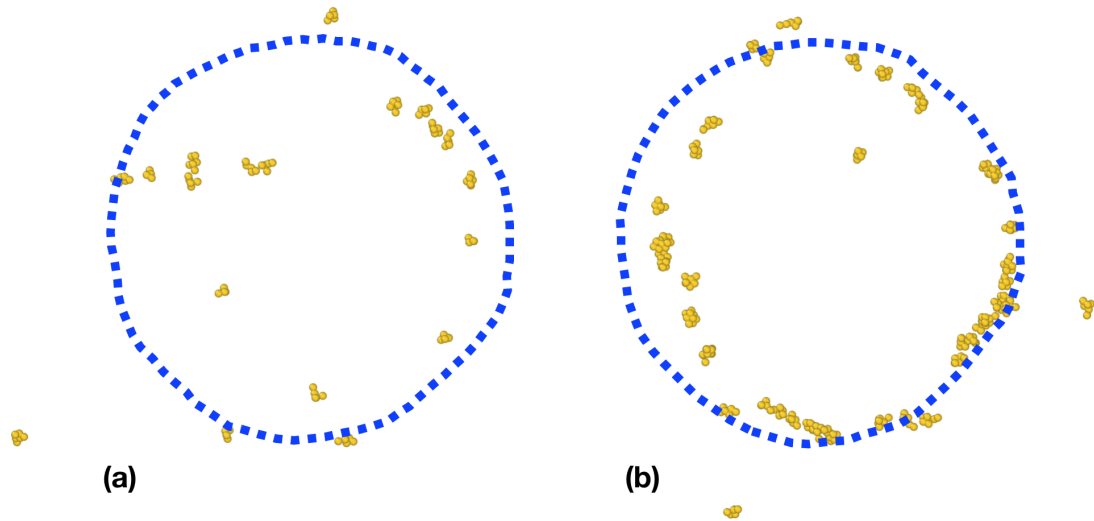
Figure 4.11: Ta clusters precipitation from the Cu-Ta random solution in MD simulations at 900 K. The dashed circle shows the initial GB position. (a) 1.25 at.%Ta solution after the GB shrinks to a point. Only clusters containing more than four atoms are shown. (b) 1.5 at.%Ta solution where the GB stopped after a short period of migration. Only Clusters containing more than five atoms are shown.

50

While two clusters precipitate outside the grain, most of them form in the area swept by the GB motion. The chain of clusters in the upper right corner of this area was created by a GB segment that remained pinned at this location for a longer period of time than other segments. In the solution containing 1.5 at.%Ta at the same temperature, the GB quickly shrinks by about a nanometer, after which it shops and becomes permanently pinned by the clusters. For the rest of the simulation run (90 ns), the boundary only serves as a short-circuit path for further cluster growth, leading to the formation of many new clusters (Fig. 4.11b).

While the increase in the rate of cluster formation (and thus the stop-and-go GB motion) with Ta concentration is readily understood, the effect of temperature is less predictable. Higher temperature increases the rate of GB diffusion needed for the cluster formation. At the same time, the GB moves faster and unpins from the clusters more easily, leaving the GB less time to grow the clusters in size. The present simulations indicate that the second trend dominates over the first: low temperatures favor the cluster formation due to the slow GB motion, even though the Ta diffusivity inside the GB is slower.

4.4 Conclusion

In the previous work [131], the GBs were driven by applied stresses coupled to the GB motion. By contrast, the present study was focused on the motion of curved GBs driven by capillary forces. The latter process is more relevant to the structural stability problem since the grain growth in polycrystalline materials is caused by capillary forces.

In conventional, coarse-grained polycrystalline materials, the capillary driving force (pressure) is on the order of 10^3 to 10^5 Pa [139]. In nanocrystalline materials, this force is much larger. Assuming $\gamma = 1$ J/m^2 and taking the initial grain radius R $\approx$ 10 nm studied here, the estimated capillary pressure is about $\gamma/R \approx 100$ MPa. Nanocrystalline materials with grain diameters of about 20 nm are not unusual; thus the pressures implemented in this work are quite realistic. In typical Cu-Ta alloys, the grain diameter is around 100 nm,

and thus the capillary pressure $2\gamma/R$ is about 40 MPa. Under such conditions, the pinning effect of the Ta clusters is even more prominent than observed in this paper. For example, the existence of just one Ta cluster per every 3.5×3.5 nm^2 of the GB area can be sufficient for blocking the grain growth at 900 K (Table 4.1).

The GB pinning effect observed in this work is well-consistent with the Zener model [19, 22–24, 114, 127, 131]. The present simulations strongly suggest that the outstanding structural stability of the Cu-Ta alloys is solely due to the kinetic mechanism. Although the material is thermodynamically unstable, the extremely low GB mobility prevents the grain growth at any temperature up to the melting point.

A unique feature of the Cu-Ta alloys in comparison with many traditional dispersion strengthened materials is that the Ta clusters show very little, if any, coarsening at high temperatures. As noted previously [29, 30, 32–35, 131] and confirmed in this project, the Ta cluster size is extremely stable. Adding more Ta to the alloy only results in the formation of more clusters with nearly the same size. The physical origin of this remarkable property of Ta atoms in Cu is not well understood. Simulations show that Ta and Cu form a thermodynamically stable nano-colloidal structure in the liquid state [140], with the Ta cluster size comparable to that in the solid-state. This tendency to preserve the cluster size is thought to be related to the unique structure and energetics of Cu-Ta interfaces. It was suggested [140] that the Cu-Ta interactions across the interfaces favor a spontaneous interface curvature, which dictates the most stable particle size. It was also suggested that the resistance to coarsening or coalescence is an indicator of a negative interface tension that nevertheless keeps the structure stable due to the strong curvature effect [140]. More research is needed to better understand this unusual effect on the atomic level and explore its existence in other immiscible systems.

The simulations have shown that the precipitation of Ta clusters from the unstable solid solution occurs by heterogeneous nucleation at GBs. For stationary boundaries, the process involves Ta diffusion to the boundary from nearby lattice regions followed by their fast redistribution by short-circuit diffusion. As a result, the boundaries become permanently

pinned in place by the clusters. Moving GBs cannot nucleate so easily. At the early stages, they only experience a solute drag force. The latter slows them down until small clusters begin to nucleate. This creates a snowball effect in which the clusters reduce the GB speed and permit the formation of more clusters. Some of the GBs become permanently pinned, while others break away from the clusters and continue to migrate, only to be slowed down and pinned again.

In addition to the formation of GB clusters, the process described creates sets of clusters inside the grains. Such clusters continue to grow until they reach the optimal size. Some of them eventually stop the motion of other boundaries and become GB clusters, while others still remain inside the grains. The existence of Ta clusters inside the grains is well documented in the experiments [30, 31, 33–35] and is one of the contributors to the high strength and unprecedented creep resistance [39] of the Cu-Ta alloys.

Some of the clusters located inside the grains can pin lattice dislocations. In fact, dislocations could also serve as cluster nucleation sites in addition to GBs, but this hypothesis requires confirmation by experiment and/or simulations in the future.

Chapter 5: Atomistic study of Ta cluster phases and their microstructural evolution in Cu-Ta alloys

5.1 Introduction

Nanocrystalline materials exhibit superior mechanical properties compared to coarse-grained materials [1–3]. Hall-Petch relation [54] describes an increase in yield strength with a reduction in grain size as small as 10 nm beyond which there arises inverse Hall-Petch behavior [2]. However, their applications at higher temperatures are limited because of their lack of thermal stability and coarsening process even at lower temperatures. A large density of grain boundaries (GBs) increases with a continual reduction in grain size and thus posses a large driving force for grain growth upon thermal activation or deformation. Grain stabilization method involves the addition of impurities in pure nanometal, which stabilizes material through a reduction in the GB energy and/or reduction in the GB mobility. The first approach is thermodynamic stabilization, where impurities segregate to GBs, reducing GB energy that results in the reduction of a driving force for grain growth [12–15, 20, 68, 98, 124–127]. The second approach is kinetic stabilization, where the GB mobility is reduced by solute drag effect [17, 19, 127, 130] or Zener pinning by small precipitates of the second phase [19, 22–24, 113, 114, 127]. Among these methods, Zener pinning of GBs by precipitated Ta clusters have been successfully employed to explain the structural stability of immiscible Cu-Ta alloys [32, 131, 141].

Cu-Ta alloys are typical immiscible alloys without the formation of intermetallic compounds in the binary Cu-Ta equilibrium phase diagrams [43]. However, Cu-Ta alloys could be generated through experimental procedures such as mechanical alloying, magnetron sputtering, or ion beam assisted methods where Ta atoms precipitate forming a high density of

nanoscale coherent clusters [31, 33–35, 39]. The presence of these clusters along the GBs, triple junctions, or within grain gives unique thermal stability [29–32, 131, 141] and strength approximately two times higher than that predicted by Hall-Petch hardening [39]. In comparison, nanocrystalline materials have been reported to exhibit significant grain coarsening even at room or moderately low temperatures.

Previous atomistic simulations have confirmed and demonstrated that nanometer-scale Ta clusters reduce GB migration and eventually pin GBs by the Zener pinning mechanism [131, 141]. Experimental observations have revealed the presence of Ta clusters with varying sizes ranging from atomic clusters to much larger nanometer-scale Ta precipitates and phases coherent (FCC) or incoherent (BCC) to Cu crystal lattice [35, 39]. These clusters were observed to emit enormous dislocation activities in the Cu matrix. As the high strength and stability at elevated temperatures are influenced not only by the retention of the grain size but also by the accumulation of dislocations within the grain interior, this project is focussed on understanding Ta phases as a function of cluster size. In addition, the study explores the stability of Ta phases, local structural changes at the interface between the Ta clusters and the Cu matrix, and microstructural evolution under intense heating and annealing.

5.2   Methodology

Interatomic interactions in the Cu-Ta systems were described by a semi-empirical angular-dependent atomistic potential developed by Purja-Pun et al. [32]. This potential was parameterized using an extensive database of energies and configurations from density functional theory (DFT) calculations of energy differences between various crystal structures of pure Cu and pure Ta, the formation energies of coherent Cu-Ta interfaces, and the binding energy of several ordered compounds, such as $L1_2$-Cu_3Ta, $L1_0$-CuTa, $L1_1$-CuTa, B_2-CuTa, and $L1_2$-Ta_3Cu [32]. More details on the validation of the potential at different temperatures can be found in [32]. This potential was recently applied to study the structural stability of

Cu-Ta alloys and the Zener pinning of Cu grain boundaries by nano-scale Ta clusters [141]. The simulations were performed using the large-scale atomic/molecular massively parallel simulator (LAMMPS) [107].

Spherical Ta clusters were created inside cubic simulation blocks of pure FCC Cu with several different sizes up to 40 nm × 40 nm × 40 nm with periodic boundary conditions. The clusters were created by replacing Cu atoms by Ta atoms within a spherical region at the center of the block. Five different cluster radii ranging from 1.5 to 3.5 nm were studied in this work. In this simulation scheme, the Ta atoms were initially arranged in the FCC structure perfectly coherent with the surrounding Cu. The structure was then relaxed by molecular statics (total energy minimization), which resulted in a partial loss of coherency and transformation of certain regions inside the cluster from FCC to BCC. The cluster structure was examined using the visualization tool OVITO [110]. Besides FCC and BCC, a small fraction of other structures or unstructured regions were usually found in the cluster, especially near the Cu-Ta interface. The system was then slowly heated up to the temperature of 927 ^{0}C (1200 K) by molecular dynamics simulations, and the structure evolution was monitored by periodically quenching the simulation block to -273 ^{0}C (0 K) and examining its structure with OVITO. The goal was to evaluate the lattice misfit and coherency as functions of the cluster size and temperature.

5.3 Results

In the atomistic simulations, it was found that small Ta clusters remained mostly (although not fully) coherent with the Cu matrix. Since the clusters were initially created and statically relaxed at T = 0 K when the lattice misfit was large, they were never perfectly coherent. Due to the partial loss of coherency, part of the initial FCC structure of the cluster always transformed into BCC and other structural forms, as shown in Fig. 5.1. At 0 K, only about 30% of the cluster atoms form the FCC structure (Fig. 5.2). As the temperature increased, the phase composition of the clusters varied. In small clusters (e.g., with a radius

56
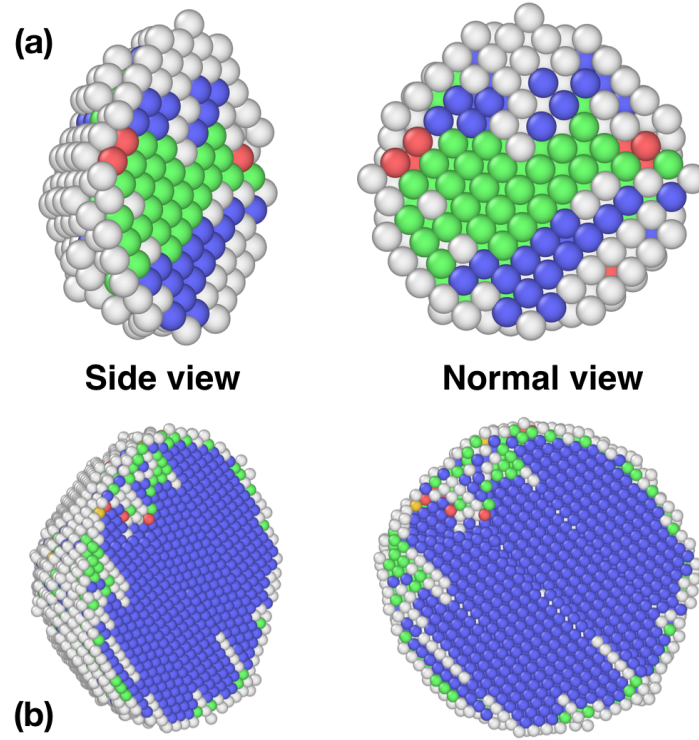
Figure 5.1: Cross sections of Ta clusters with a radius of (a) 1.5 nm and (b) 3.5 nm at 700 K. Ta atoms in FCC and BCC environments are shown in green and blue. The white atoms represent other structural environments at the interface.

of 1.5 nm), the fraction of the FCC structure was found to increase with temperature while the fraction of the BCC structure decreased. Thus, the clusters became more coherent at higher temperatures, suggesting that the lattice misfit between Ta and Cu decreased with temperature.

By contrast, in larger Ta clusters, most of the initial FCC structures transformed to BCC already during the static relaxation (Fig. 5.1b). This resulted in nearly complete loss of coherency, and during the subsequent high-temperature anneals, the fraction of the BCC structure in the cluster increased (Fig. 5.2). For smaller or larger Ta clusters, difference in the phase percentage increased with an increase in temperature, however for the intermediate Ta clusters (e.g., with the radius of 2.5 nm and 3.0 nm), the difference was very small and phases compete to dominate each other. On increasing the cluster diameter,
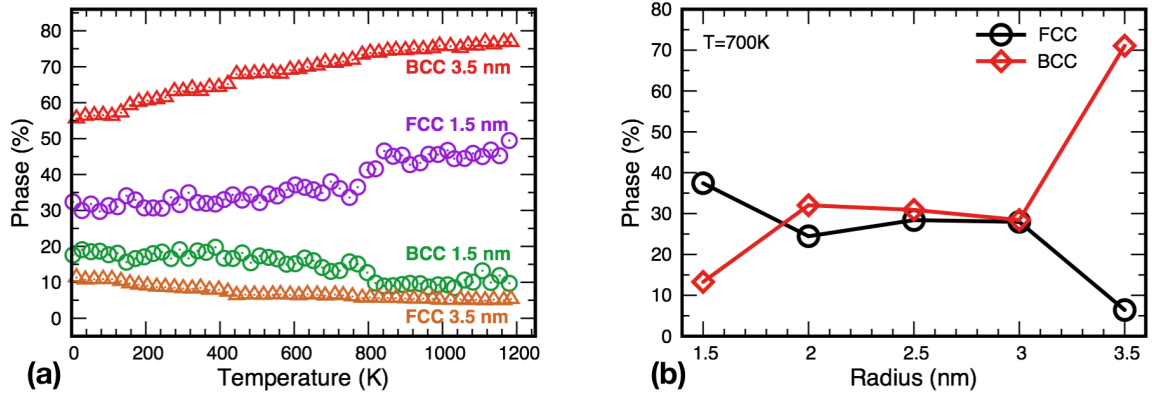
Figure 5.2: (a) Temperature dependence of the FCC and BCC phases in Ta clusters for two cluster sizes (1.5 nm and 3.5 nm). (b) Variation of Ta cluster phases with radius at a particular temperature 700 K. Phases changes from coherent to incoherent with the Cu matrix as radius increases.

Ta phase changed from FCC to BCC losing coherency with the Cu matrix. Figure 5.1b shows that the Ta cluster was coherent for radius 1.5 nm and incoherent for radius 3.5 nm with the Cu matrix at 700 K.

In experiments, the size distribution of Ta precipitates has been classified into two groups: one as a nanocluster containing a small aggregation of Ta atoms (10-50 atoms) with an average diameter 3.18±0.86 nm and other as a particle having a much larger size with average diameter 39±19 nm [35]. The coherency of these clusters was indicated as coherent, semi-coherent, and incoherent for the diameter <3.898 nm, 3.898 to 15.592 nm, and >15.592 nm, respectively. Thus, Ta clusters were found to lose coherency at smaller sizes in simulations than seen in experiments.

The loss of coherency was accompanied by the emission of dislocation loops into the Cu matrix, as illustrated in Fig. 5.3a. This figure shows a single Ta particle with an initially coherent boundary. The loss of coherency resulted in the formation of misfit dislocations at the particle/matrix interface. These dislocations then separated from the particle and formed loops gliding into the Cu matrix along (111) planes. For clarity, the perfect FCC Cu atoms are not shown in Fig. 5.3a and the particle was cut in halves during the visualization
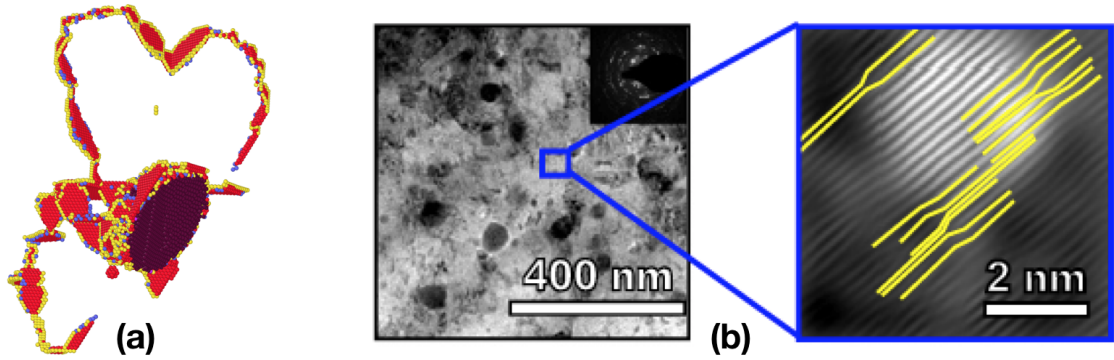
Figure 5.3: a) Dislocation loops emitted by the Ta particle having a radius of 3.5 nm at 700 K. The dislocation loop splits into partials separated by a stacking fault (red color). The FCC Cu atoms were removed for clarity and half of the Ta particle was cut out to reveal its spherical cross-section. b) TEM (transmission electron microscopy) image of Cu-10at.%Ta alloy and IFFT (inverse fast Fourier transform) image of Ta particle. (Ref. [35])

to reveal its cross-section and a better view of the dislocation loops. The dislocations split into Shockley partials (yellow) separated by a stacking fault colored in red. It is well known that a coherent nanocluster can lose coherency once it grows above a critical diameter. This happens when the elastic energy with the nanocluster becomes large, and it is energetically favorable for a dislocation to form at the matrix-nanocluster interface. This has been indeed observed in experiments and Fig. 5.3b shows the high-resolution TEM (HRTEM) image of nanocluster with diameter 4.11 nm, where the yellow lines along the Cu-Ta interface are the misfit dislocations. The generation of such dislocations is easier for an incoherent nanocluster in comparison to a coherent nanocluster. This dislocation raises the free energy of the system to an amount that equals to its formation energy, but this increase in energy is compensated by the decrease in the self-energy of the nanocluster. Due to the presence of the misfit strain around nanocluster, the pinning-depinning of propagating dislocations during the deformation within the matrix will be hindered. This hindrance will have a direct consequence on the mechanical behavior. Hence, the change in coherency can be linked to the change in mechanical properties.

Because of the complex two-phase structures of the clusters and the thermal noise at high temperatures, it was not possible to accurately determine the interplanar spacing between
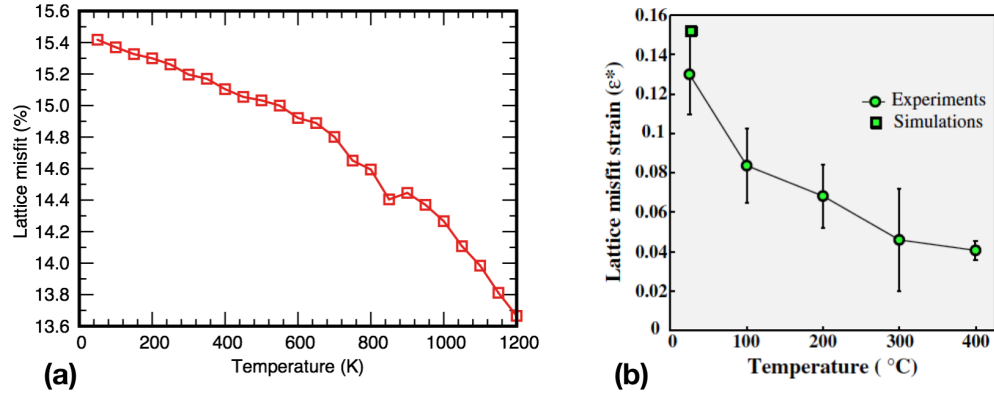
Figure 5.4: (a) Lattice misfit strain evolution as a function of temperature for the Ta nanocluster of radius 3.5 nm. The misfit strain decreases from 15.94% to 13.6%. (b) Experimentally observed misfit strain evolution as a function of temperature [35].

Ta atoms. Instead, the following crude estimates were made. Knowing the dimensions of the simulation block, the atomic volume of FCC Cu Ω_{Cu}, and the numbers of Cu and Ta atoms, it was possible to extract the average volume Ω_{Ta} per Ta atom in the cluster. The average atomic spacing was estimated for Cu and Ta by $\Omega_{Cu}^{1/3}$ and $\Omega_{Ta}^{1/3}$, respectively. The misfit was then estimated from the equation.

$$\epsilon = \frac{2(\Omega_{Ta}^{1/3} - \Omega_{Cu}^{1/3})}{(\Omega_{Ta}^{1/3} + \Omega_{Cu}^{1/3})} \tag{5.1}$$

The misfit estimated from this equation as a function of temperature is shown in Fig. 5.4. The misfit strain initially as high as 15.94% decreased with the increase in temperature and was reduced to a value of about 13.6%. This decrease can be explained by the structural relaxation of the clusters resulting in increased coherency and transformation to a more thermodynamically stable structure. Moreover, the difference in thermal expansion factors of Cu and Ta cluster reduces the lattice parameter difference at high temperatures. This behavior agrees qualitatively with experimental observations. Quantitatively, however, the amount of this decrease is smaller than in the experiment (Fig. 5.4b), where the misfit

60

strain is estimated to reduce to 4% at 400 ^{0}C. Nevertheless, the misfit strain calculated from atomistic simulations at room temperature agrees well with in situ TEM experimental measurement, as shown in Fig. 5.4b.

5.4   Conclusion

The atomistic simulations confirmed that small Ta clusters have FCC structure predominantly and remain at least partially coherent with the Cu matrix. As the cluster size increases, it loses coherency with the Cu matrix. The loss of coherency forms misfit dislocations at the particle/matrix interface and emits into the matrix forming loop within the clusters. The lattice misfit between the Ta clusters and the matrix decreases at higher temperatures, promoting better coherency. Although the simulation results are generally consistent with the experiment, there are some deviations on the quantitative level. For example, the clusters were found to lose coherency at smaller sizes than seen in the experiment. Also, the rate at which the misfit decreases with increasing temperature is on the lower side of the experimental data. The main source of these deviations is likely to be the absence of vacancies in the present simulations. Indeed, the mere replacement of Cu atoms by significantly larger Ta atoms creates a cluster in a state of strong compression. It is very likely that at higher temperatures, such clusters attract vacancies, which then dissolve into the clusters and create a much larger vacancy concentration than in stress-free Ta. This should result in a decrease of the lattice parameter inside the cluster and partial relief of the coherency stresses and strains. Despite this limitation, atomistic simulations were able to reveal critical structural changes within the Ta based clusters, which remained mostly (although not fully) coherent with the Cu matrix.

Chapter 6: Atomistic study of core-shell structure nanoparticles in Cu-Ta alloys

6.1 Introduction

Studies of nanocrystalline Cu-Ta alloys through experiments [16, 30, 33–35, 39, 142] and atomistic simulations [29, 32, 131, 143] have well established its technological and scientific significance for high-temperature and high-strength applications with unexceptional mechanical and thermal stability. The extraordinary characteristic of these alloys is primarily due to the effect of immiscible Ta solute on thermodynamics and mobility of internal interfaces, primarily grain boundaries (GBs). Although each of these elements lacks mutual solubility, Ta atoms forced into the Cu matrix forms supersaturated Cu-rich solution with Ta atoms precipitated in the form of nanoclusters [30, 39].

Previous atomistic simulations [29, 32, 131] have demonstrated the formation of Ta clusters, especially at GBs and grain interiors, and their role in stabilizing grain. The stability arises from Ta clusters that pin GBs by the Zener mechanism [22–24], thereby preventing grain mobility and grain coarsening. These clusters were formed either by equilibrating the system with Monte Carlo (MC) simulations or segregating dispersed Ta atoms near the GBs with molecular dynamics (MD) simulations. Most of these clusters were nanoclusters with an average size of 1 nm and coherent with the Cu matrix.

The current simulation is focused on understanding the formation of larger Ta precipitates (≥ 1 nm) in the immiscible Cu matrix as experimentally observed through a transmission electron microscope (TEM) or atom probe tomography [30, 39]. Experimental observations have reported a wide range of Ta clusters with sizes ranging from atomic nanoclusters to much larger nanometer-scale Ta precipitates and phases coherent, semi-coherent, or incoherent with the Cu matrix. These larger size Ta precipitates are responsible for changing

mechanical properties emitting dislocation loops in the Cu matrix [35]. Some of these clusters are observed to have a core-shell type structure with embedding Cu atoms as core and Ta as shell [39]. Core-shell type nanoclusters have recently been attributed to the excellent strength and ductility of molybdenum alloys [40] and steels [41]. Interactions of core-shell particles with grain boundaries have a profound effect on the inherent mechanical properties and challenge the long-established theoretical frameworks related to the mechanical behavior of materials. As Cu-Ta is an immiscible alloy, it is essential to investigate whether it has any prospect in forming core-shell structures. Thus, we carried out atomistic simulations to understand the formation mechanism of larger core/shell Ta particles and their interface behavior to have a firm understanding of thermal stability, strength, and ductility of Cu-Ta material.

6.2 Methodology

Study of the formation of core/shell Ta structures has been carried out by performing MC and MD simulations with the use of angular-dependent potential (ADP) describing the interatomic interactions for Cu-Ta systems [32]. MD simulations were employed in large-scale atomic/molecular massively parallel simulator (LAMMPS) code [107], and MC simulations were conducted in parallel grand canonical Monte Carlo (ParaGrandMC) simulation code developed by V. Yamakov (NASA).

While performing MC simulations with the composition controlled Metropolis scheme [91, 108] up to 4 at.%Ta, it only formed smaller and coherent Ta clusters randomly distributed in a single crystalline lattice and predominantly located at the GB in bicrystal. These clusters had the same size distribution as described in previous simulation [29,32,131], and the size distribution was consistent regardless of alloy composition and temperature. There was only a change in the number density of clusters with a change in composition. The sizes of the simulation blocks were $10.7{\times}10.7{\times}10.7$ nm for single crystal and $21.3{\times}21.3{\times}58.7$ nm for bicrystal having plane GB $\Sigma17(530)[001]$. This approach did not

result in the formation of larger Ta precipitates.

Similarly, annealing of nonequilibrium solutions having Ta concentrations up to 4% in single and bi-crystalline alloy resulted only in the formation of Ta clusters having size much smaller than MC simulations. The precipitated cluster size was smaller even after annealing non equilibrium solutions for 5 μs with accelerated molecular dynamics (AMD) [144–147] simulation at 1100 K. This implied us to draw the conclusion that larger Ta clusters experimentally observed in the Cu matrix or at the GBs couldn't be formed by the diffusion of randomly distributed small concentration of Ta atoms on Cu matrix. Ta concentration should be critically high enough to diffuse and coarsen into larger size nanoparticles, or there should exist Ta concentrated region to agglomerate neighboring Ta atoms on its surface.

It has been described in the literature that a metastable Cu-rich solid solution can accommodate up to 10-20at.%Ta with higher concentrations causing amorphization [48, 49, 67]. A metastable Cu-Ta solution is formed by the addition of Ta atoms in the FCC Cu solution, which replaces FCC Cu lattice, diffuses, and forms clusters during thermal processing when the composition becomes critical. Thus, we believed larger core/shell Ta structures should be formed by diffusion from the highly amorphous region and focussed on the crystallization of amorphous solution. With the random replacement of Cu atoms by Ta atoms, Cu-50at.%Ta alloy of radius 3.5 nm was created at the center of the cubic FCC Cu simulation block having dimension 14.5×14.5×14.5 nm (2.56×10^5 atoms) as shown in Fig. 6.1. The structure was slowly heated to the temperature of 900 K and then annealed with the NPT ensemble. The solution remained amorphous when annealed for 17 ns at 900 K. Therefore, the solution was rapidly expanded to anneal at 1000 K with a higher diffusion rate. During the simulation, snapshots of the simulation block were saved at a regular interval of time. The snapshots were observed with OVITO [110] for visualizing structure and analyzing crystallization through bond angle parameter analysis.

Further, to mimic the crystallization of amorphous solution at 1000 K, constrained composition controlled MC simulations were performed to obtain desired Ta concentration only within the sphere of radius 3.5 nm of the simulation block. Alloy composition within the
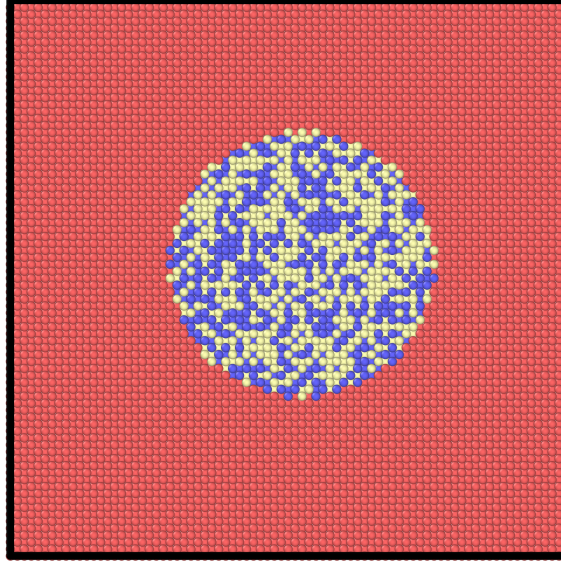
Figure 6.1: Simulation block containing spherical amorphous solution Cu-50at.%Ta alloy in a radius of 3.5 nm. The Cu matrix is colored in red with amorphous Cu and Ta atoms in white and blue color, respectively.

sphere was varied between 30-80at.%Ta running 10^5 MC steps for each MC simulation. Redistributed Cu and Ta atoms within the sphere was analyzed for quantifying crystallization and the evolution of nanostructure.

6.3 Results

While annealing the system having a spherical solution of radius 3.5 nm and composition Cu-50%at.Ta at 1000 K with MD NPT ensemble, Ta atoms redistributed within the amorphous sphere in a more organized structure. The rearrangement of configuration was facilitated by the diffusion of Cu and Ta atoms. Dispersed Cu atoms diffused much faster than Ta atoms, and its's self lattice diffusion favored movement within the amorphous solution and between the matrix and the solution. Since Ta diffusion is extremely slow even at the melting temperature T_m of Cu [29], Ta atoms did not diffuse into the Cu matrix. Instead, the diffusion process redistributed Ta coarsening nearby Ta atoms inside the solution and

on the interface of solution-matrix.
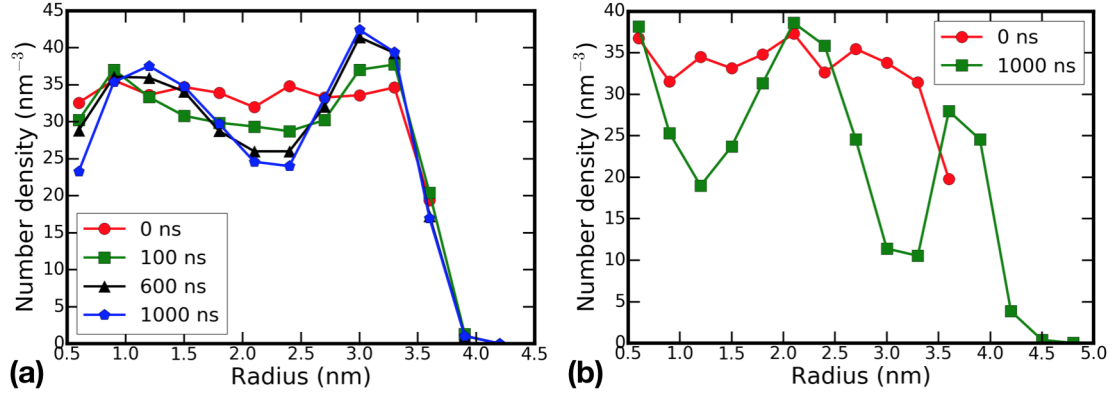
Figure 6.2: Redistribution of (a) Ta and (b) Cu atoms during annealing of Cu-50%at.Ta random alloy with MD NPT ensemble at 1000 K.

Figure 6.2a shows the redistribution of Ta atoms during annealing as a function of radius. Initially, there was a uniform distribution of Ta atoms, as indicated by the red curve. As the annealing continued, Ta atoms redistributed, forming two concentration peaks, one lying close to the interface and other towards center. Since the number of particles was conserved and Ta atoms could not diffuse into the matrix, this segregation should always be accompanied by the formation of depletion zone within the spherical region of amorphous solution. As expected, one could notice the formation of a depletion zone at a radius of ∼ 2.5 nm inside the sphere.

Figure 6.2b shows the redistribution of dispersed Cu atoms initially lying within the amorphous solution. There is Cu enrichment in the depletion zone of Ta and Cu depletion in the Ta segregated region. The second enrichment peak near the interface and long tail in the Cu redistribution curve are due to the self-diffusion of dispersed Cu atoms into the matrix. An increase in the concentration peak of segregation and depletion zone for both elements was observed with an increase in annealing time.

Redistribution curves of both elements represented the same qualitative phenomena except for the region close to the center. The plot was not extended to the center to avoid
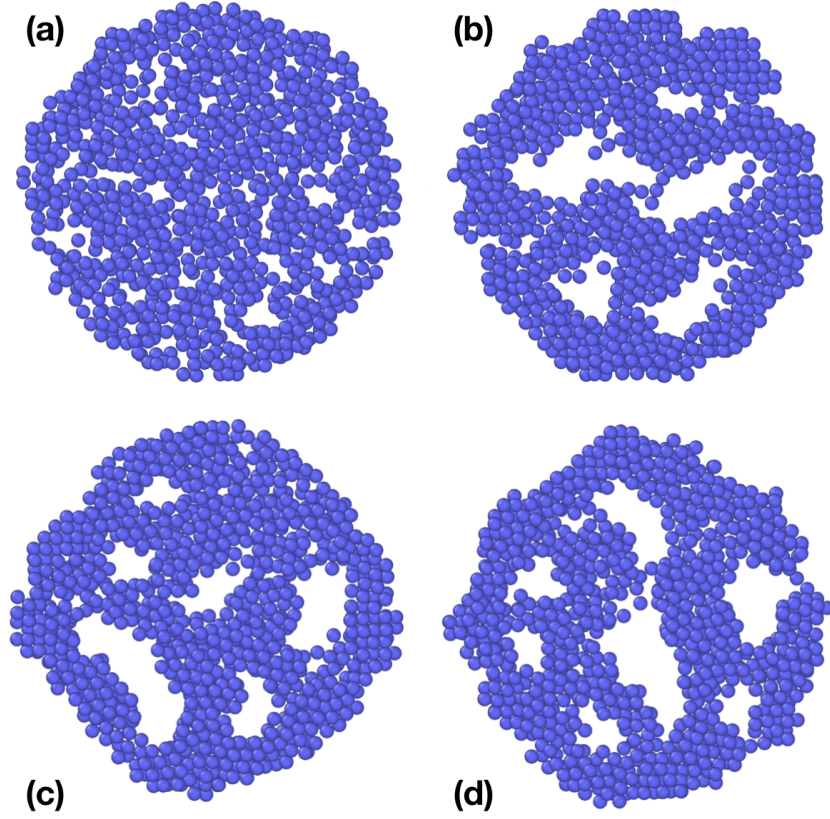
Figure 6.3: Annealing of spherical solution Cu-50%at.Ta by MD NPT ensemble at 1000 K. (a) Uniformly dispersed Ta atoms in the beginning. Observations from (b) x[1 0 0] direction, (c) y[0 1 0] direction and (d) z[0 0 1] direction at 1000 ns. Thickness of the slice is $6\mathring{A}$ and passes through the center of the spherical solution.

significant statistical error arising from less number of atoms. Examination of snapshots displayed that uniformly dispersed Ta atoms were coarsened into partially concentric interconnected shells separated by Cu atoms. The concentric shells consist of pores from which Cu atoms were diffusing inward and outward. These concentric shells became more distinct with the separation of Cu and Ta atoms as the process of annealing was prolonged. Figure 6.3 shows the slices passing through the center observed from cubic crystal orientation x[100], y[010], and z[001] directions. The empty spaces are the regions occupied by Cu atoms.
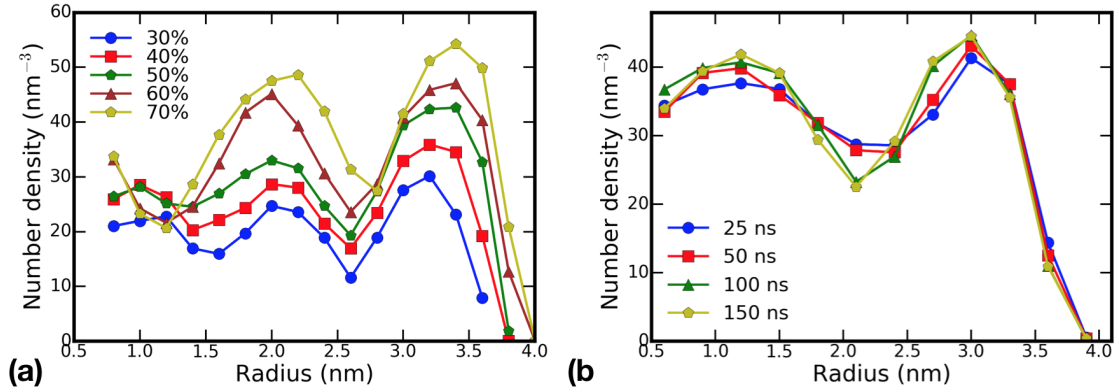
Figure 6.4: Redistribution of Ta atoms within a sphere of radius 3.5 nm at 1000 K. (a) MC simulation and (b) Hybrid MD simulation.

To understand more regarding the formation of concentric shells through the redistribution of Cu and Ta atoms, MC simulations were performed with a constrained composition controlled algorithm which allows random movement and exchange only within the Cu atoms initially lying within the sphere of radius 3.5 nm rather than in the entire simulation block. The composition within the sphere was varied from 30at.%Ta to 80at.%Ta. Figure 6.4a shows the MC distribution of Ta atoms for various compositions within the predefined spherical region. As observed in MD simulation, each of these curves revealed a double peak with the depletion zone at radius ~ 2.5 nm. These peaks became much sharper with the increase in composition up to 70at.%Ta. At 80at.%Ta, the double peak was not as prominent as the lower composition.

For the lower composition 30at.%Ta and 40at.%Ta, Ta atoms inserted by MC simulations were small isolated clusters coherent with Cu matrix and were arranged in a concentric pattern within the predefined spherical region (Fig. 6.5a and 6.5b). With the increase in composition, the interface was covered mostly by larger size clusters having smaller ones lying inwards. As the composition reached 60at.%Ta, Ta atoms lying on the surface behaved as shell having pores filled with Cu atoms. At 80at.%Ta, inner Ta atoms behaved as single-core interconnecting with an outer shell.
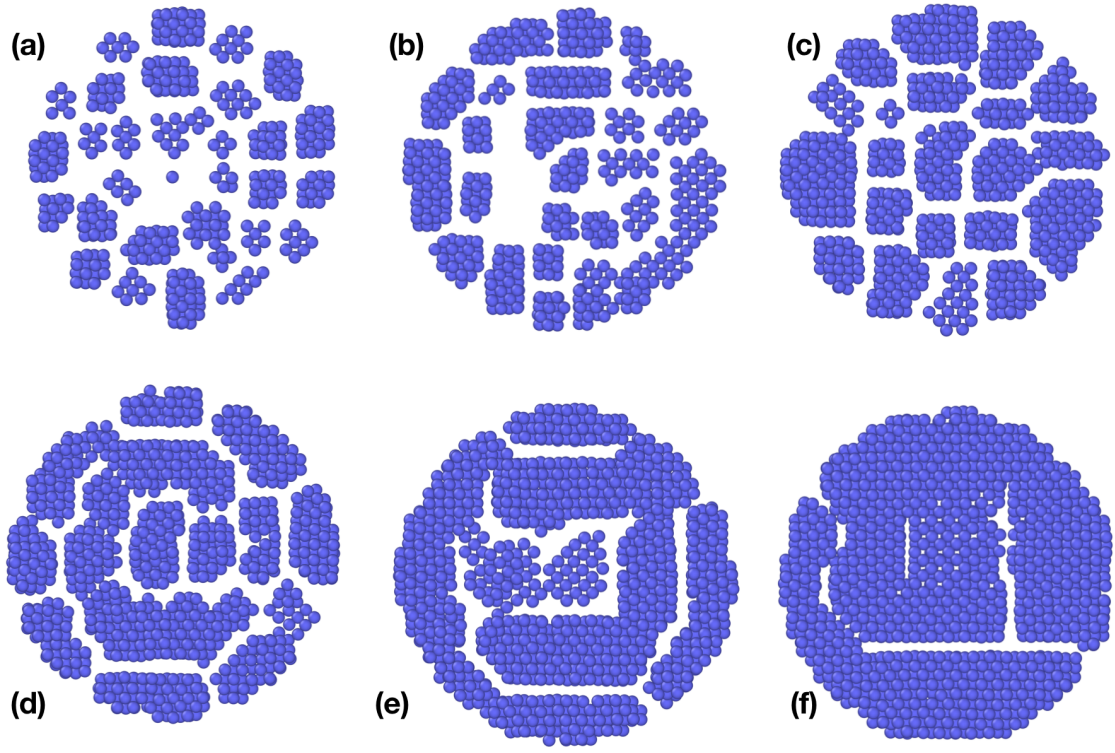
Figure 6.5: Slice of MC simulation observed from y[0 1 0] direction for various compositions:-
(a) 30at.%Ta, (b) 40at.%Ta, (c) 50at.%Ta, (d) 60at.%Ta, (e) 70at.%Ta and (f) 80at.%Ta.
Thickness of slice is $6\mathring{A}$.
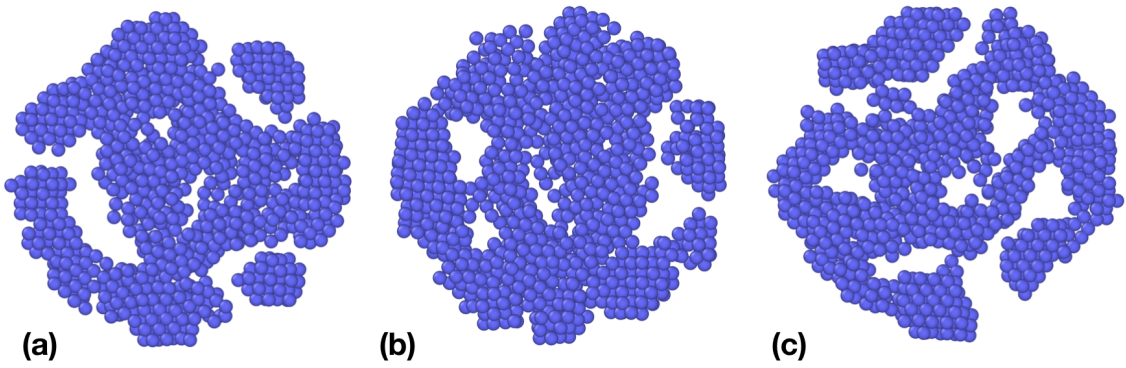
Figure 6.6: Slice of hybrid MD simulation at 150 ns. Observations from (a) x[1 0 0] direction,
(b) y[0 1 0] direction and (c) z[0 0 1]. Thickness of slice is $6\mathring{A}$.

We also performed hybrid MD simulations involving one MC simulation after every one nanosecond of MD simulation for Cu-50at.%Ta alloy. The MC simulation was short, involving 100 MC steps. Hybrid MD simulation also exhibited the same dynamics of the formation of shell structure as observed in MD and MC simulations (Fig. 6.4b and Fig. 6.6). The concentration peaks of the segregation and depletion zone became much more apparent in a short time interval than MD simulation.
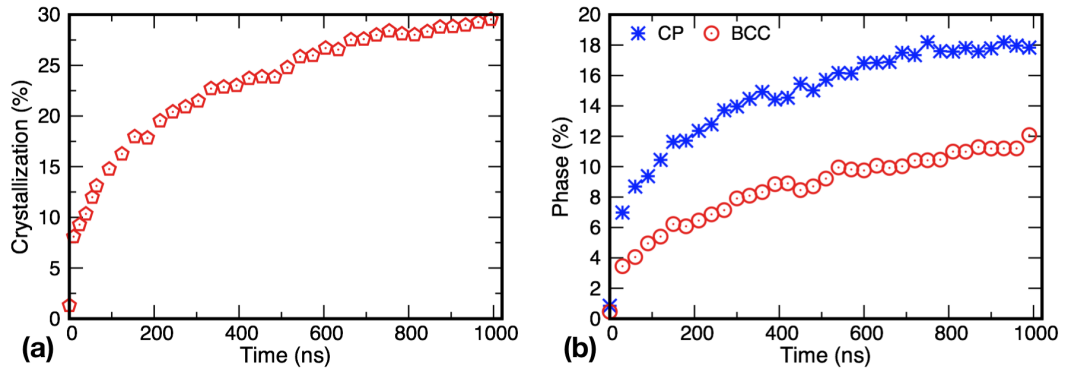
Figure 6.7: (a) Crystallization of Ta atoms and (b) phase evolution during annealing of spherical Cu-50at.%Ta solution by MD NPT ensemble at 1000 K.

Apart from the redistribution of atoms by the process of diffusion, Ta atoms were crystallized from the amorphous solution with the continuation of annealing. The fraction of crystallized Ta atoms increased with the evolution of time. Figure 6.7 shows the percentage of crystallized Ta atoms and their phase distribution during the annealing of Cu-50at.%Ta alloy at 1000 K. These parameters were obtained from OVITO [110] through bond angle parameter analysis. Of the total number of Ta atoms in spherical Cu50at.%Ta alloy, 30% of Ta atoms were observed to be crystallized when annealed for 1000 ns. The phase of the crystalline atoms was predominated by the close-packed structure. We referred to both FCC and HCP as close-packed structures as the atoms in the third layer may not be distinguishable when there is the presence of a significant fraction of other non-structural atoms. Most of the crystallized Ta atoms were located close to the interface and partially towards

the center. Crystallized Ta atoms displayed a concentration peak in the same radii where the enrichment of Ta atoms occurred during the redistribution of atoms (Fig. 6.8).
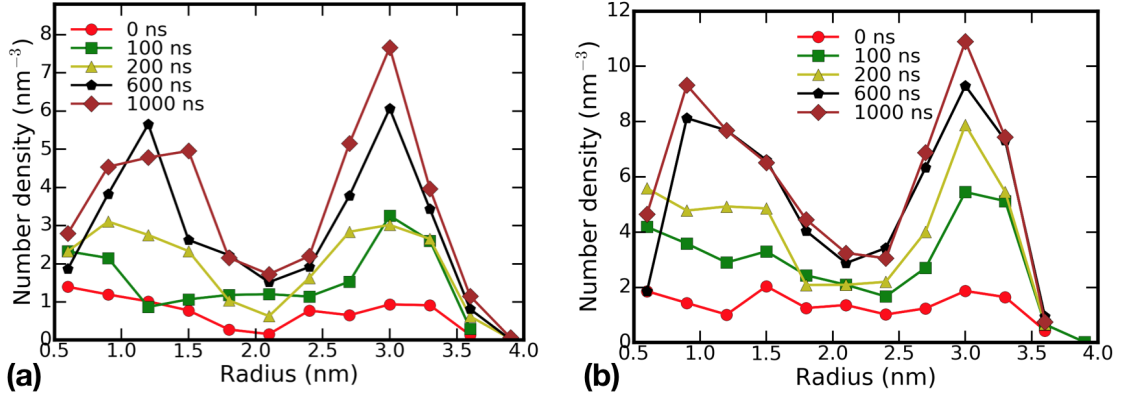
Figure 6.8: Distribution of (a) close-packed and (b) BCC phase of crystallized Ta atoms.

Thus, we believe that whenever Ta atoms are non uniformly distributed by mechanical alloying leaving Ta rich concentrated zone in single-crystalline Cu matrix, diffusion mechanism aids in redistributing their position through the replacement of FCC Cu lattice. While rearranging their position, Ta atoms come together to other dispersed Ta atoms and are coarsened to form small isolated clusters. The slow diffusion rate of Ta does not allow Ta atoms to diffuse into the Cu matrix. Only the Cu movements are allowed by the self lattice diffusion. Thus, when the concentration becomes critical, smaller clusters combine to form larger clusters within the amorphous region, transforming central atoms into a crystalline structure. Accordingly, there are two distinct undergoing physical phenomena. The first one is the redistribution of atoms aid by diffusion mechanism within the nonequilibrium region, and the second one is the crystallization achieved through the coarsening of redistributed neighboring atoms. The phenomena of coarsening also trap dispersed Cu atoms lying between those clusters. The presence of Cu atoms has an advantage in reducing the bulk energy of the cluster. Thus, instead of forming the bulk cluster, Ta atoms aggregate in spherical shell trapping Cu atoms to minimize the stress condition acting from the interface

and matrix. As a result, Ta rich region will arrange in concentric or partially interconnected concentric shell filling Cu atoms in between them. These shells may have pores to allow diffusion of Cu between the matrix and the clusters.

6.4   Conclusion

MC and MD simulations have demonstrated that the redistribution of Cu and Ta atoms in a Ta-rich random solution forms a single/double core-shell nanostructure. When Cu atoms diffuse within the amorphous region or into the matrix, Ta atoms tend to aggregate and form small isolated clusters. These small isolated clusters further coarsened together to form larger clusters transferring central atoms into a crystalline structure. During the coarsening process, Cu atoms are also trapped within the Ta clusters forming a core-shell structure that reduce the energy. Thus, the formation mechanism of the core-shell structure observed in Cu-Ta alloys can be explained with two distinct physical phenomena viz., redistribution of Cu and Ta atoms by the process of diffusion and crystallization through the coarsening of Ta atoms.

Chapter 7: Atomistic study of superplastic behavior in Cu-Ta alloys

7.1 Introduction

Nanocrystalline materials exhibit deformation-induced grain growth and poor microstructural stability even at lower temperatures compared to their coarse-grained counterparts. The strain rate sensitivity (SRS) index (m) is an essential parameter in characterizing the deformation behavior of structural materials. Materials display superplastic behavior when the magnitude of m increases above 0.3. Coarse-grained materials and alloys generally exhibit low strain rate sensitivities with m value usually less than 0.01. However, it undergoes a rapid increase in magnitude as the average grain size is decreased and/or the temperature is increased. The magnitude of m approaches one as the homologous temperature is increased [148]. Even at a lower temperature, m has been found to increase significantly with a continual reduction in grain size. For instance, in pure Cu, Chen et al. reported an increase in the value of m from 0.009 to 0.038 when the grain size changes from coarse-grained polycrystalline to nanocrystalline Cu at room temperature [149]. Wei et al. also reported m values as high as 0.06 for Cu grain sizes as small as 10 nm [150]. With a reduction in grain size, a significant fraction of grain boundaries increases, which changes deformation behavior from dislocation nucleation and glide to grain boundary processes such as grain boundary rotation, grain boundary sliding, and viscous flow [151]. Therefore, it is expected for nanocrystalline metals and alloys to exhibit extreme SRS values ($1 \geq m > 0.3$) when deformed at higher temperatures.

Nanocrystalline Cu-Ta alloys exhibit extraordinary strength and structural stability at high temperatures [29–35]. This has been attributed to Ta clusters precipitated within grains and along GBs, which strongly pin GBs by the Zener pinning mechanism inhibiting

further grain growth [131,141]. However, the SRS behavior of Cu-Ta alloys at such extreme temperatures is unknown. It is fundamentally important to explore the dependence of the SRS parameter with temperature to understand the lack of superplastic behavior in Cu-Ta alloys. Thus, the SRS behavior of Cu-Ta alloy is explored through atomistic simulation as high as 75% of homologous temperature. The goal of the present work is to demonstrate that nanocrystalline Cu-Ta alloy exhibits limited SRS dependence with temperature.

7.2   Methodology

The atomistic simulations utilized the angular-dependent interatomic potential for the Cu-Ta system [32], reproducing a large number of physical properties of this system in agreement with experimental data and first-principles calculations. The molecular dynamics (MD) simulations employed the Large-scale Atomic/Molecular Massively Parallel Simulator (LAMMPS) [107]. The Monte Carlo (MC) simulations constituted an important part of the methodology and were conducted using the parallel MC code ParaGrandMC recently developed by V. Yamakov (NASA) [132]. The code implements a number of statistical ensembles, including the composition-controlled MC algorithm that brings the system to thermodynamic equilibrium at a given temperature and average chemical composition under zero-stress conditions. The trial moves of the MC process include small random displacements of randomly selected atoms in a random direction and a random re-assignment of the chemical species of the atoms to either Cu or Ta.

The study was carried out in a polycrystalline Cu sample constructed by the Voronoi tessellation method and contained 32 grains with an average grain size of 12.5 nm. The sample contained about 5.4 million atoms and had the approximate dimensions of 40 nm × 40 nm × 40 nm with periodic boundary conditions in all three Cartesian directions. The GB structures were optimized by a procedure described elsewhere [32,93,94].

To obtain a polycrystalline alloy, an equilibrium distribution of Ta atoms was created in the initial pure-Cu polycrystal by MC simulations at the temperatures of 300 and 800K with

the target composition of 4 at.%Ta. At these temperatures, no appreciable grain growth was observed during the MC simulations (see Fig. 7.6). The zero-pressure boundary conditions ensured that the introduction of the oversized Ta atoms did not create internal stresses. Ta was found to form nanoclusters located primarily at the GBs.

In the MD simulations of the polycrystalline sample, it was heated to the desired temperature and, after thermal equilibration, subject to isothermal uniaxial deformation in one of the Cartesian directions while keeping zero stresses in the two remaining directions. The sample was first compressed by 2% and then elongated back to its original shape in order to generate some defects in the otherwise too perfect GBs and possibly inside the grains. Following this pre-straining step, the sample was subject to a slow 15% compression with a constant strain rate $\dot{\epsilon}$. The compressive stress σ was monitored during the simulations, and multiple snapshots were saved to keep track of the structure evolution. The compression tests were conducted at the temperatures of 300 and 1000 K with strain rates between 5 $\times 10^6$ and 10^9 s^{-1}.

7.3 Results

7.3.1 Stress-strain curves

Figure 7.1 shows stress-strain curves for the polycrystalline Cu-4at.%Ta alloy at two different temperatures 300 and 1000 K with strain rates ranging from 10^7 to 10^9 s^{-1}. The maximum at about 5% strain reflects the well-known stress-overshoot effect often observed in MD simulations at large strain rates. Despite the pre-straining, the initial GB structures are too ordered and cannot easily generate dislocations. As a result, the material displays an excessively high strength until the GBs generate a sufficient amount of dislocation for a steady-state flow. The overshoot effect nearly disappears at slower strain rates. Moreover, the stress-strain curves did not show any strain hardening at both high and low temperatures.
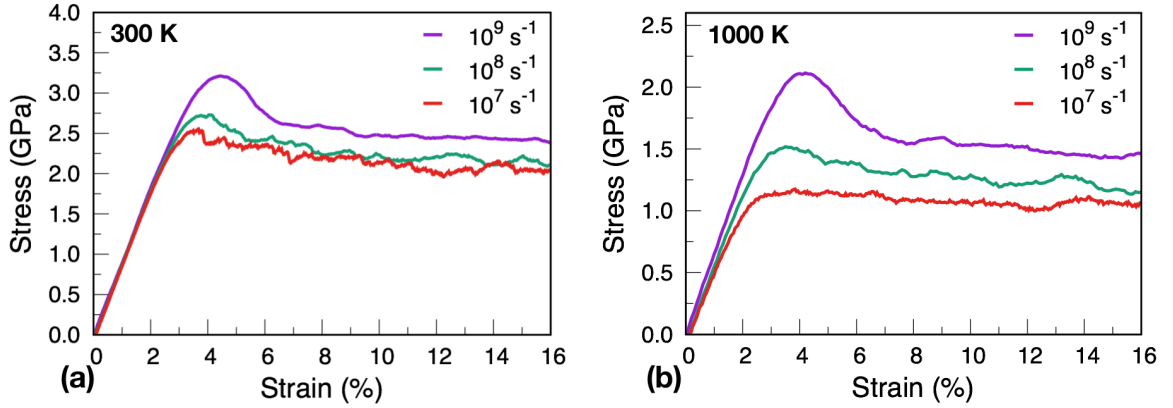
Figure 7.1: Representative engineering stress-strain curves obtained by simulated compression tests of nanocrystalline Cu-4at.%Ta alloy at the temperatures of (a) 300 K and (b) 1000 K. The strain rates in s^{-1} are indicated in the legend.

7.3.2 Strain rate sensitivity

The flow stress σ_f at each strain rate was evaluated as the stress at 10% deformation. This deformation matches the experiment and is large enough to avoid the stress-overshoot impact. Figure 7.2a shows the flow stress as a function of strain rate. As expected, the flow stress decreases with increasing temperature and slightly increases with the strain rate. To demonstrate the temperature effect on the stain-rate sensitivity, Fig. 7.2b shows the same σ_f vs. $\dot{\epsilon}$ functions except that the flow stress is normalized by its value at the slowest strain rate. It is evident that at 1000 K, the strain rate has a stronger effect on the flow stress than at 300 K. To quantify this difference, the strain-rate sensitivity index m=$\frac{d(ln\sigma_f)}{d(ln\dot{\epsilon})}$ was computed from the slopes of the ln σ_f vs. ln $\dot{\epsilon}$ plots. The values obtained were m = 0.029 ± 0.004 at 300 K and m = 0.075 ± 0.004 at 1000 K. These numbers agree reasonably well with the experimental numbers [152] obtained from compression tests performed on Cu-10at.%Ta alloy over a wide range of deformation rates (10^{-4}-10^{1} s^{-1}) and temperature conditions (297 K - 1273 K), as shown in Fig 7.3.

Similar deformation behavior was found in pure Cu. The stress-strain curves look qualitatively similar to those for the alloy. The flow stress is lower than for the alloy (Fig. 7.2a).

76
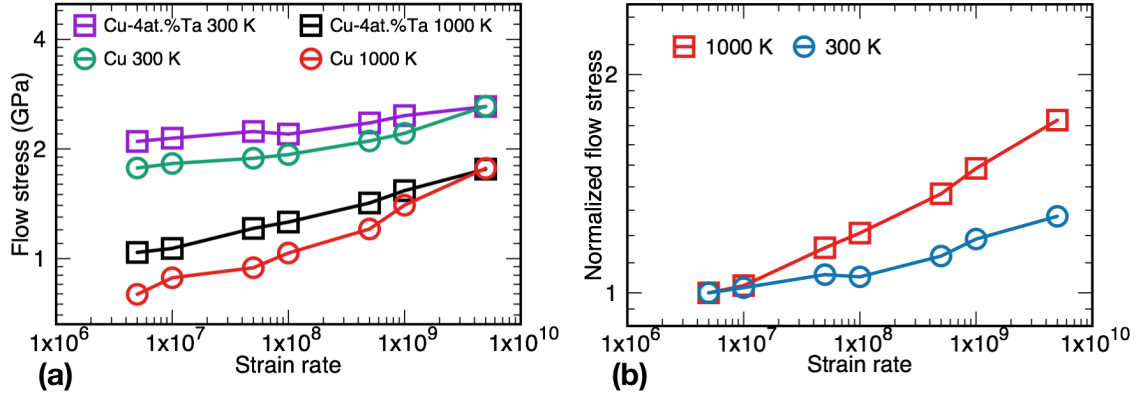
Figure 7.2: (a) Flow stress as a function of strain rate for pure Cu and the Cu-4at.%Ta alloy at 300 and 1000 K. (b) Normalized flow stress as a function of strain rate for the Cu-4at.%Ta alloy at the temperatures of 300 and 1000 K.
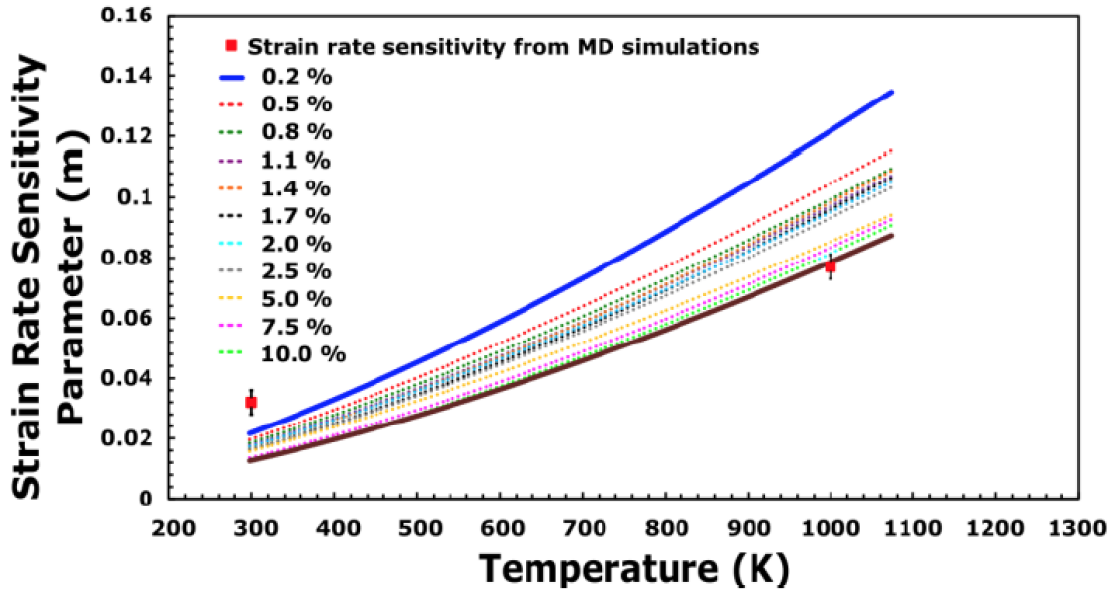
Figure 7.3: Comparison of simulated strain rate sensitivity value with experimental curves showing the influence of temperature on strain rate sensitivity at various strain levels for nanocrystalline Cu-10at.%Ta alloy [152].

As shown previously [29–35, 131, 141], the strengthening effect is due to the Zener pinning of GBs by Ta nanoclusters. The simulations reveal a larger strain rate sensitivity of Cu in

77

comparison with the alloy at both temperatures. The strain-rate sensitivity index is m = 0.039 ± 0.005 at 300 K and m = 0.098 ± 0.009 at 1000 K. This difference is evident from the σ_f vs. $\dot{\epsilon}$ plots showing systematic upward deviations of Cu points with increasing strain rate (Fig. 7.4).
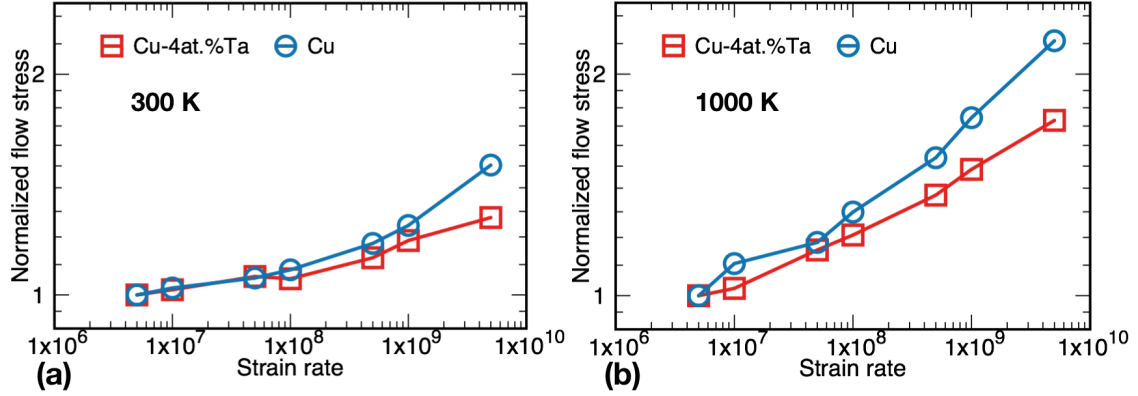
Figure 7.4: Normalized flow stress as a function of strain rate for the Cu-4at.%Ta alloy and pure Cu at the temperatures of (a) 300 K and (b) 1000 K.

7.3.3 Microstructural evolution

Figure 7.5 shows the microstructural evolution of polycrystalline Cu when deformed to about 12% under compression with strain rate 5×10^6 s^{-1} at 300 K and 1000 K, respectively. At 300 K, polycrystalline Cu exhibited enormous dislocation activities with dislocation emission, propagation, and twinning. Dislocations emitted from the GBs moved freely inside the grains and were absorbed at the opposite GB. However, at 1000 K, polycrystalline Cu exhibited significant grain growth and grain rotation along with twinning, dislocation emission, and propagation (compare Fig. 7.5c and Fig. 7.5d).

Figure 7.6 shows the microstructural evolution of Cu-4at.%Ta alloy when deformed to 12% using the strain rate 5×10^6 s^{-1} at 300 K and 1000 K, respectively. Although there is a significant difference between two simulated temperatures, the initial structures
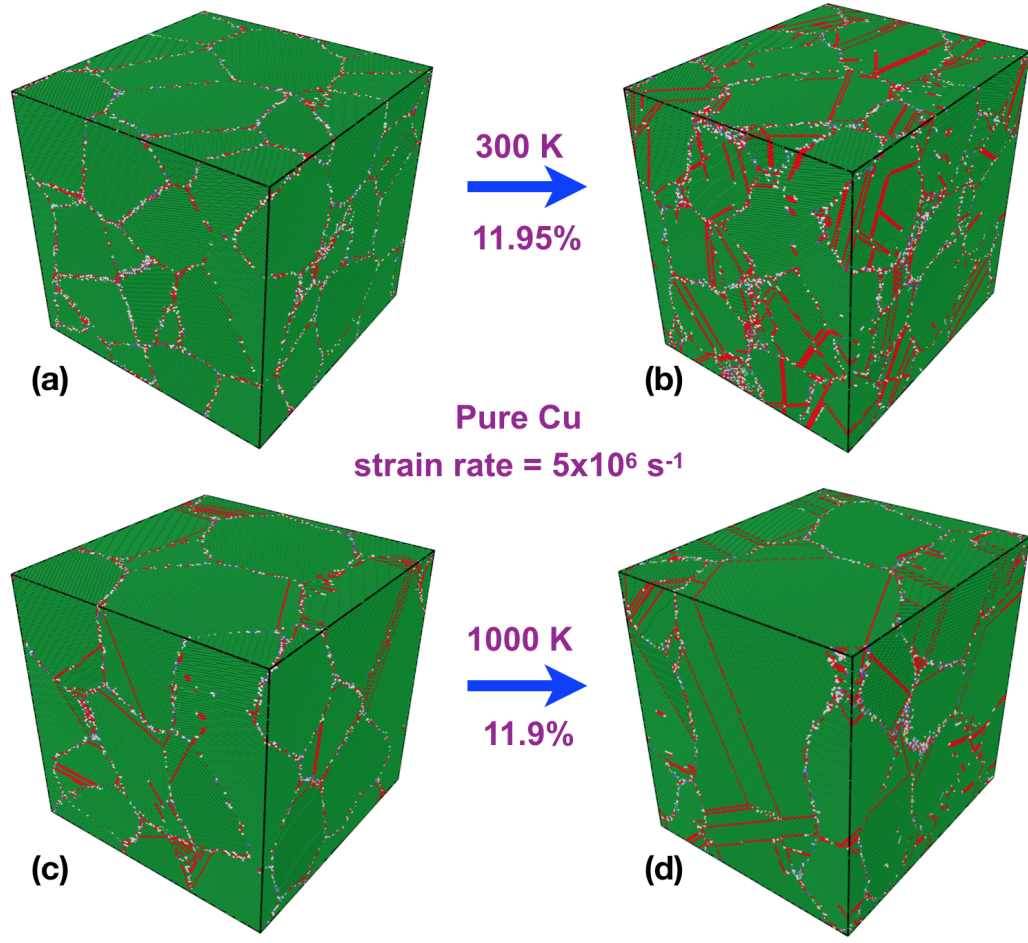
Figure 7.5: Microstructural evolution of pure Cu during deformation with the 5×10^6 s^{-1} strain rate at (a) 300 K and (b) 1000 K. FCC and HCP atoms are colored in green, and red color respectively.

of 300 K (Fig. 7.6a) and 1000 K (Fig. 7.6c) with the presence of Ta clusters (yellow atoms) along the GB are almost similar. While the atoms colored with green correspond to FCC structures, the red atoms correspond to HCP structures forming the stacking faults. Comparing these two initial snapshots, one can see the effect of Ta in attaining grain stability of polycrystalline Cu even at higher temperatures. At 300 K, the deformation process was dominated by dislocation slip but less than pure Cu. Dislocations emitted from the GBs interacted with the Ta nanoclusters, and become pinned at various sites, thereby reducing their mean free path of propagation. However, at 1000 K, deformation
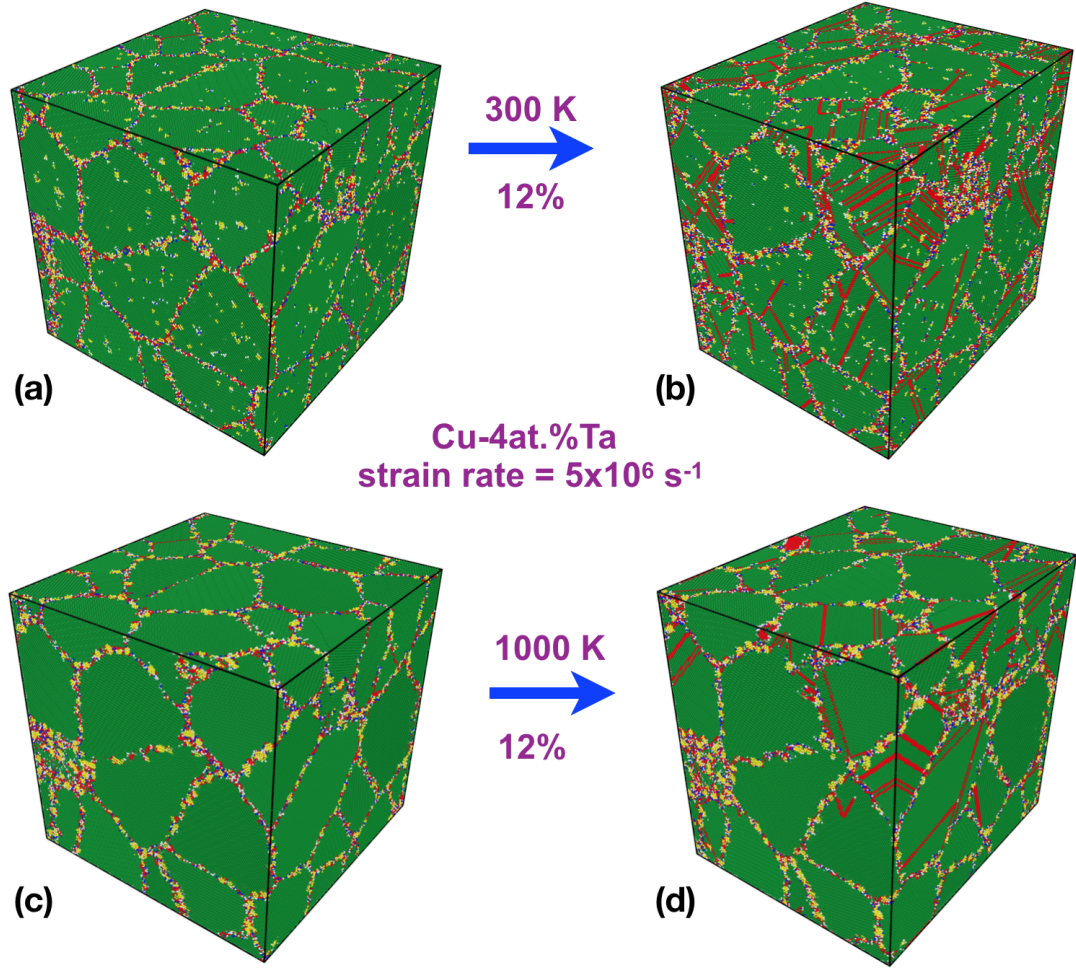
Figure 7.6: Microstructural evolution of Cu-4at.%Ta alloy during deformation with the 5×10^6 s^{-1} strain rate at (a) 300 K and (b) 1000 K. FCC, HCP, and Ta atoms are colored in green, red, and yellow color respectively.

was dominated by GB activities such as GB diffusion, sliding, and grain rotation. The presence of Ta nanoclusters slowed down and eventually blocked grain boundary motion and grain rotation. Thus, the amount of sliding and grain rotation in Cu-4at.%Ta alloy was less extensive than pure Cu.

To observe the GB processes, a network of mutually perpendicular marker lines was created by coloring groups of atoms and tracing their motion during the simulations. As shown in Fig. 7.7, after a 12% deformation, many of the marker lines are broken into

(a)   Cu   **(b)   Cu-4at.%Ta**
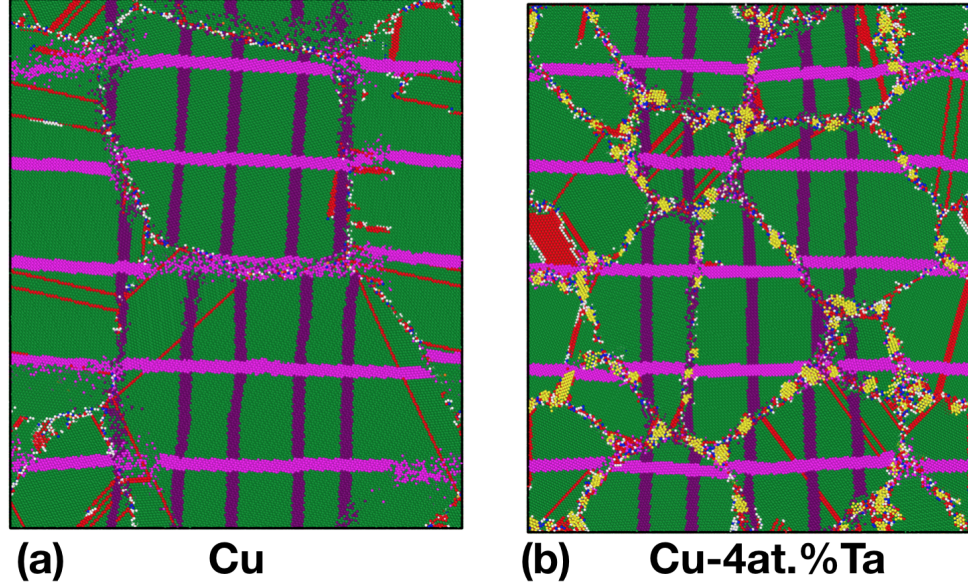
Figure 7.7: Typical projections of polycrystalline Cu (a) and Cu-4at.%Ta alloy (b) at 1000 K after 12% deformation with the 5×10^6 s^{-1} strain rate. The compression axis is horizontal. The horizontal (pink) and vertical (purple) stripes represent two sets of marker lines. FCC, HCP, and Ta atoms are colored in green, red, and yellow color respectively.

segments at intersections with GBs, which is a signature of GB sliding. Furthermore, some of the segments are slightly tilted relative to the initial strictly horizontal or strictly vertical alignments. This tilting is an indicator of grain rotation. The GB sliding and grain rotation are kinematically coupled to each other [37,92,93]. Fig. 7.7 also reveals some grain growth in Cu during the deformation process and perhaps slightly more extensive GB sliding and grain rotation than in the alloy. This is additional evidence that Ta clusters are more effective in attaining grain stability by reducing grain boundary migration.

7.4   Conclusion

The strain-rate sensitivity behavior has been studied by atomistic simulation in Cu-4at.%Ta alloy over a wide range of compression rates between 5×10^6 and 10^9 s^{-1} at the temperature 300 K and 1000 K, respectively. The flow stress decreased with an increase in temperature and slightly increased with the strain rate but always remained higher than polycrystalline

Cu for that particular temperature. Cu-4at.%Ta alloy exhibited smaller strain rate sensitivity in comparison with the pure Cu at both temperatures. The computed strain rate sensitivity values of Cu-4at.%Ta alloy were m=0.029±0.004 at 300 K and m=0.075±0.004 at 1000K. These numbers agree reasonably well with the experimental numbers. Thus, the strain rate sensitivity of Cu-Ta alloys is not substantial, even at higher temperatures where pure nanomaterials become unstable and undergo rapid grain growth. The mechanisms driving this unexpected trend are related to interactions of GBs with Ta nanoclusters leading to a reduction or elimination of grain boundary sliding and grain rotation. The Ta clusters also inhibit deformation-induced grain growth and suppress the operation of dislocation sources inside the grains leading to high strength and structural stability.

Chapter 8: Atomistic study of tensile creep behavior in Cu-Ta alloys

8.1   Introduction

Mechanical properties of nanocrystalline materials get modified when exposed longer time to the mechanical load below the yield strength at high homologous temperature. Thus, materials exhibiting superior resistance to time-dependent plastic deformation called creep needs to be designed for the structural applications at high temperature. Materials possess such behavior when deformation mechanisms such as dislocation slip, grain boundary sliding, rotation, and diffusion are limited. The current design includes the use of single-crystal alloys for high temperature creep performance. Ni-based single superalloys lie at the forefront in having superior tensile creep behavior (creep rate of about 10^{-8} s^{-1}) with high-temperature strength even up to temperatures as high as 90% of its melting temperature. Nanocrystalline materials, with a mean grain size less than 100 nanometers, have never been considered for high-temperature creep applications due to their lack of thermal and microstructural stability.

Recently, based on the mechanical alloying technique, a new class of nanocrystalline alloys with two immiscible components, Cu and Ta, have been developed that show remarkable properties under various thermal and mechanical loadings. Nanocrystalline Cu-10at.%Ta alloy has been shown to possess compression creep rates comparable to the Ni-based superalloys with a dislocation based creep mechanism. Previous atomistic simulations have demonstrated that the reduction of GB motion by the Ta clusters lying along the GBs and lattice gives extraordinary strength, stability, and low strain rate sensitivity index. The current simulations deal in understanding the creep mechanisms of Cu-Ta alloy in the temperature interval 850-1100 K by adding Ta up to 4% under tensile elongation with applied

stress in the interval 100-300 MPa.

8.2 Methodology

Atomistic simulations utilized the angular dependent potential [32] for the Cu-Ta system which reproduced results that were in agreement with the experimental data and first-principles calculations. The simulations employed parallel MC code ParaGrandMC [132] for generating varying compositions of Cu-Ta alloys using the composition-controlled MC algorithm [91, 108]. This algorithm brings the system to thermodynamic equilibrium at a given temperature and average chemical composition under zero-stress conditions. The trial moves of the MC process include small random displacements of randomly selected atoms in a random direction and a random re-assignment of the chemical species of the atoms to either Cu or Ta. MD simulations were performed using the Large-scale Atomic/Molecular Massively Parallel Simulator (LAMMPS) [107] code.

A polycrystalline copper sample composed of 32 grains with a mean grain size of 12.6 nm was constructed using the Voronoi tesselation method. The sample contained about 5.4 million atoms with an approximate dimension of 40 nm×40 nm×40 nm and periodic boundary conditions in all three dimensions. The GBs structures were optimized by a procedure described elsewhere [32,38,94]. In the MC simulations, Ta atoms precipitated in the form of nanoclusters predominantly at GBs and triple junctions (TJs).

To investigate tensile creep response, MD simulations were performed applying constant stress along one cartesian direction with zero pressure in lateral directions. The sample was subject to different uniaxial stresses ranging from 100 Mpa to 300 MPa in the temperatures range 850 K to 1100 K. Snapshots of the simulation block were saved at regular interval of time and were observed using visualization software OVITO [110]. The atoms in the grain were identified and tracked through the parallel MPI code written for evaluating the orientation matrix. The orientation matrix was determined through the orientation of the unit cell structure of a sample coordinate system, which can be calculated with

the alignment of direction vectors of its neighboring atoms [103]. Four different chemical compositions ranging from pure Cu to Cu-4at.%Ta alloy were tested in order to understand the creep deformation mechanisms.

8.3 Results

8.3.1 Creep behavior

Figure 8.1 shows strain evolution with time for the polycrystalline Cu-4at.%Ta alloy under isothermal (T=1100 K) and isobaric (σ_{xx}=300 MPa) creep deformation. All curves consist of a short primary creep regime characterized by a decrease in deformation rate with time and a secondary creep regime defined by a steady-state deformation rate. The deformation
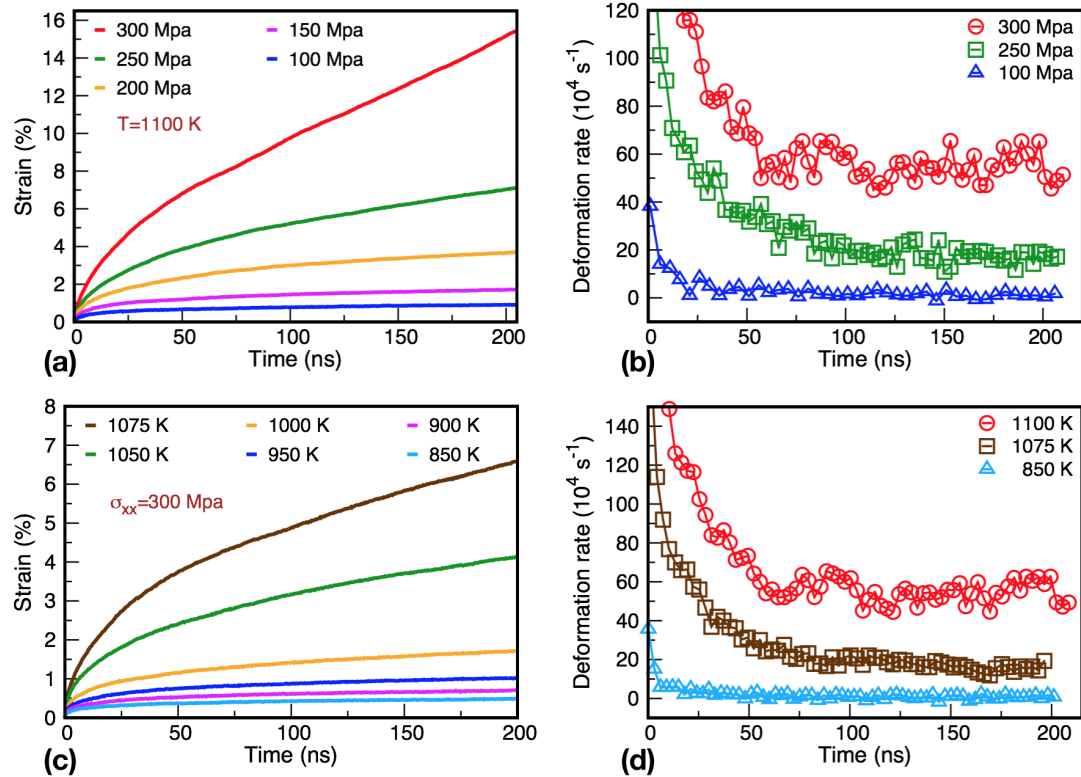
Figure 8.1: Tensile creep curves of Cu-4at.%Ta alloy. Creep strain versus time curves for (a) isothermal (1100 K) and (c) isobaric (300 MPa) creep deformation. Deformation rate versus time curves for (b) isothermal and (d) isobaric creep deformation.

rate is indicated by the change in slope on strain-time curves. These curves shows only the first two stages of creep deformation as the simulations were focussed only on understanding the primary and the secondary creep behavior. As expected, the rate of deformation increased with temperature and applied stress.

Table 8.1: Yield stress (YS) as a function of temperature calculated with tensile elongation of strain rate $1\times10^7\text{s}^{-1}$ in Cu-4at.%Ta alloy

Temperature (K)	Homologous temperature	Yield stress (MPa)	Applied stress
850	0.64	858.09	0.35YS (300 MPa)
900	0.68	788.46	0.38YS (300 MPa)
950	0.72	639.25	0.47YS (300 MPa)
1000	0.75	554.68	0.54YS (300 MPa)
1050	0.79	440.10	0.68YS (300 MPa)
1075	0.81	375.66	0.80YS (300 MPa)
1100	0.83	337.53	0.30-0.89YS (100-300 MPa)

Table 8.1 shows the simulation temperatures and the applied stresses in terms of homologous temperature and yield stress, respectively. The yield stress was calculated with the tensile elongation of strain rate 1×10^7 s^{-1}. The observed steady creep deformation rates at $(0.64\text{T}_m,0.35\text{YS})$, $(0.83\text{T}_m,0.3\text{YS})$ and $(0.83\text{T}_m,0.89\text{YS})$ were $3.86\pm7.31\times10^3$ s^{-1}, $7.86\pm9.91\times10^3$ s^{-1} and $5.70\pm0.43\times10^5$ s^{-1}, respectively. Although these values are much higher than experimentally observed creep deformation rate 10^{-6} s^{-1} across Cu-10at.%Ta alloy [39], the simulated strain-time curves for Cu-4at.%Ta alloy look qualitatively similar without strain hardening and sustains thermal and mechanical stability.

As the deformation rate $\dot{\epsilon}$ follows a power-law relationship with stress σ, which may be expressed as $\dot{\epsilon} \propto \sigma^n$, the stress exponent n=$\partial(\ln\dot{\epsilon})/\partial(\ln\sigma)$ was computed from the slope of the $\ln\sigma$ vs. $\ln\dot{\epsilon}$ plot at 1100 K (Fig. 8.2a). The value of n was obtained as 3.78±0.44. In pure metals, the stress exponent is an important parameter as its value indicates whether the creep mechanism is governed by diffusion (n<1) or dislocation (n∼3-8). For pure Cu, it has been shown through MD simulations that the value of n changes with different applied
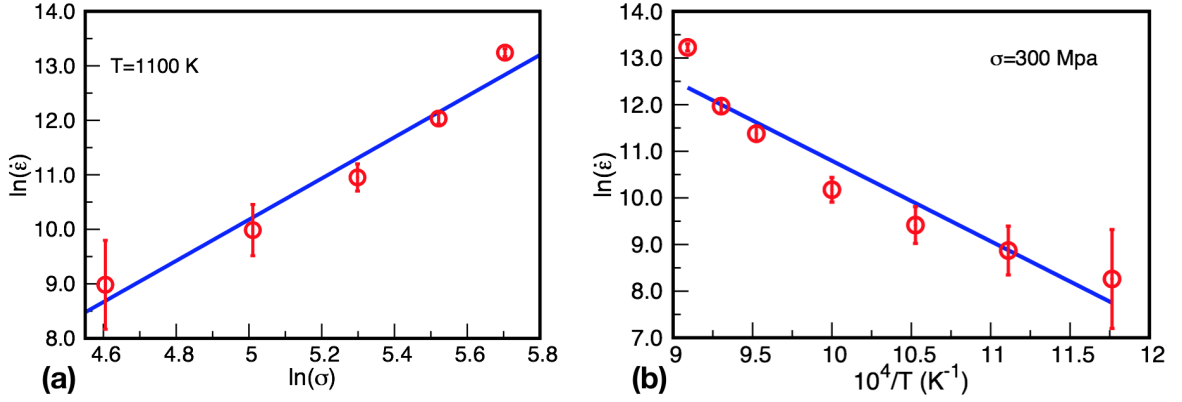
Figure 8.2: (a) Log-log plot of steady-state deformation rate versus applied stress at 1100 K. (b) Arrhenius plot of steady-state deformation rate versus $10^4/T$ for 300 MPa.

stresses and the magnitudes are n ≈ 1 for 50 to 250 MPa, 1<n<2 for 250 to 850 MPa, and n > 4 MPa above 800 MPa [153]. These values were reported for 960 K with a grain size of about 10.8 nm, which is pretty similar to the grain size used in this simulation. Thus, the simulations reveal a higher value of n for Cu-Ta alloys compared to pure Cu for the same magnitude of stress.

Figure 8.2b shows an Arrhenius plot of the steady-state deformation rate observed at various temperatures. The computed activation energy was 1.48±0.21 ev. To have a further insight into the activation energy, the primary creep curves of isobaric deformation were best fitted with the Andrade's equation of the form $\dot{\epsilon}=\beta t^m$. Andrade reported m=1/3 for the creep deformation of soft metals at constant temperature and stress. In our case, the results for m varies between 0.29 to 0.56 with 300 MPa, as shown in Fig. 8.3. At low temperatures 850 to 950 K, m is close to 1/3 but varies significantly at higher temperatures reaching 0.57 at 1100 K. It has been reported in literature that m could exhibit large scattering with a value ranging between 0.25 to 0.45 [154]. Thus, the scattering in the observed values of m is recognizable. Further, assuming the Arrhenius behavior on $\beta=\beta_0\exp(-U/kT)$, the activation energy U for the primary creep regime was calculated, as shown in Fig. 8.3, and the corresponding activation energy was 0.53±0.05 ev. Andrade's law predicts the

activation energy of the primary creep regime as 1/3 of the activation energy of steady-state. In our case, the value was obtained as 0.36. This correlation between two activation energy calculated from two different regimes lends additional confidence to the simulation methodology used in this work.
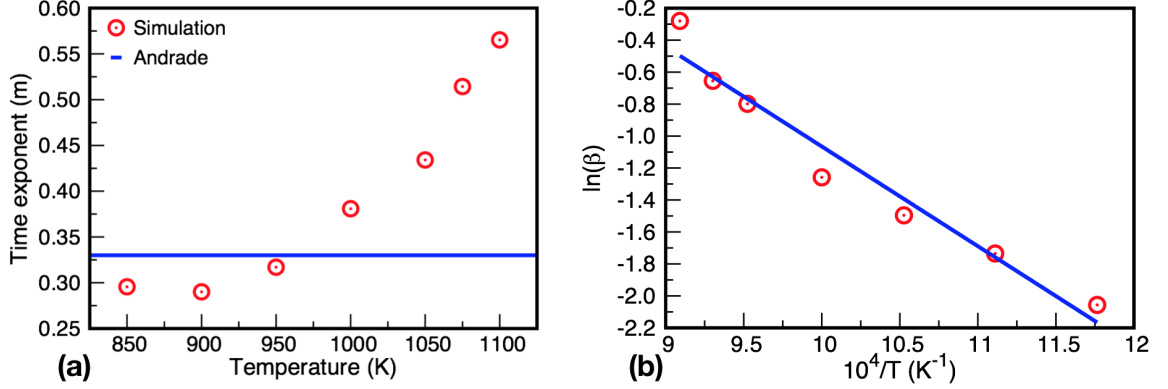
Figure 8.3: (a) Time exponent as a function of temperature. (b) Arrhenius plot of Andrade's coefficient versus $10^4/T$ for 300 MPa.

8.3.2 Mircrostructural evolution

Atomistic simulations were run using MC and MD simulations for four different chemical compositions, ranging from NC pure Cu to NC Cu with 0.5at.%, 2at.% and 4at.% Ta respectively, in order to understand the creep deformation mechanisms. In Cu-Ta alloys, Ta atoms were found to segregate into nanoclusters in the GBs, triple junctions (TJs), as well as in the lattice similar to that observed from as-received TEM characterization. Figure 8.4 shows the microstructural evolution of pure Cu under creep loading for 14 ns with applied stress of 300 MPa at 1100 K. Pure Cu displayed significant grain growth and grain rotation along with twinning, dislocation emission, and propagation. The rate of deformation decreased rapidly in pure Cu with the onset of grain growth and shrinkage.

As the Ta concentration was increased, Ta clusters segregated along the boundary, and
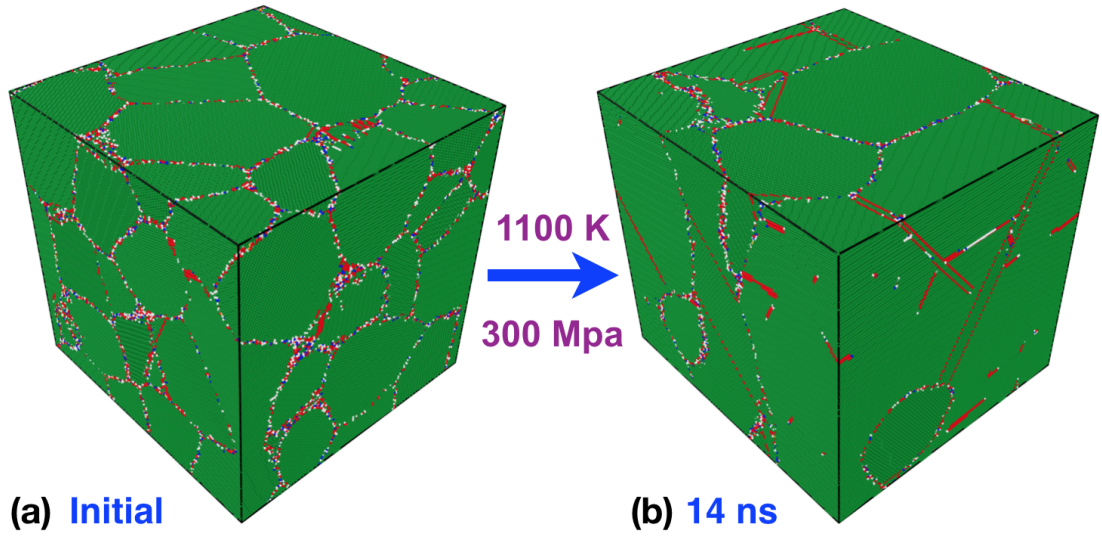
Figure 8.4: Creep deformation of pure Cu with 300 MPa at 1100 K. Initial (a) and (b) final (after 14 ns) microstructure shows rapid grain growth with dislocation slip, rotation, twinning, and grain shrinkage. FCC and HCP atoms are colored in green and red, respectively.
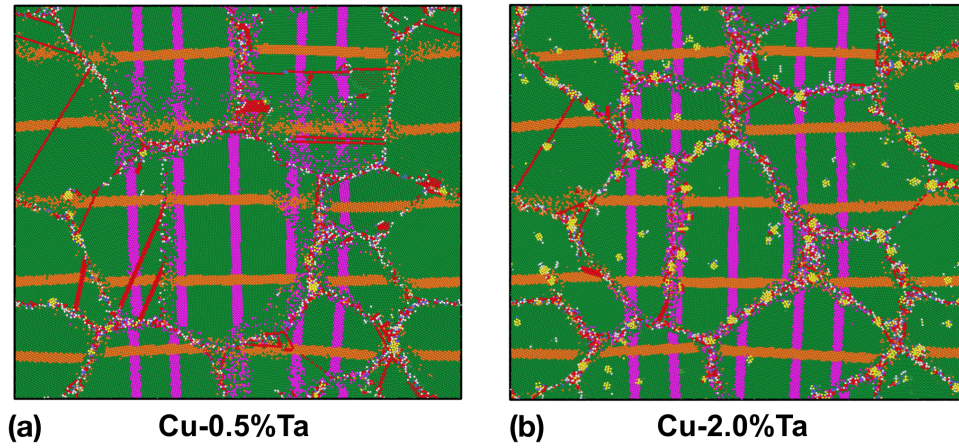
Figure 8.5: Projections of (a) Cu-0.5at.%Ta and (b) Cu-2.0at.%Ta alloys after 28 ns and 40 ns respectively with 300 MPa at 1100 K. The smearing of mutually perpendicular lines in the interior of the grain indicates the GB migration causing grain growth. The broken and shifted line segments indicates GB sliding. The tensile axis is horizontal. FCC, HCP, and Ta atoms are colored in green, red, and yellow color respectively.

the GB migration rate was reduced. Furthermore, the GB sliding became prominent. However, Cu-Ta alloys with compositions up to 2at.%Ta displayed grain growth, grain rotation and sliding, twinning, dislocation emission, and propagation. Figure 8.5 shows the two-dimensional slices of Cu-0.5%Ta and Cu-2.0%Ta alloys after 28 ns and 40 ns, respectively. Some grains that can be observed at 2at.%Ta alloy are completely lost in 0.5at.%Ta alloy. The smearing of mutually perpendicular lines in the interior of the grain indicates the GB migration causing grain growth. In addition, the broken and shifted line segments intersecting with the GBs is a signature of GB sliding. These lines were created by coloring groups of atoms in the initial simulation block and were tracked during the simulations.

When Ta concentration was 4at.%, Cu-Ta alloy displayed outstanding microstructural stability (Fig. 8.6). In this case, the GB migration was found to be impeded and thus resulting in preservation of the total number of grains within the simulation block. Instead, the simulation block was elongated along the tensile direction and compressed laterally.
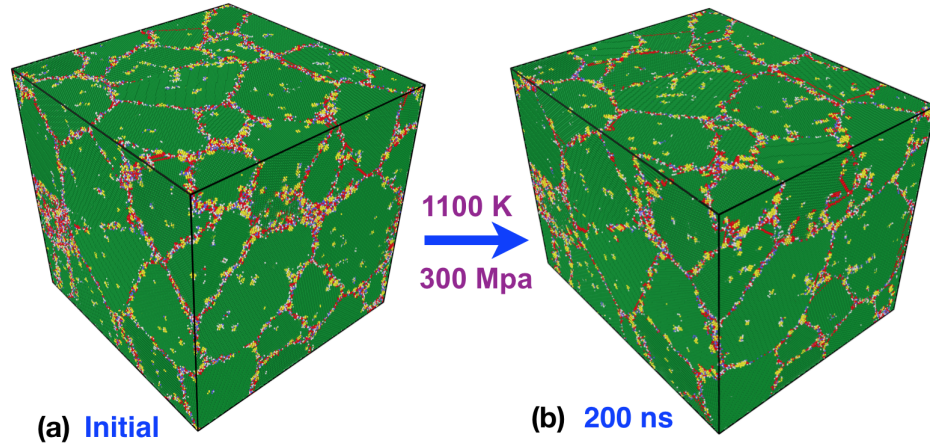
Figure 8.6: Creep deformation of Cu-4at.% alloy with 300 MPa at 1100 K. (a) Initial and (b) after 200 ns. FCC, HCP atoms, and Ta clusters are colored in green, red, and yellow color respectively.

Fig. 8.7 displays the evolution of the network of mutually perpendicular lines in Cu-4.0%Ta alloy after 200 ns. Comparing the initial and final snapshots, one can find that the
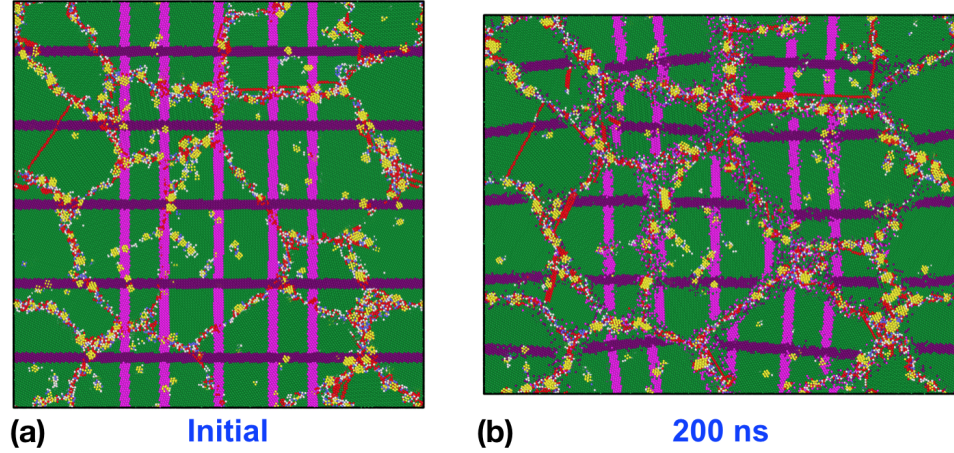
Figure 8.7: Projection of Cu-4at.%Ta alloy. (a) Initial and (b) final after tensile creep deformation with 300 MPa at 1100 K. The tensile creep direction is horizontal. The horizontal (purple) and vertical (pink) stripes represent two sets of mutually perpendicular marker lines. The broken line segments indicates GBs sliding and dispersion along the GBs implies diffusion. FCC, HCP, and Ta atoms are colored in green, red, and yellow color respectively.

lines intersecting with the GBs are segmented; a signature of GB sliding and the portion of lines lying along the GBs are dispersed; a signature of GB diffusion. However, there is no scattering of lines in the grain interior, as observed in the lower compositions indicating an absence of GB migration. We did not observe considerable dislocation activity within the simulation time, although some twin planes having tiny dimensions were formed near the GBs. Some partial dislocations emitted from the GBs could not extend further inside the grain and lost absorbing back into the GBs. The interior Ta clusters were also observed to hinder such extension. The slip vector analysis inferred the maximum activity of atoms lying only along the GB regions. Figure 8.8 shows the slip vector analysis of the snapshots after 200 ns with 300 MPa at 900 K and 1100 K, respectively. Had there been a dislocation slip, a line passing through the grain interior would have been observed, but such lines were not discernible. This implies GB diffusion as the major mechanism of creep deformation in Cu-4.0%Ta alloy.

If the creep deformation is indeed controlled by GB diffusion, atoms should diffuse from the boundaries lying parallel to the tensile direction to normal boundaries for the elongation
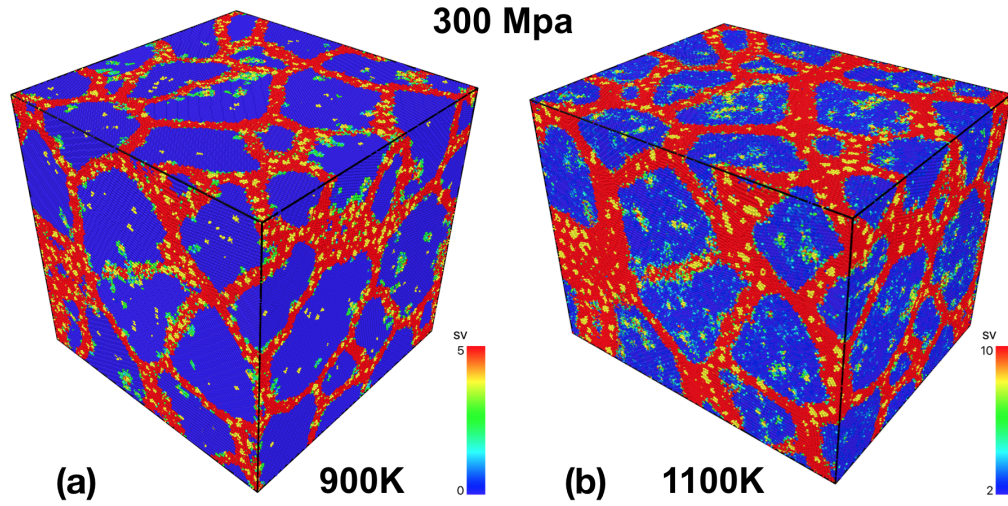
Figure 8.8: Slip vector analysis of Cu-4at.%Ta alloy after tensile creep deformation with 300 MPa at (a) 900 K and (b) 1100 K.
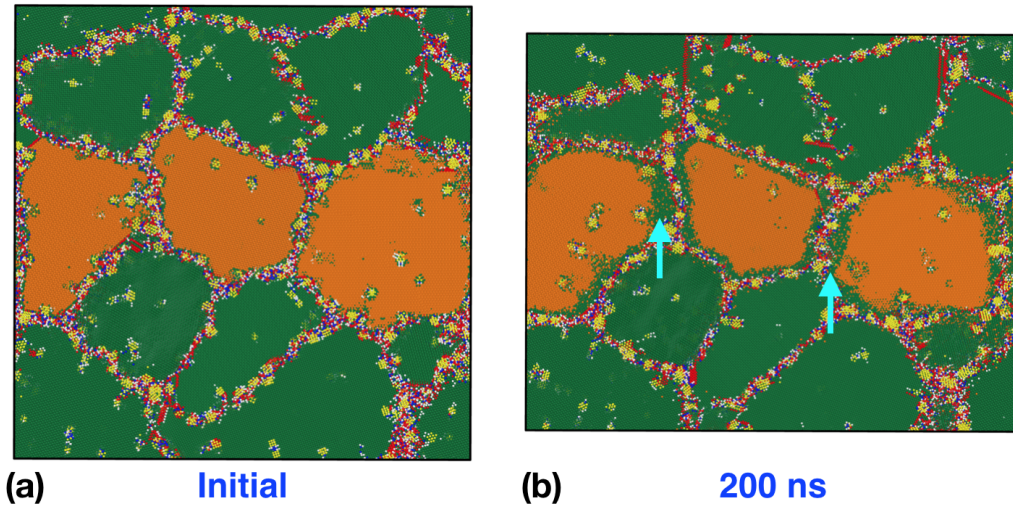
Figure 8.9: Two-dimensional slices of three-dimensional Cu-4at.%Ta alloy (a) before and (b) after tensile creep deformation with 300 MPa at 1100 K. Interior grain atoms are colored orange in both images. Addition of new layers through diffusion mechanism along tensile direction are indicated by cyan arrows. FCC, HCP, and Ta atoms are colored in green, red, and yellow color respectively.

of the block. This is because an applied uniaxial tensile stress creates high hydrostatic stress at normal GBs and then generates excess vacancies, which diffuses to parallel boundaries.

As such, new layers of FCC atoms should be added in the grain along the tensile direction, and lateral directions should constrict retaining old atoms intact with the boundary. This was indeed observed when the grain atoms from the initial snapshot were tracked during the simulation. Figure 8.9 shows two-dimensional slices of the three-dimensional simulation structure before and after creep testing with 300 MPa at 1100 K for 200 ns. The atoms in the grain interior were colored orange for visualization purposes. In the post- deformation slice, Fig 8.9b, new layers of FCC atoms are added along the tensile direction as indicated by cyan arrows.
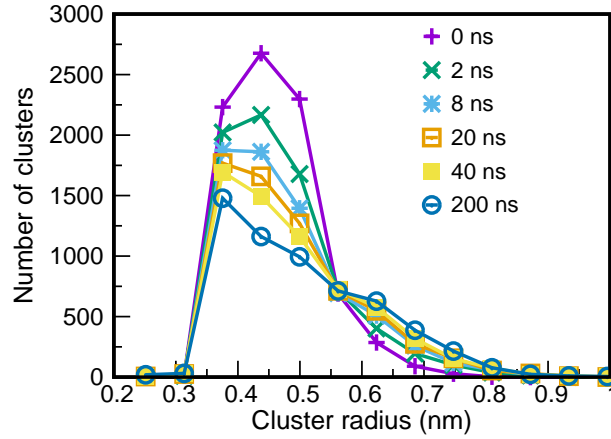
Figure 8.10: Clusters size distribution during creep deformation with 100 Mpa at 1100 K. The size distribution includes all clusters lying in the GBs as well as in the lattice.

While analyzing the atoms diffused along the GBs, Cu atoms were observed to diffuse significantly along the GBs. However, the slow diffusion rate of Ta did not allow Ta atoms in the nanoclusters to diffuse along the GBs. Instead, neighboring Ta clusters lying along the GBs were coarsened together to form larger Ta clusters with the GB diffusion of Cu atoms. This phenomena shifted the size distribution of Ta clusters towards the larger size, as shown in Fig. 8.10. The coarsening process was very rapid in the primary regime of creep deformation and became slower in the secondary regime of creep deformation. Although

the coarsening process merges Ta clusters into larger clusters, the size of clusters remained below one nanometer.

8.4   Conclusion

Atomistic simulations confirmed that Cu-4at.%Ta alloy exhibits steady-state creep behavior without strain hardening and sustains thermal and mechanical stability. The creep exponent was computed as 3.78 ± 0.44. This value indicates the dislocation based creep mechanism in pure nanomaterials. However, the case here was different, as this is an alloy. We did not observe considerable dislocation activity within the simulation time, although some twin planes having tiny dimensions were formed near the GBs. The Ta clusters suppressed the operation of dislocation sources inside the grains and GB activities, such as GB sliding and grain rotation. Indeed, the creep mechanism was governed by GB diffusion. With the GB diffusion of Cu atoms, new layers of atoms were added in the grain along the tensile direction, while dissolving atomic layers in the lateral directions. During the process of Cu diffusion, Ta clusters lying along the GBs were coarsened together to form larger Ta clusters. Thus, the prediction of the creep mechanism on the basis of stress exponent in pure nanomaterials misses in Cu-Ta alloys and may require revision for the case of alloys.

Chapter 9: Summary

Using atomistic simulations, we have systematically studied the interaction of Ta clusters with individual GBs to have a better understanding of the mechanism of thermal stability of Cu-Ta alloys. With the stress-driven and capillary driven GB motions, we have observed that the retardation of GB motion by Ta clusters is consistent with the Zener pinning model both qualitatively and quantitatively. Thus, Zener pinning is the primary mechanism of the extraordinary stability of nanocrystalline Cu-Ta alloys. Moreover, the effect of solute drags at GBs in a random or nonequilibrium solution is not as strong as cluster pinning. However, a moving GB in the random solution precipitates a set of Ta clusters due to short circuit diffusion of Ta along the GB core. The GB redistributes diffused Ta atoms in its core in a non-uniform manner causing the formation of tiny clusters. These clusters pin the GB until the stress builds up, reaching the unpinning value. As the GB unpins, it moves ahead and again creates a new set of clusters that pin the boundary in the new position. Thus, the GB motion in the metastable solid solution exhibits a dynamic instability with alternating periods of GB arrest and motion.

The atomistic simulations confirmed that small Ta clusters have FCC structure predominantly and remain at least partially coherent with the Cu matrix. As the cluster size increases, it becomes incoherent and emits misfit dislocations in the matrix. Also, the lattice misfit between the Ta clusters and the matrix tends to decrease at higher temperatures, promoting better coherency.

The MC and MD simulations have demonstrated redistributions of Cu and Ta atoms and coarsening of neighboring Ta atoms in an amorphous solution as the main mechanism for the formation of single/double core-shell nanostructures. When Cu atoms diffuse within the amorphous region or into the matrix, Ta atoms tend to aggregate and form small isolated clusters. During the coarsening process, Cu atoms are also trapped within the Ta clusters

forming a core-shell structure that reduce the energy.

Cu-4at.%Ta alloy exhibited smaller strain rate sensitivity even at a higher temperature where the Cu polycrystal demonstrated rapid grain growth. The mechanisms driving this unexpected trend are related to the interactions of GBs with Ta nanoclusters leading to a reduction or elimination of grain boundary sliding and rotation. We observed that creep in Cu-Ta alloy is governed by atomic diffusion with the stress exponent 3.78 ± 0.44. While this value indicates dislocation based creep mechanism in pure nanomaterials, the case is different in Cu-4at.%Ta alloy where Ta clusters suppressed the operation of dislocation sources inside the grains and GB activities, such as GB sliding and grain rotation. With the GB diffusion of Cu atoms, new layers of atoms were added in the grain along the tensile direction, while dissolving atomic layers in the lateral directions. During the process of Cu diffusion, Ta clusters lying along the GBs were coarsened together to form larger Ta clusters.

Bibliography

Bibliography

[1] H. Gleiter, "Nanocrystalline materials," *Progress in Materials Science*, vol. 33, no. 4, pp. 223–315, 1989. [Online]. Available: http://www.sciencedirect.com/science/article/pii/0079642589900017

[2] K. S. Kumar, H. Van Swygenhoven, and S. Suresh, "Mechanical behavior of nanocrystalline metals and alloys11the golden jubilee issue—selected topics in materials science and engineering: Past, present and future, edited by s. suresh," *Acta Materialia*, vol. 51, no. 19, pp. 5743–5774, 2003. [Online]. Available: http://www.sciencedirect.com/science/article/pii/S1359645403005135

[3] J. H. Driver, "Stability of nanostructured metals and alloys," *Scripta Materialia*, vol. 51, no. 8, pp. 819–823, 2004. [Online]. Available: http://www.sciencedirect.com/science/article/pii/S1359646204002830

[4] M. A. Meyers, A. Mishra, and D. J. Benson, "Mechanical properties of nanocrystalline materials," *Progress in Materials Science*, vol. 51, no. 4, pp. 427–556, 2006. [Online]. Available: http://www.sciencedirect.com/science/article/pii/S0079642505000447

[5] R. A. Andrievski, "Review of thermal stability of nanomaterials," *Journal of Materials Science*, vol. 49, no. 4, pp. 1449–1460, 2014. [Online]. Available: http://dx.doi.org/10.1007/s10853-013-7836-1

[6] M. Dao, L. Lu, R. J. Asaro, J. T. M. De Hosson, and E. Ma, "Toward a quantitative understanding of mechanical behavior of nanocrystalline metals," *Acta Materialia*, vol. 55, no. 12, pp. 4041–4065, 2007. [Online]. Available: http://www.sciencedirect.com/science/article/pii/S1359645407001073

[7] L. Lu, Y. Shen, X. Chen, L. Qian, and K. Lu, "Ultrahigh strength and high electrical conductivity in copper," *Science*, vol. 304, no. 5669, pp. 422–426, 2004. [Online]. Available: https://science.sciencemag.org/content/304/5669/422

[8] R. Ferrando, J. Jellinek, and R. L. Johnston, "Nanoalloys: From theory to applications of alloy clusters and nanoparticles," *Chemical Reviews*, vol. 108, no. 3, pp. 845–910, 03 2008. [Online]. Available: https://doi.org/10.1021/cr040090g

[9] Z. N. Farhat, Y. Ding, D. O. Northwood, and A. T. Alpas, "Effect of grain size on friction and wear of nanocrystalline aluminum," *Materials Science and Engineering: A*, vol. 206, no. 2, pp. 302–313, 1996. [Online]. Available: http://www.sciencedirect.com/science/article/pii/0921509395100164

[10] D. H. Jeong, F. Gonzalez, G. Palumbo, K. T. Aust, and U. Erb, "The effect of grain size on the wear properties of electrodeposited nanocrystalline nickel coatings," *Scripta Materialia*, vol. 44, no. 3, pp. 493–499, 2001. [Online]. Available: http://www.sciencedirect.com/science/article/pii/S1359646200006254

[11] T. J. Rupert and C. A. Schuh, "Sliding wear of nanocrystalline ni–w: Structural evolution and the apparent breakdown of archard scaling," *Acta Materialia*, vol. 58, no. 12, pp. 4137–4148, 2010. [Online]. Available: http://www.sciencedirect.com/science/article/pii/S1359645410002119

[12] C. C. Koch, R. O. Scattergood, K. A. Darling, and J. E. Semones, "Stabilization of nanocrystalline grain sizes by solute additions," *Journal of Materials Science*, vol. 43, no. 23, pp. 7264–7272, 2008. [Online]. Available: http://dx.doi.org/10.1007/s10853-008-2870-0

[13] J. R. Trelewicz and C. A. Schuh, "Grain boundary segregation and thermodynamically stable binary nanocrystalline alloys," *Physical Review B*, vol. 79, no. 9, pp. 094 112–, 03 2009. [Online]. Available: http://link.aps.org/doi/10.1103/PhysRevB.79.094112

[14] T. Chookajorn, H. A. Murdoch, and C. A. Schuh, "Design of stable nanocrystalline alloys," *Science*, vol. 337, no. 6097, p. 951, 08 2012. [Online]. Available: http://science.sciencemag.org/content/337/6097/951.abstract

[15] T. Chookajorn and C. A. Schuh, "Thermodynamics of stable nanocrystalline alloys: A monte carlo analysis," *Physical Review B*, vol. 89, no. 6, pp. 064 102–, 02 2014. [Online]. Available: http://link.aps.org/doi/10.1103/PhysRevB.89.064102

[16] K. A. Darling, M. A. Tschopp, B. K. VanLeeuwen, M. A. Atwater, and Z. K. Liu, "Mitigating grain growth in binary nanocrystalline alloys through solute selection based on thermodynamic stability maps," *Computational Materials Science*, vol. 84, pp. 255–266, 3 2014. [Online]. Available: http://www.sciencedirect.com/science/article/pii/S0927025613006356

[17] J. W. Cahn, "The impurity-drag effect in grain boundary motion," *Acta Metallurgica*, vol. 10, no. 9, pp. 789–798, 1962. [Online]. Available: http://www.sciencedirect.com/science/article/pii/0001616062900925

[18] M. I. Mendelev and D. J. Srolovitz, "Impurity effects on grain boundary migration," *Modelling and Simulation in Materials Science and Engineering*, vol. 10, no. 6, p. R79, 2002. [Online]. Available: http://stacks.iop.org/0965-0393/10/i=6/a=201

[19] I. Toda-Caraballo, C. Capdevila, G. Pimentel, and C. G. De Andrés, "Drag effects on grain growth dynamics," *Computational Materials Science*, vol. 68, pp. 95–106, 2 2013. [Online]. Available: http://www.sciencedirect.com/science/article/pii/S0927025612006015

[20] F. Abdeljawad and S. M. Foiles, "Stabilization of nanocrystalline alloys via grain boundary segregation: A diffuse interface model," *Acta Materialia*, vol. 101, pp. 159–171, 12 2015. [Online]. Available: http://www.sciencedirect.com/science/article/pii/S1359645415005418

[21] Y. Mishin, "Solute drag and dynamic phase transformations in moving grain boundaries," *Acta Materialia*, vol. 179, pp. 383–395, 2019. [Online]. Available: http://www.sciencedirect.com/science/article/pii/S135964541930566X

[22] E. Nes, N. Ryum, and O. Hunderi, "On the zener drag," *Acta Metallurgica*, vol. 33, no. 1, pp. 11–22, 1985. [Online]. Available: http://www.sciencedirect.com/science/article/pii/0001616085902147

[23] W. B. Li and K. E. Easterling, "The influence of particle shape on zener drag," *Acta Metallurgica et Materialia*, vol. 38, no. 6, pp. 1045–1052, 1990. [Online]. Available: http://www.sciencedirect.com/science/article/pii/095671519090177I

[24] P. A. Manohar, M. Ferry, and T. Chandra, "Five decades of the zener equation," *ISIJ International*, vol. 38, no. 9, pp. 913–924, 1998. [Online]. Available: https://doi.org/10.2355/isijinternational.38.913

[25] B. Huang, R. J. Perez, and E. J. Lavernia, "Grain growth of nanocrystalline fe–al alloys produced by cryomilling in liquid argon and nitrogen," *Materials Science and Engineering: A*, vol. 255, no. 1, pp. 124–132, 1998. [Online]. Available: http://www.sciencedirect.com/science/article/pii/S0921509398007655

[26] K. Darling, B. VanLeeuwen, J. Semones, C. Koch, R. Scattergood, L. Kecskes, and S. Mathaudhu, "Stabilized nanocrystalline iron-based alloys: Guiding efforts in alloy selection," *Materials Science and Engineering: A*, vol. 528, no. 13, pp. 4365 – 4371, 2011. [Online]. Available: http://www.sciencedirect.com/science/article/pii/S0921509311002553

[27] A. Khalajhedayati and T. J. Rupert, "High-temperature stability and grain boundary complexion formation in a nanocrystalline cu-zr alloy," *JOM*, vol. 67, no. 12, pp. 2788–2801, 2015. [Online]. Available: https://doi.org/10.1007/s11837-015-1644-9

[28] J. T. Zhao, J. Y. Zhang, Z. Q. Hou, K. Wu, X. B. Feng, G. Liu, and J. Sun, "The w alloying effect on thermal stability and hardening of nanostructured cu–w alloyed thin films," *Nanotechnology*, vol. 29, no. 19, p. 195705, 2018. [Online]. Available: http://dx.doi.org/10.1088/1361-6528/aab19a

[29] T. Frolov, K. A. Darling, L. J. Kecskes, and Y. Mishin, "Stabilization and strengthening of nanocrystalline copper by alloying with tantalum," *Acta Materialia*, vol. 60, no. 5, pp. 2158–2168, 3 2012. [Online]. Available: http://www.sciencedirect.com/science/article/pii/S1359645412000468

[30] K. A. Darling, A. J. Roberts, Y. Mishin, S. N. Mathaudhu, and L. J. Kecskes, "Grain size stabilization of nanocrystalline copper at high temperatures by alloying with tantalum," *Journal of Alloys and Compounds*, vol. 573, pp. 142–150, 10 2013. [Online]. Available: http://www.sciencedirect.com/science/article/pii/S0925838813007081

[31] K. Darling, M. Tschopp, R. Guduru, W. Yin, Q. Wei, and L. Kecskes, "Microstructure and mechanical properties of bulk nanostructured cu–ta alloys consolidated by equal channel angular extrusion," *Acta Materialia*, vol. 76, pp. 168 – 185, 2014. [Online]. Available: http://www.sciencedirect.com/science/article/pii/S1359645414003371

[32] G. P. Purja Pun, K. A. Darling, L. J. Kecskes, and Y. Mishin, "Angular-dependent interatomic potential for the cu–ta system and its application to structural stability of nano-crystalline alloys," *Acta Materialia*, vol. 100, pp. 377–391, 11 2015. [Online]. Available: http://www.sciencedirect.com/science/article/pii/S1359645415006291

[33] T. Rojhirunsakool, K. A. Darling, M. A. Tschopp, G. P. Purja Pun, Y. Mishin, R. Banerjee, and L. J. Kecskes, "Structure and thermal decomposition of a nanocrystalline mechanically alloyed supersaturated cu–ta solid solution," *MRS Communications*, vol. 5, no. 2, pp. 333–339, 2015. [Online]. Available: https://doi.org/10.1557/mrc.2015.34

[34] B. C. Hornbuckle, T. Rojhirunsakool, M. Rajagopalan, T. Alam, G. P. Purja Pun, R. Banerjee, K. N. Solanki, Y. Mishin, L. J. Kecskes, and K. A. Darling, "Effect of ta solute concentration on the microstructural evolution in immiscible cu-ta alloys," *JOM*, vol. 67, no. 12, pp. 2802–2809, 2015. [Online]. Available: http://dx.doi.org/10.1007/s11837-015-1643-x

[35] M. Rajagopalan, K. Darling, S. Turnage, R. K. Koju, B. Hornbuckle, Y. Mishin, and K. N. Solanki, "Microstructural evolution in a nanocrystalline cu-ta alloy: A combined in-situ tem and atomistic study," *Materials & Design*, vol. 113, pp. 178–185, 1 2017. [Online]. Available: http://www.sciencedirect.com/science/article/pii/S0264127516313119

[36] Y. Mishin, M. J. Mehl, and D. A. Papaconstantopoulos, "Phase stability in the fe–ni system: Investigation by first-principles calculations and atomistic simulations," *Acta Materialia*, vol. 53, no. 15, pp. 4029–4041, 2005. [Online]. Available: http://www.sciencedirect.com/science/article/pii/S1359645405002843

[37] J. W. Cahn, Y. Mishin, and A. Suzuki, "Coupling grain boundary motion to shear deformation," *Acta Materialia*, vol. 54, no. 19, pp. 4953–4975, 11 2006. [Online]. Available: http://www.sciencedirect.com/science/article/pii/S1359645406005313

[38] Z. T. Trautt and Y. Mishin, "Capillary-driven grain boundary motion and grain rotation in a tricrystal: A molecular dynamics study," *Acta Materialia*, vol. 65, pp. 19–31, 2 2014. [Online]. Available: http://www.sciencedirect.com/science/article/pii/S1359645413009178

[39] K. A. Darling, M. Rajagopalan, M. Komarasamy, M. A. Bhatia, B. C. Hornbuckle, R. S. Mishra, and K. N. Solanki, "Extreme creep resistance in a microstructurally stable nanocrystalline alloy," *Nature*, vol. 537, no. 7620, pp. 378–381, 09 2016. [Online]. Available: http://dx.doi.org/10.1038/nature19313

[40] G. Liu, G. J. Zhang, F. Jiang, X. D. Ding, Y. J. Sun, J. Sun, and E. Ma, "Nanostructured high-strength molybdenum alloys with unprecedented tensile ductility," *Nat Mater*, vol. 12, no. 4, pp. 344–350, 04 2013. [Online]. Available: http://dx.doi.org/10.1038/nmat3544

[41] A. Hirata, T. Fujita, Y. R. Wen, J. H. Schneibel, C. T. Liu, and M. W. Chen, "Atomic structure of nanoclusters in oxide-dispersion-strengthened steels,"

Nat Mater, vol. 10, no. 12, pp. 922–926, 12 2011. [Online]. Available: http://dx.doi.org/10.1038/nmat3150

[42] T. M. Pollock and S. Tin, "Nickel-based superalloys for advanced turbine engines: Chemistry, microstructure and properties," *Journal of Propulsion and Power*, vol. 22, no. 2, pp. 361–374, 2019/10/01 2006. [Online]. Available: https://doi.org/10.2514/1.18239

[43] P. R. Subramanian and D. E. Laughlin, "The cu-ta (copper-tantalum) system," *Bulletin of Alloy Phase Diagrams*, vol. 10, no. 6, pp. 652–655, 1989. [Online]. Available: https://doi.org/10.1007/BF02877637

[44] T. B. Massalski, J. L. Murray, L. H. Bennett, and H. Baker, *Binary alloy phase diagrams*.   Metals Park, Ohio: American Society for Metals, 1986.

[45] A. G. Cullis, J. A. Borders, J. K. Hirvonen, and J. M. Poate, "Metastable alloy layers produced by implantation of ag and ta + ions into cu crystals," *Philosophical Magazine Part B*, vol. 37, no. 5, pp. 615–630, 05 1978. [Online]. Available: http://dx.doi.org/10.1080/01418637808226456

[46] G. Veltl, B. Scholz, and H. D. Kunze, "Amorphization of cu-ta alloys by mechanical alloying," *Materials Science and Engineering: A*, vol. 134, pp. 1410–1413, 1991. [Online]. Available: http://www.sciencedirect.com/science/article/pii/092150939191002A

[47] K. Sakurai, Y. Yamada, C. H. Lee, T. Fukunaga, and U. Mizutani, "Solid state amorphization in the cuta alloy system," *Materials Science and Engineering: A*, vol. 134, pp. 1414–1417, 1991. [Online]. Available: http://www.sciencedirect.com/science/article/pii/092150939191003B

[48] H. R. Gong, L. T. Kong, W. S. Lai, and B. X. Liu, "Atomistic modeling of solid-state amorphization in an immiscible cu-ta system," *Phys. Rev. B*, vol. 66, p. 104204, Sep 2002. [Online]. Available: http://link.aps.org/doi/10.1103/PhysRevB.66.104204

[49] ——, "Metastable phase formation in an immiscible cu-ta system studied by ion-beam mixing, ab initio calculation, and molecular dynamics simulation," *Acta Materialia*, vol. 51, no. 13, pp. 3885–3893, 8 2003. [Online]. Available: http://www.sciencedirect.com/science/article/pii/S1359645403002131

[50] E. Ma, "Alloys created between immiscible elements," *Progress in Materials Science*, vol. 50, no. 4, pp. 413–509, 5 2005. [Online]. Available: http://www.sciencedirect.com/science/article/pii/S0079642504000490

[51] J. M. Rigsbee, "Development of nanocrystalline copper-refractory metal alloys," *Materials Science Forum*, vol. 561-565, pp. 2373–2378, 2007. [Online]. Available: https://www.scientific.net/MSF.561-565.2373

[52] E. Hall, "The deformation and ageing of mild steel: Iii discussion of results," *Proceedings of the Physical Society. Section B*, vol. 64, no. 9, p. 747, 1951. [Online]. Available: http://dx.doi.org/10.1088/0370-1301/64/9/303

[53] E. O. HALL, "Variation of hardness of metals with grain size," *Nature*, vol. 173, no. 4411, pp. 948–949, 05 1954. [Online]. Available: http://dx.doi.org/10.1038/173948b0

[54] N. Petch, "The cleavage strength of polycrystals," *J. Iron Steel Inst.*, vol. 174, pp. 25–28, 1953.

[55] K. A. Darling, S. Mathaudhu, and L. Kecskes, "Demonstration of ultra high-strength nanocrystalline copper alloys for military applications," US Army Research Lab. Rep. Project number: WP-2139-2012., Tech. Rep., 2012. [Online]. Available: https://apps.dtic.mil/dtic/tr/fulltext/u2/a568813.pdf

[56] W. Qin, L. Fu, T. Xie, J. Zhu, W. Yang, D. Li, and L. Zhou, "Abnormal hardness behavior of cu-ta films prepared by magnetron sputtering," *Journal of Alloys and Compounds*, vol. 708, pp. 1033–1037, 2017. [Online]. Available: http://www.sciencedirect.com/science/article/pii/S0925838817308861

[57] W. Qin, L. Fu, J. Zhu, W. Yang, D. Li, and L. Zhou, "Tribological properties of self-lubricating ta-cu films," *Applied Surface Science*, vol. 435, pp. 1105–1113, 2018. [Online]. Available: http://www.sciencedirect.com/science/article/pii/S0169433217335134

[58] S. A. Turnage, M. Rajagopalan, K. A. Darling, P. Garg, C. Kale, B. G. Bazehhour, I. Adlakha, B. C. Hornbuckle, C. L. Williams, P. Peralta, and K. N. Solanki, "Anomalous mechanical behavior of nanocrystalline binary alloys under extreme conditions," *Nature Communications*, vol. 9, no. 1, p. 2699, 2018. [Online]. Available: https://doi.org/10.1038/s41467-018-05027-5

[59] M. Z. Wei, Z. H. Cao, J. Shi, G. J. Pan, L. J. Xu, and X. K. Meng, "Evolution of interfacial structures and creep behavior of cu/ta multilayers at room temperature," *Materials Science and Engineering: A*, vol. 646, pp. 163–168, 2015. [Online]. Available: http://www.sciencedirect.com/science/article/pii/S0921509315303154

[60] I. Webb, Edmund Blackburn and X. W. Zhou, "Atomically engineering cu/ta interfaces." Sandia National Laboratories, Tech. Rep., 2007. [Online]. Available: https://doi.org/10.2172/920464

[61] H. Ono, T. Nakano, and T. Ohta, "Diffusion barrier effects of transition metals for cu/m/si multilayers (m=cr, ti, nb, mo, ta, w)," *Applied Physics Letters*, vol. 64, no. 12, pp. 1511–1513, 2019/10/01 1994. [Online]. Available: https://doi.org/10.1063/1.111875

[62] H. R. Gong and B. X. Liu, "Interface stability and solid-state amorphization in an immiscible cu–ta system," *Applied Physics Letters*, vol. 83, no. 22, pp. 4515–4517, 2019/10/02 2003. [Online]. Available: https://doi.org/10.1063/1.1630353

[63] X. W. Zhou, R. A. Johnson, and H. N. G. Wadley, "Misfit-energy-increasing dislocations in vapor-deposited cofe/nife multilayers," *Physical Review B*, vol. 69, no. 14, pp. 144113–, 04 2004. [Online]. Available: https://link.aps.org/doi/10.1103/PhysRevB.69.144113

[64] A. Hashibon, A. Y. Lozovoi, Y. Mishin, C. Elsässer, and P. Gumbsch, "Interatomic potential for the cu-ta system and its application to surface wetting and dewetting," *Physical Review B*, vol. 77, no. 9, pp. 094 131–, 03 2008. [Online]. Available: https://link.aps.org/doi/10.1103/PhysRevB.77.094131

[65] M. W. Finnis and J. E. Sinclair, "A simple empirical n-body potential for transition metals," *Philosophical Magazine A*, vol. 50, no. 1, pp. 45–55, 07 1984. [Online]. Available: https://doi.org/10.1080/01418618408244210

[66] M. S. Daw and M. I. Baskes, "Embedded-atom method: Derivation and application to impurities, surfaces, and other defects in metals," *Physical Review B*, vol. 29, no. 12, pp. 6443–6453, 06 1984. [Online]. Available: https://link.aps.org/doi/10.1103/PhysRevB.29.6443

[67] V. Y. Gertsman and R. Birringer, "On the room-temperature grain growth in nanocrystalline copper," *Scripta Metallurgica et Materialia*, vol. 30, no. 5, pp. 577–581, 1994. [Online]. Available: http://www.sciencedirect.com/science/article/pii/0956716X94904324

[68] H. A. Murdoch and C. A. Schuh, "Stability of binary nanocrystalline alloys against grain growth and phase separation," *Acta Materialia*, vol. 61, no. 6, pp. 2121–2132, 4 2013. [Online]. Available: http://www.sciencedirect.com/science/article/pii/S1359645412008919

[69] L. Margulies, G. Winther, and H. F. Poulsen, "In situ measurement of grain rotation during deformation of polycrystals," *Science*, vol. 291, no. 5512, pp. 2392–2394, 2001. [Online]. Available: http://science.sciencemag.org/content/291/5512/2392

[70] P. Liu, S. C. Mao, L. H. Wang, X. D. Han, and Z. Zhang, "Direct dynamic atomic mechanisms of strain-induced grain rotation in nanocrystalline, textured, columnar-structured thin gold films," *Scripta Materialia*, vol. 64, no. 4, pp. 343–346, 2 2011. [Online]. Available: http://www.sciencedirect.com/science/article/pii/S1359646210007220

[71] J. C. M. Li, "Thermodynamics for nonequilibrium systems. the principle of macroscopic separability and the thermokinetic potential," *Journal of Applied Physics*, vol. 33, no. 2, pp. 616–624, 2019/11/12 1962. [Online]. Available: https://doi.org/10.1063/1.1702476

[72] K. E. Harris, V. V. Singh, and A. H. King, "Grain rotation in thin films of gold," *Acta Materialia*, vol. 46, no. 8, pp. 2623–2633, 5 1998. [Online]. Available: http://www.sciencedirect.com/science/article/pii/S1359645497004679

[73] B. B. Rath, M. Winning, and J. C. M. Li, "Coupling between grain growth and grain rotation," *Applied Physics Letters*, vol. 90, no. 16, 2007. [Online]. Available: http://scitation.aip.org/content/aip/journal/apl/90/16/10.1063/1.2723195

[74] J. Stolle and N. Provatas, "Characterizing solute segregation and grain boundary energy in binary alloy phase field crystal models," *Computational Materials Science*, vol. 81, pp. 493–502, 1 2014. [Online]. Available: http://www.sciencedirect.com/science/article/pii/S092702561300517X

[75] G. Gottstein and L. S. Shvindlerman, *Structure of Grain Boundaries.* CRC Press, 2009, ch. 2, pp. 111–133. [Online]. Available: http://dx.doi.org/10.1201/9781420054361-c2

[76] W. T. Read and W. Shockley, "Dislocation models of crystal grain boundaries," *Phys. Rev.*, vol. 78, pp. 275–289, May 1950. [Online]. Available: http://link.aps.org/doi/10.1103/PhysRev.78.275

[77] C. Herring, *Surface Tension as a Motivation for Sintering.* Springer, Berlin, Heidelberg, 1999. [Online]. Available: https://doi.org/10.1007/978-3-642-59938-5_2

[78] S. M. Foiles, "Evaluation of harmonic methods for calculating the free energy of defects in solids," *Phys. Rev. B*, vol. 49, pp. 14 930–14 938, Jun 1994. [Online]. Available: http://link.aps.org/doi/10.1103/PhysRevB.49.14930

[79] J. Q. Broughton and G. H. Gilmer, "Thermodynamic criteria for grain-boundary melting: A molecular-dynamics study," *Phys. Rev. Lett.*, vol. 56, pp. 2692–2695, Jun 1986. [Online]. Available: http://link.aps.org/doi/10.1103/PhysRevLett.56.2692

[80] Y. Shibuta, S. Takamoto, and T. Suzuki, "Dependence of the grain boundary energy on the alloy composition in the bcc iron–chromium alloy: A molecular dynamics study," *Computational Materials Science*, vol. 44, no. 4, pp. 1025–1029, 2 2009. [Online]. Available: http://www.sciencedirect.com/science/article/pii/S0927025608003509

[81] N. Wang, R. Spatschek, and A. Karma, "Multi-phase-field analysis of short-range forces between diffuse interfaces," *Phys. Rev. E*, vol. 81, p. 051601, May 2010. [Online]. Available: http://link.aps.org/doi/10.1103/PhysRevE.81.051601

[82] A. Suzuki and Y. Mishin, "Atomistic modeling of point defects and diffusion in copper grain boundaries," *Interface Science*, vol. 11, no. 1, pp. 131–148, 2003. [Online]. Available: http://dx.doi.org/10.1023/A:1021599310093

[83] S. M. Foiles, "Temperature dependence of grain boundary free energy and elastic constants," *Scripta Materialia*, vol. 62, no. 5, pp. 231–234, 3 2010. [Online]. Available: http://www.sciencedirect.com/science/article/pii/S1359646209007052

[84] T. Frolov and Y. Mishin, "Thermodynamics of coherent interfaces under mechanical stresses. ii. application to atomistic simulation of grain boundaries," *Phys. Rev. B*, vol. 85, p. 224107, Jun 2012. [Online]. Available: http://link.aps.org/doi/10.1103/PhysRevB.85.224107

[85] B. Schönfelder, D. Wolf, S. R. Phillpot, and M. Furtkamp, "Molecular-dynamics method for the simulation of grain-boundary migration," *Interface Science*, vol. 5, no. 4, pp. 245–262, 1997. [Online]. Available: https://doi.org/10.1023/A:1008663804495

[86] M. Upmanyu, R. W. Smith, and D. J. Srolovitz, "Atomistic simulation of curvature driven grain boundary migration," *Interface Science*, vol. 6, no. 1, pp. 41–58, 1998. [Online]. Available: http://dx.doi.org/10.1023/A:1008608418845

[87] Z. T. Trautt, M. Upmanyu, and A. Karma, "Interface mobility from interface random walk," *Science*, vol. 314, no. 5799, pp. 632–635, 2006. [Online]. Available: http://science.sciencemag.org/content/314/5799/632

[88] S. M. Foiles and J. J. Hoyt, "Computation of grain boundary stiffness and mobility from boundary fluctuations," *Acta Materialia*, vol. 54, no. 12, pp. 3351–3357, 7 2006. [Online]. Available: http://www.sciencedirect.com/science/article/pii/S1359645406002333

[89] K. G. F. Janssens, D. Olmsted, E. A. Holm, S. M. Foiles, S. J. Plimpton, and P. M. Derlet, "Computing the mobility of grain boundaries," *Nat Mater*, vol. 5, no. 2, pp. 124–127, 02 2006. [Online]. Available: http://dx.doi.org/10.1038/nmat1559

[90] A. Karma, Z. T. Trautt, and Y. Mishin, "Relationship between equilibrium fluctuations and shear-coupled motion of grain boundaries," *Phys. Rev. Lett.*, vol. 109, p. 095501, Aug 2012. [Online]. Available: http://link.aps.org/doi/10.1103/PhysRevLett.109.095501

[91] Y. Mishin, "Calculation of the γ/γ' interface free energy in the ni–al system by the capillary fluctuation method," *Modelling and Simulation in Materials Science and Engineering*, vol. 22, no. 4, p. 045001, 2014. [Online]. Available: http://dx.doi.org/10.1088/0965-0393/22/4/045001

[92] J. W. Cahn and J. E. Taylor, "A unified approach to motion of grain boundaries, relative tangential translation along grain boundaries, and grain rotation," *Acta Materialia*, vol. 52, no. 16, pp. 4887–4898, 9 2004. [Online]. Available: http://www.sciencedirect.com/science/article/pii/S1359645404003945

[93] Z. T. Trautt and Y. Mishin, "Grain boundary migration and grain rotation studied by molecular dynamics," *Acta Materialia*, vol. 60, no. 5, pp. 2407–2424, 3 2012. [Online]. Available: http://www.sciencedirect.com/science/article/pii/S1359645412000432

[94] Z. T. Trautt, A. Adland, A. Karma, and Y. Mishin, "Coupled motion of asymmetrical tilt grain boundaries: Molecular dynamics and phase field crystal simulations," *Acta Materialia*, vol. 60, no. 19, pp. 6528–6546, 11 2012. [Online]. Available: http://www.sciencedirect.com/science/article/pii/S1359645412005472

[95] J. Weissmüller, "Alloy effects in nanostructures," *Nanostructured Materials*, vol. 3, no. 1, pp. 261–272, 1993. [Online]. Available: http://www.sciencedirect.com/science/article/pii/096597739390088S

[96] P. Lejcek, *Grain Boundary Segregation in Metals.* Springer, 2010, vol. 136. [Online]. Available: https://doi.org/10.1007/978-3-642-12505-8

[97] P. Wynblatt and D. Chatain, "Anisotropy of segregation at grain boundaries and surfaces," *Metallurgical and Materials Transactions A*, vol. 37, no. 9, pp. 2595–2620, Sep 2006. [Online]. Available: https://doi.org/10.1007/BF02586096

[98] A. R. Kalidindi, T. Chookajorn, and C. A. Schuh, "Nanocrystalline materials at equilibrium: A thermodynamic review," *JOM*, vol. 67, no. 12, pp. 2834–2843, 2015. [Online]. Available: https://doi.org/10.1007/s11837-015-1636-9

[99] I. J. Beyerlein, N. A. Mara, D. Bhattacharyya, D. J. Alexander, and C. T. Necker, "Texture evolution via combined slip and deformation twinning in rolled silver–copper cast eutectic nanocomposite," *International Journal of Plasticity*, vol. 27, no. 1, pp. 121–146, 2011. [Online]. Available: http://www.sciencedirect.com/science/article/pii/S0749641910000720

[100] D. Hull and D. L. Bacon, *Introduction to Dislocations*, 3rd ed. Pergamon press, Oxford, 1984. [Online]. Available: https://doi.org/10.1016/C2009-0-64358-0

[101] L. Smith and D. Farkas, "Deformation response of grain boundary networks at high temperature," *Journal of Materials Science*, vol. 53, no. 8, pp. 5696–5705, 2018. [Online]. Available: https://doi.org/10.1007/s10853-017-1760-8

[102] J. Pelleg, *Creep in Ceramics*. Cham: Springer International Publishing, 2017. [Online]. Available: https://doi.org/10.1007/978-3-319-50826-9

[103] J. F. Panzarino and T. J. Rupert, "Tracking microstructure of crystalline materials: A post-processing algorithm for atomistic simulations," *JOM*, vol. 66, no. 3, pp. 417–428, Mar 2014. [Online]. Available: https://doi.org/10.1007/s11837-013-0831-9

[104] N. Q. Vo, S. W. Chee, D. Schwen, X. Zhang, P. Bellon, and R. S. Averback, "Microstructural stability of nanostructured cu alloys during high-temperature irradiation," *Scripta Materialia*, vol. 63, no. 9, pp. 929–932, 11 2010. [Online]. Available: http://www.sciencedirect.com/science/article/pii/S1359646210004604

[105] N. Q. Vo, J. Schäfer, R. S. Averback, K. Albe, Y. Ashkenazy, and P. Bellon, "Reaching theoretical strengths in nanocrystalline cu by grain boundary doping," *Scripta Materialia*, vol. 65, no. 8, pp. 660–663, 10 2011. [Online]. Available: http://www.sciencedirect.com/science/article/pii/S1359646211003873

[106] S. Özerinç, K. Tai, N. Q. Vo, P. Bellon, R. S. Averback, and W. P. King, "Grain boundary doping strengthens nanocrystalline copper alloys," *Scripta Materialia*, vol. 67, no. 7–8, pp. 720–723, 10 2012. [Online]. Available: http://www.sciencedirect.com/science/article/pii/S1359646212004253

[107] S. Plimpton, "Fast parallel algorithms for short-range molecular dynamics," *Journal of Computational Physics*, vol. 117, no. 1, pp. 1–19, 1995. [Online]. Available: http://www.sciencedirect.com/science/article/pii/S002199918571039X

[108] G. P. P. Pun, V. Yamakov, and Y. Mishin, "Interatomic potential for the ternary ni–al–co system and application to atomistic modeling of the b2–l1 0 martensitic transformation," *Modelling and Simulation in Materials Science and Engineering*, vol. 23, no. 6, p. 065006, 2015. [Online]. Available: http://stacks.iop.org/0965-0393/23/i=6/a=065006

[109] J. W. Cahn, Y. Mishin, and A. Suzuki, "Duality of dislocation content of grain boundaries," *Philosophical Magazine*, vol. 86, no. 25-26, pp. 3965–3980, 09 2006. [Online]. Available: http://dx.doi.org/10.1080/14786430500536909

[110] A. Stukowski, "Visualization and analysis of atomistic simulation data with ovito–the open visualization tool," *Modelling and Simulation in Materials Science and Engineering*, vol. 18, no. 1, p. 015012, 2010. [Online]. Available: http://stacks.iop.org/0965-0393/18/i=1/a=015012

[111] C. Schwink and A. Nortmann, "The present experimental knowledge of dynamic strain ageing in binary f.c.c. solid solutions," *Materials Science and Engineering: A*, vol. 234, pp. 1–7, 1997. [Online]. Available: http://www.sciencedirect.com/science/article/pii/S0921509397001391

[112] Y. Brechet and Y. Estrin, "On the influence of precipitation on the portevin-le chatelier effect," *Acta Metallurgica et Materialia*, vol. 43, no. 3, pp. 955–963, 1995. [Online]. Available: http://www.sciencedirect.com/science/article/pii/095671519400334E

[113] M. Miodownik, E. A. Holm, and G. N. Hassold, "Highly parallel computer simulations of particle pinning: zener vindicated," *Scripta Materialia*, vol. 42, no. 12, pp. 1173–1177, 2000. [Online]. Available: http://www.sciencedirect.com/science/article/pii/S1359646200003547

[114] C. L. D. Prinzio, E. Druetta, and O. B. Nasello, "More about zener drag studies with monte carlo simulations," *Modelling and Simulation in Materials Science and Engineering*, vol. 21, no. 2, p. 025007, 2013. [Online]. Available: http://stacks.iop.org/0965-0393/21/i=2/a=025007

[115] L. Vanherpe, N. Moelans, B. Blanpain, and S. Vandewalle, "Pinning effect of spheroid second-phase particles on grain growth studied by three-dimensional phase-field simulations," *Computational Materials Science*, vol. 49, no. 2, pp. 340–350, 8 2010. [Online]. Available: http://www.sciencedirect.com/science/article/pii/S0927025610002922

[116] F. Uyar, S. R. Wilson, J. Gruber, S. Lee, S. Sintay, A. D. Rollett, and D. J. Srolovitz, "Testing a curvature driven moving finite element grain growth model with the generalized three dimensional von neumann relation," *International Journal of Materials Research*, vol. 100, no. 4, pp. 543–549, 2016/11/20 2009. [Online]. Available: http://dx.doi.org/10.3139/146.110075

[117] S. Takeuchi, "The mechanism of the inverse hall-petch relation of nanocrystals," *Scripta Materialia*, vol. 44, no. 8, pp. 1483 – 1487, 2001. [Online]. Available: http://www.sciencedirect.com/science/article/pii/S1359646201007138

[118] L. Yue, H. Zhang, and D. Y. Li, "A closer look at the local responses of twin and grain boundaries in cu to stress at the nanoscale with possible transition from the p-h to the inverse p-h relation," *Acta Materialia*, vol. 58, no. 7, pp. 2677–2684, 2010. [Online]. Available: http://dx.doi.org/10.1016/j.actamat.2009.12.054

[119] Z. X. Wu, Y. W. Zhang, M. H. Jhon, and D. J. Srolovitz, "Anatomy of nanomaterial deformation: Grain boundary sliding, plasticity and cavitation in nanocrystalline ni," *Acta Materialia*, vol. 61, no. 15, pp. 5807–5820, 2013. [Online]. Available: http://www.sciencedirect.com/science/article/pii/S1359645413004588

[120] J. Li and A. K. Soh, "Synergy of grain boundary sliding and shear-coupled migration process in nanocrystalline materials," *Acta Materialia*, vol. 61, no. 14, pp. 5449–5457, 2013. [Online]. Available: http://www.sciencedirect.com/science/article/pii/S1359645413004114

[121] B. Chen, K. Lutker, J. Lei, J. Yan, S. Yang, and H.-k. Mao, "Detecting grain rotation at the nanoscale," *Proceedings of the National Academy of Sciences*, vol. 111, no. 9, pp. 3350–3353, 2014. [Online]. Available: https://www.pnas.org/content/111/9/3350

[122] X. Han, L. Wang, Y. Yue, and Z. Zhang, "In situ atomic scale mechanical microscopy discovering the atomistic mechanisms of plasticity in nano-single crystals and grain rotation in polycrystalline metals," *Ultramicroscopy*, vol. 151, pp. 94–100, 2015. [Online]. Available: http://www.sciencedirect.com/science/article/pii/S0304399114002551

[123] X. Zhou, N. Tamura, Z. Mi, J. Lei, J. Yan, L. Zhang, W. Deng, F. Ke, B. Yue, and B. Chen, "Reversal in the size dependence of grain rotation," *Phys. Rev. Lett.*, vol. 118, p. 096101, Mar 2017. [Online]. Available: https://link.aps.org/doi/10.1103/PhysRevLett.118.096101

[124] M. Saber, H. Kotan, C. C. Koch, and R. O. Scattergood, "Thermodynamic stabilization of nanocrystalline binary alloys," *Journal of Applied Physics*, vol. 113, no. 6, p. 063515, 2013. [Online]. Available: https://doi.org/10.1063/1.4791704

[125] ——, "A predictive model for thermodynamic stability of grain size in nanocrystalline ternary alloys," *Journal of Applied Physics*, vol. 114, no. 10, p. 103510, 2013. [Online]. Available: https://doi.org/10.1063/1.4821040

[126] A. R. Kalidindi and C. A. Schuh, "Stability criteria for nanocrystalline alloys," *Acta Materialia*, vol. 132, pp. 128–137, 2017. [Online]. Available: http://www.sciencedirect.com/science/article/pii/S1359645417302197

[127] F. Abdeljawad, P. Lu, N. Argibay, B. G. Clark, B. L. Boyce, and S. M. Foiles, "Grain boundary segregation in immiscible nanocrystalline alloys," *Acta Materialia*, vol. 126, pp. 528–539, 2017. [Online]. Available: http://www.sciencedirect.com/science/article/pii/S1359645416309715

[128] R. Kirchheim, "Reducing grain boundary, dislocation line and vacancy formation energies by solute segregation. i. theoretical background," *Acta Materialia*, vol. 55, no. 15, pp. 5129–5138, 2007. [Online]. Available: http://www.sciencedirect.com/science/article/pii/S1359645407003655

[129] ——, "Reducing grain boundary, dislocation line and vacancy formation energies by solute segregation: Ii. experimental evidence and consequences," *Acta Materialia*, vol. 55, no. 15, pp. 5139 – 5148, 2007. [Online]. Available: http://www.sciencedirect.com/science/article/pii/S1359645407003667

[130] N. Ma, S. Dregia, and Y. Wang, "Solute segregation transition and drag force on grain boundaries," *Acta Materialia*, vol. 51, no. 13, pp. 3687 – 3700, 2003. [Online]. Available: http://www.sciencedirect.com/science/article/pii/S1359645403001848

[131] R. K. Koju, K. A. Darling, L. J. Kecskes, and Y. Mishin, "Zener pinning of grain boundaries and structural stability of immiscible alloys," *JOM*, vol. 68, no. 6, pp. 1596–1604, 2016. [Online]. Available: http://dx.doi.org/10.1007/s11837-016-1899-9

[132] V. Yamakov. The paragrandmc code can be obtained from the nasa software catalog. [Online]. Available: https://software.nasa.gov/software/LAR-18773-1

[133] D. Frenkel and B. Smit, *Understanding Molecular Simulation: from Algorithms to Applications*, 2nd ed. San Diego: Academic, 2002. [Online]. Available: https://doi.org/10.1016/B978-0-12-267351-1.X5000-7

[134] A. Suzuki and Y. M. Mishin, "Atomic mechanisms of grain boundary motion," *Materials Science Forum*, vol. 502, pp. 157–162, 2005. [Online]. Available: https://www.scientific.net/MSF.502.157

[135] S. Srinivasan and J. Cahn, *Challenging Some Free-Energy Reduction Criteria for Grain Growth*. John Wiley & Sons, Ltd, 2013, pp. 1–14. [Online]. Available: https://onlinelibrary.wiley.com/doi/abs/10.1002/9781118788103.ch1

[136] M. F. Ashby, J. Harper, and J. Lewis, "The interaction of crystal boundaries with second-phase particles," *The American Institute of Mining, Metallurgical, and Petroleum Engineers*, 1969.

[137] G. T. and A. N. Percy, "On the theory of the effect of precipitate particles on grain growth in metals," *Proceedings of the Royal Society of London. Series A. Mathematical and Physical Sciences*, vol. 294, no. 1438, pp. 298–309, 2019/04/30 1966. [Online]. Available: https://doi.org/10.1098/rspa.1966.0208

[138] N. Wang, Y. Ji, Y. Wang, Y. Wen, and L.-Q. Chen, "Two modes of grain boundary pinning by coherent precipitates," *Acta Materialia*, vol. 135, pp. 226 – 232, 2017. [Online]. Available: http://www.sciencedirect.com/science/article/pii/S1359645417305062

[139] A. P. Sutton, "Interfaces in crystalline materials," *Monographs on the Physice and Chemistry of Materials*, pp. 414–423, 1995. [Online]. Available: https://ci.nii.ac.jp/naid/10006547402/en/

[140] T. Frolov and Y. Mishin, "Stable nanocolloidal structures in metallic systems," *Phys. Rev. Lett.*, vol. 104, p. 055701, Feb 2010. [Online]. Available: https://link.aps.org/doi/10.1103/PhysRevLett.104.055701

[141] R. K. Koju, K. A. Darling, K. N. Solanki, and Y. Mishin, "Atomistic modeling of capillary-driven grain boundary motion in cu-ta alloys," *Acta Materialia*, vol. 148, pp. 311–319, 2018. [Online]. Available: http://www.sciencedirect.com/science/article/pii/S1359645418300582

[142] K. Darling, E. Huskins, B. Schuster, Q. Wei, and L. Kecskes, "Mechanical properties of a high strength cu–ta composite at elevated temperature," *Materials Science and Engineering: A*, vol. 638, no. Supplement C, pp. 322 – 328, 2015. [Online]. Available: http://www.sciencedirect.com/science/article/pii/S0921509315004761

[143] M. A. Bhatia, M. Rajagopalan, K. A. Darling, M. A. Tschopp, and K. N. Solanki, "The role of ta on twinnability in nanocrystalline cu–ta alloys," *Materials Research Letters*, vol. 5, no. 1, pp. 48–54, 01 2017. [Online]. Available: http://dx.doi.org/10.1080/21663831.2016.1201160

[144] A. F. Voter, F. Montalenti, and T. C. Germann, "Extending the time scale in atomistic simulation of materials," *Annual Review of Materials Research*, vol. 32, no. 1, pp. 321–346, 2016/11/29 2002. [Online]. Available: http://dx.doi.org/10.1146/annurev.matsci.32.112601.141541

[145] M. R. Sørensen and A. F. Voter, "Temperature-accelerated dynamics for simulation of infrequent events," *The Journal of Chemical Physics*, vol. 112, no. 21, pp. 9599–9606, 2019/11/12 2000. [Online]. Available: https://doi.org/10.1063/1.481576

[146] D. Perez, E. D. Cubuk, A. Waterland, E. Kaxiras, and A. F. Voter, "Long-time dynamics through parallel trajectory splicing," *Journal of Chemical Theory and Computation*, vol. 12, no. 1, pp. 18–28, 01 2016. [Online]. Available: http://dx.doi.org/10.1021/acs.jctc.5b00916

[147] D. Perez, B. P. Uberuaga, and A. F. Voter, "The parallel replica dynamics method –coming of age," *Computational Materials Science*, vol. 100, Part B, pp. 90–103, 4 2015. [Online]. Available: http://www.sciencedirect.com/science/article/pii/S0927025614008489

[148] G. Dieter and D. Bacon, *Mechanical Metallurgy*. McGraw-Hill New York, 1986.

[149] J. Chen, L. Lu, and K. Lu, "Hardness and strain rate sensitivity of nanocrystalline cu," *Scripta Materialia*, vol. 54, no. 11, pp. 1913–1918, 2006. [Online]. Available: http://www.sciencedirect.com/science/article/pii/S1359646206001242

[150] Q. Wei, S. Cheng, K. T. Ramesh, and E. Ma, "Effect of nanocrystalline and ultrafine grain sizes on the strain rate sensitivity and activation volume: fcc versus bcc metals," *Materials Science and Engineering: A*, vol. 381, no. 1, pp. 71–79, 2004. [Online]. Available: http://www.sciencedirect.com/science/article/pii/S0921509304003946

[151] O. D. Sherby and J. Wadsworth, "Superplasticity—recent advances and future directions," *Progress in Materials Science*, vol. 33, no. 3, pp. 169–221, 1989. [Online]. Available: http://www.sciencedirect.com/science/article/pii/0079642589900042

[152] M. Rajagopalan, K. A. Darling, C. Kale, S. A. Turnage, R. K. Koju, B. C. Hornbuckle, Y. Mishin, and K. N. Solanki, "Nanotechnology enabled design of a structural material with extreme strength as well as thermal and electrical properties," *Materials Today*, vol. 31, pp. 10–20, 2019. [Online]. Available: http://www.sciencedirect.com/science/article/pii/S1369702119308028

[153] S. Jiao and Y. Kulkarni, "Molecular dynamics study of creep mechanisms in nanotwinned metals," *Computational Materials Science*, vol. 110, pp. 254–260, 2015. [Online]. Available: http://www.sciencedirect.com/science/article/pii/S0927025615005145

[154] F. Louchet and P. Duval, "Andrade creep revisited," *International Journal of Materials Research*, vol. 100, no. 10, pp. 1433–1439, 2019/08/15 2009. [Online]. Available: https://doi.org/10.3139/146.110189

Curriculum Vitae

Raj Kiran Koju was born in Byasi, Bhaktapur, Nepal. He went to Vidhay Vikash Secondary School, Bhaktapur and Kathmandu Institute of Science and Technology, Kathmandu. He earned his B.Sc. degree in physics from Tri-Chandra Campus, Tribhuvan University, Nepal in 2007. He received his M.Sc. degree in physics from the Central Department of Physics, University Campus, Tribhuvan University, Nepal in 2011. The title of his master's thesis was "Study of visual flux emitted from the outer layer of red supergiant Betelgeuse observed from national observatory, Nagarkot, Nepal." He enrolled Ph.D. program in physics with a presidential scholarship at George Mason University, Fairfax, Virginia in 2012. He worked as a graduate research assistant under the supervision of Dr. Yuri Mishin from 2014 and published the following papers.

1. M. Rajagopalan, K. Darling, S. Turnage, R.K. Koju, C. Kale, B. Hornbuckle, Y. Mishin, K.N. Solanki "Nanotechnology enabled design of a structural material with extreme strength as well as thermal and electrical properties", Materials Today, **31**, 10-20, (2019).

2. R.K. Koju, K.A. Darling, K.N. Solanki and Y. Mishin: "Atomistic modeling of capillary-driven grain boundary motion in Cu-Ta alloys", Acta Materialia **148**, 311-319 (2018).

3. M. Rajagopalan, K. Darling, S. Turnage, R.K. Koju, B. Hornbuckle, Y. Mishin, K.N. Solanki: "Microstructural evolution in a nanocrystalline Cu-Ta alloy: A combined in-situ TEM and atomistic study", Materials and Design **113**, 178-185 (2017).

4. R.K. Koju, K. A. Darling, L. J. Kecskes and Y. Mishin: "Zener pinning of grain boundaries and structural stability of immiscible alloys", JOM **68**, 1596-1604 (2016).

Emails: rkoju@masonlive.gmu.edu
        rajkiran_koju@hotmail.com
ORCID ID: 0000-0001-9799-2103
Google Scholar: R K Koju